

Demonstrating Quantum Speed-Up with a Two-Transmon Quantum Processor.

Andreas Dewes

May 24, 2012

Contents

1	Introduction & Summary	13
1.1	Quantum Computing & Circuit Quantum Electrodynamics	13
1.2	Realizing a Two-Qubit Quantum Processor	16
1.3	Demonstrating Simultaneous Single-Shot Readout	17
1.4	Generating and Characterizing Entanglement	18
1.5	Realizing a Universal Two-Qubit Quantum Gate	21
1.6	Running a Quantum Search Algorithm	22
1.7	Demonstrating Quantum Speed-Up	23
2	Theoretical Foundations	25
2.1	Classical & Quantum Information Processing	25
2.2	Principles of Quantum Computing	26
2.2.1	Quantum Bits	26
2.2.2	Quantum Gates	27
2.3	Superconducting Quantum Circuits	28
2.3.1	The Josephson junction	28
2.3.2	Transmission Lines	29
2.3.3	Transmission Line Resonators	29
2.3.4	Quantization of Electrical Circuits	32
2.3.5	The Cooper Pair Box	34
2.4	The Transmon Qubit	35
2.5	Circuit Quantum Electrodynamics	36
2.5.1	Dispersive Limit & Qubit Readout	36
2.6	The Josephson Bifurcation Amplifier	37
3	Realizing a Two-Qubit Processor	39
3.1	Introduction & Motivation	39
3.2	Qubit Design	40
3.3	Readout Design	40
3.4	Processor Fabrication	40

4 Measurement Setup	41
4.1 Sample Holder & PCB	41
4.2 Cryogenic Wiring	42
4.3 Signal Generation & Acquisition	43
4.3.1 Microwave Sideband Mixing	43
4.3.2 Fast Magnetic Flux Pulses	44
4.3.3 Pulse Synchronization	45
5 Measurement Techniques	47
5.1 Qubit Readout	47
5.2 Qubit Manipulation	47
5.3 Decoherence Time Measurement	47
6 Characterizing the Two-Qubit Processor	49
6.1 Qubit & Readout Characterization	49
6.1.1 Qubit Parameters	50
Readout Parameters	50
Qubit Readout, Driving, Relaxation and Dephasing Time	50
6.2 Single-Qubit Operations	52
6.2.1 Estimation of drive errors	53
6.3 Two Qubit Operations	53
6.3.1 Creation of Entanglement	53
6.3.2 Violation of the Bell Inequality	53
6.3.3 Quantum State Tomography of Two-Qubit States	55
Maximum Likelihood Estimation of Quantum States	55
6.4 Realizing a Two-Qubit Gate	57
6.4.1 Principle	57
6.4.2 Experimental Implementation	57
6.4.3 Quantum Process Tomography of the Gate	57
Introduction & Principle	57
Implementation	57
The Kraus Representation of the Quantum Process	61
6.4.4 Gate Fidelity	62
6.4.5 Gate Error Analysis	62
7 Running the Grover Search Algorithm	65
7.1 Introduction & Motivation	65
7.1.1 Deriving the Grover Algorithm from Schrödinger's Equation	67
Efficiency of Quantum "Crawling"	70
7.1.2 Ancilla-based Implementation of the Algorithm	72

<i>CONTENTS</i>	5
-----------------	---

7.2 Comparision to a Classical Algorithm	73
7.3 Experimental Implementation	74
7.3.1 Pulse Sequence	75
7.4 Results	75
7.4.1 State Tomography of the Algorithm	76
7.4.2 Single Run Results	76
7.5 Algorithm Fidelity	77
7.6 Error Analysis	78
7.6.1 Gate Errors & Decoherence	79
Modeling Decoherence	79
Fidelity of the Oracle and diffusion operators	83
7.6.2 Readout Errors	83
7.7 Conclusions	85
8 Conclusions & Perspective	87
8.1 Future Directions in Superconducting QC	87
8.1.1 3D Circuit Quantum Electrodynamics	87
8.1.2 Hybrid Quantum Systems	87
8.1.3 Quantum Error Correction & Feedback	87
A Modeling of Multi-Qubit Systems	89
A.1 Analytical Approach	89
A.1.1 Multi-Qubit Hamiltonian	89
A.1.2 Energies and Eigenstates	89
A.2 Master Equation Approach	89
A.2.1 Direct Integration	89
A.2.2 Monte Carlo Simulation	89
A.2.3 Speeding Up Simulations	89
B Data Acquisition & Management	91
B.1 Data Acquisition Infrastructure	91
B.2 Data Management Requirements	91
B.3 PyView	91
B.3.1 Overview	91
B.3.2 Instrument Management	91
B.3.3 Data Acquisition	91
B.3.4 Data Management	91
B.3.5 Data Analysis	91

C Design & Fabrication	93
C.1 Mask Design	93
C.2 Optical Lithography	93
C.3 Electron Beam Lithography	93
D Bibliography	93

List of Figures

1.1 Blueprint of a “canonical” two-qubit quantum processor	13
1.2 Circuit schematic of the realized two-qubit processor	16
1.3 Switching probabilities of the two qubit readouts as a function of the read-out excitation power	17
1.4 Generating entangled two-qubit states by swapping interaction	19
1.5 Measurement of the CHSH operator of an entangled two-qubit state	20
1.6 Measured χ -matrix of the $\sqrt{i\text{SWAP}}$ gate	21
1.7 Schematic of the implementation of the Grover search algorithm	22
1.8 Measured density matrices when running the Grover algorithm	23
1.9 Single-run results of the Grover search algorithm	23
2.1 The Bloch sphere representation of a qubit state $ \psi\rangle = \cos \frac{\theta}{2} 0\rangle + e^{i\phi} \sin \frac{\theta}{2} 1\rangle$. The state $ \psi\rangle$ is fully characterized by specifying its “altitude” and “azimuth” angles θ and ϕ . Pure quantum states will always lie on the surface of the Bloch sphere, whereas mixed quantum states can also lie anywhere inside the sphere.	26
2.2 The three main circuit elements that are used to construct superconducting quantum circuits. Shown are a) a Josephson junction, b) an inductor and c) a capacitor.	27
2.3 a) The circuit diagram of a grounded transmission line. b) The circuit diagram of a grounded coaxial transmission line.	29
2.4 This is the side caption which is maybe already to small to support such long text..	31
2.5 An exemplary superconducting circuit made of a Josephson junction, a capacitor and a voltage source. The circuit topology can be described by one node (plus ground) and one branch.	32

2.6	The circuit schematic of a Split Cooper Pair Box. The device consists of two Josephson junctions arranged in a loop, where the capacitance of the junctions is modeled as the extra capacitor indicated on the left. By putting the two junctions in series with a gate capacitance one creates an island one which charges can accumulate. The gate voltage can be controlled by an external voltage source.	34
2.7	Energies of the first four energy level of the Cooper pair box for different ratios E_J/E_C , plotted as a function of the gate charge n_g . As can be seen, for $E_J \ll E_C$, the charge-dispersion curve becomes almost completely flat.	35
3.1	Circuit schematic of the two-qubit processor	39
4.1	The measurement setup used for the two-qubit experiments	42
6.1	Spectroscopy of the Two-Qubit Processor	49
6.2	A qubit parameter survey showing T_1 , readout contrast and Rabi frequency of the two qubits over a large range of qubit frequencies	51
6.3	Demonstration of single-qubit IQ control	52
6.4	53
6.5	Experimentally created $ \psi_+\rangle$ ($F = 0.91$) and $ \psi_-\rangle$ ($F = 0.93$) states	54
6.6	54
6.7	test	57
6.8	The input-output density matrix of the quantum process tomography of the $\sqrt{i\text{SWAP}}$ gate. Shown are the measured density matrices of 16 different input states and the corresponding output matrices with their state fidelities. The ideal matrices are overlaid in red.	58
6.9	The input-output density matrix of the quantum process tomography of the $\sqrt{i\text{SWAP}}$ gate. Shown are the measured density matrices of 16 different input states and the corresponding output matrices with their state fidelities. The ideal matrices are overlaid in red.	59
6.10	64
7.1	A wavefunction $\psi(x)$ and potential $V(x)$ defined on a grid of points x_1, \dots, x_N .	68
7.3	Full version of an ancilla-based implementation of the two-qubit Grover search algorithm	73

7.4 Classical reversible implementation of a search algorithm on a two-bit input register. The Oracle function can be implemented by two single-bit NOT operations and a Toffoli gate. R designates the generation of a random binary value at the beginning of the algorithm. If the Oracle does not yield the correct answer, the test state is incremented. The average success probability of the algorithm is 50 %	73
7.5 Schematic of our implementation of the Grover search algorithm	74
7.6 Pulse sequence used for implementing Grovers search algorithm	75
7.7 Quantum state tomographies at different steps during the Grover search algorithm and single-run outcome probabilities	77
7.8 Single-run success probabilities of the Grover search algorithm	78
7.9 Error model used for analyzing gate and decoherence errors for the Grover search algorithm	80
7.10 Comparision of the general error model to our experimental data	82
7.11 Measured single- and two-qubit readout matrices and crosstalk matrix for the Grover search algorithm experiment	84

List of Tables

7.1	Conditional probabilities $p_{ab/ uv\rangle}$ and statistical fidelities f_{ab} for all possible outcomes ab , measured for our version of Grover's algorithm.	78
7.2	Fitted gate error parameters of the Grover algorithm	81
7.3	Measured fidelities of the quantum Oracle and diffusion operators used in the Grover search algorithm	83

Chapter 1

Introduction & Summary

1.1 Quantum Computing & Circuit Quantum Electrodynamics

This thesis presents experiments performed with a superconducting two-qubit quantum processor. The main goal of this work was to demonstrate a possible quantum computing architecture based on superconducting qubits that follows the canonical blueprint of a quantum processor as shown in fig. 1.1, in accordance with the five criteria formulated by DiVincenzo (2000). By this definition, a universal quantum computer is a register of well-defined quantum bits (1) with long coherence times (2) on which one can perform universal single- and two-qubit quantum gates(3), read out the state of each qubit individually and with high fidelity (4) and reset the qubit register to a well-defined state (5).

Implementing this allegedly simple list of requirements in a system of superconducting qubits has been a major research challenge during the last decade. Incoherent quantum tunneling in a superconducting device was observed for the first time by Devoret et al. (1985); Martinis et al. (1985) and Clarke et al. (1988), which showed that it

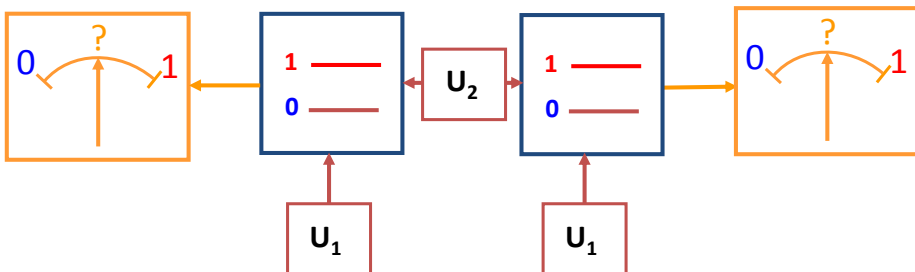


Figure 1.1: The blueprint of a “canonical” two-qubit quantum processor. Shown are two qubits that can be individually manipulated (U_1) and are connected by a universal two-qubit gate U_2 . Each of the qubits can be read out individually.

is possible to cool down a Josephson junction sufficiently to see quantum-mechanical tunneling between different quantum levels of the system. However, the observation of incoherent quantum tunneling did not prove that the quantum state of these devices could be manipulated coherently. The first demonstration of such coherent quantum behaviour in a superconducting system was achieved more than ten years later by Nakamura et al. (1999), who measured for the first time coherent energy oscillations between two quantum levels of a Cooper pair box. This experiment created a large interest in superconducting quantum circuits and led to development of a research field on superconducting quantum computing. In the years after Nakamuras experiment, several types of superconducting qubits were proposed using Josephson junctions in different configurations to realize systems where e.g. the Josephson phase (Martinis et al., 2002) or the magnetic flux inside a superconducting ring (Mooij et al., 1999; Chiorescu et al., 2003) are the dominant quantum variables. In this context, an important result on the way to robust superconducting qubits was the development of the so-called *Quantronium* qubit by Vion et al. (2002). The Quantronium is a Cooper pair box with comparable Josephson and charging energies operated at a well-defined “sweet spot” at which the sensitivity of the device to charge and flux noise is greatly reduced. The high coherence times achieved with the Quantronium –values larger than $2 \mu s$ have been reported– allowed for the first time the implementation of NMR-like quantum operations using a superconducting qubit (Collin et al., 2004). Shortly after that, in 2004, the development of another new type of qubit, the so called *Transmon*, by Wallraff et al. (2004) marked again a drastic improvement in coherence times, qubit robustness and usability. The Transmon qubit is a Cooper pair box shunted with a large capacitor that drastically decreases the charging energy of the system and thus renders the device almost insensitive to charge noise, however still leaving sufficient anharmonicity to operate the device as a qubit. With the Transmon, coherence times comparable or higher than those reported for the Quantronium have been achieved *without* operating the qubit at a special working point, thereby greatly reducing experimental complexity. Furthermore, by embedding the Transmon qubit in a superconducting coplanar waveguide (CPW) resonator it is possible to protect it from external sources of electrical noise and use the dispersive interaction between the qubit and the resonator for reading out the qubit state (Blais et al., 2004). This approach of embedding a superconducting qubit in a waveguide resonator has been termed –in analogy with conventional quantum electrodynamics– *circuit quantum electrodyamics* (CQED) and gained wide popularity in the superconducting qubit community **!1!**. So far, using this CQED approach, superconducting quantum processors with up to three qubits have been realized and two- and three-qubit quantum gates (Fedorov et al., 2011), multi-qubit entanglement (DiCarlo et al., 2010) and simple quantum algorithms (DiCarlo et al., 2009) as well as quantum error correction (Reed et al., 2011) have been demonstrated. Futhermore, experiments demonstrating

To Do 1: add some citations of relevant experiments

fundamental quantum effects that before were accessible only in quantum optics have been performed, demonstrating e.g. QND measurements of photons in a cavity (Johnson et al., 2010), the resolution of photon-number states (Schuster et al., 2007) and the measurement of the Autler-Townes and Mollow transitions with a superconducting qubit (Baur et al., 2009).

Recently, a new type of CQED architecture has been developed by Paik et al. (2011) that combines Transmon qubits with 3D cavities instead of CPW resonators, resulting again in an impressive increase of qubit coherence times of up to two orders of magnitude, with reported qubit relaxation times as high as $80 \mu\text{s}$ **!2!** and decoherence times at a comparable time scale. These drastically improved coherence times have already made possible the realization of elemental quantum feedback and error correction schemes with these systems **!3!** and make them promising candidates for the realization of a superconducting quantum computer. **!4!**

To Do 2: verify this!

To Do 3: cite Irfan's paper here

To Do 4: expand this section as soon as new relevant material appears, include recent IBM, Yale

In parallel to this, the development of quantum-limited amplifiers based on nonlinear superconducting resonators by Siddiqi et al. (2004) and Vijay et al. (2009) provided a very useful tool for measuring and amplifying weak quantum signals, which was already used in several context within the field of superconducting qubits: By operating such a nonlinear amplifier in a hysteretic regime and coupling it, in analogy to the CQED approach, dispersively to a superconducting qubit, Siddiqi et al. (2006) and Mallet et al. (2009) were able to demonstrate a high-fidelity readout scheme for Transmon qubits, reaching up to 97 % readout fidelity. Vijay et al. (2011) used quantum-limited amplifiers to read out a Transmon qubit coupled to a linear microwave cavity and were able to observe quantum jumps of its state. **!5!** used a similar setup with a 3D Transmon to implement a quantum feedback scheme to phase-stabilize a Rabi oscillation of a superconducting qubit.

To Do 5: Add Quantum Feedback Paper Here

With the research presented in this thesis we aim **!1!** to complement the CQED architecture as outlined in the last sections by combining a multi-qubit architecture based on Transmon qubits with a readout scheme based on a nonlinear bifurcation amplifier, thus providing the so-far missing per-qubit single-shot readout that is needed to realize a canonical superconducting quantum processor with these devices.

Comment 1: can I really say "we" here or should it be "I"?

The first part of the thesis discusses the realization of a superconducting two-qubit processor based on Transmon qubits fitted with individual single-shot readouts. With this processor, we implement elementary one- and two-qubit quantum operations and use it to run a simple quantum algorithm that demonstrates probabilistic quantum speed-up. Finally, we discuss the realization of a four-qubit quantum processor using a more scalable approach that could possibly be extended to an even larger number of qubits.

1.2 Realizing a Two-Qubit Quantum Processor

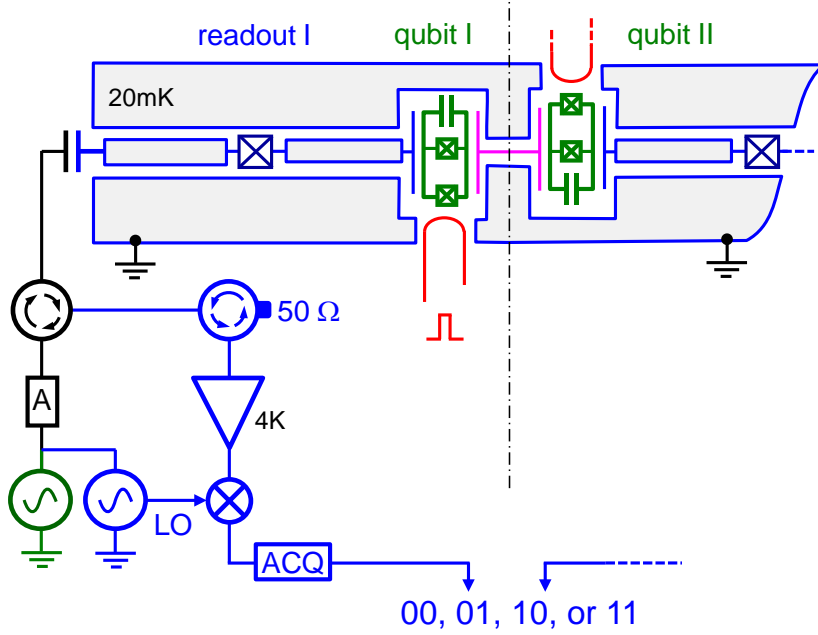


Figure 1.2: Circuit schematic of the two-qubit processor realized in this work, showing the two qubits in green, the qubit readouts in blue and the fast flux lines in red. Each qubit is embedded in its own nonlinear readout resonator and can be driven and read out through an individual microwave line.

The quantum processor implemented in this work is shown in fig. 1.2. It consists of two superconducting quantum bits of the Transmon type, each equipped with its own drive and readout circuit. The qubit readout is realized using a nonlinear coplanar-waveguide resonator that serves as a so-called *cavity bifurcation amplifier* (CBA)(Siddiqi et al., 2006; Mallet et al., 2009; Vijay et al., 2009) and allows a single-shot readout of the qubit state. Each qubit can be manipulated by driving it with microwave pulses through its readout resonator, allowing for robust and fast single-qubit operations. The qubit frequencies can be tuned individually using fast flux lines, allowing us to change the frequency of each qubit over a range of several GHz. The coupling between the two qubits is realized through a fixed capacitance that connects the two top-electrodes of the Transmons and implements a fixed σ_{xx} -type qubit-qubit coupling. This coupling allows us to generate entangled two-qubit states and to implement a two-qubit gate. We use this simple processor to generate entangled two-qubit states, test the Bell inequality, implement an universal two-qubit gate and perform a simple quantum algorithm that demonstrates probabilistic quantum speed-up, as will be discussed in the following sections.

1.3 Demonstrating Simultaneous Single-Shot Readout

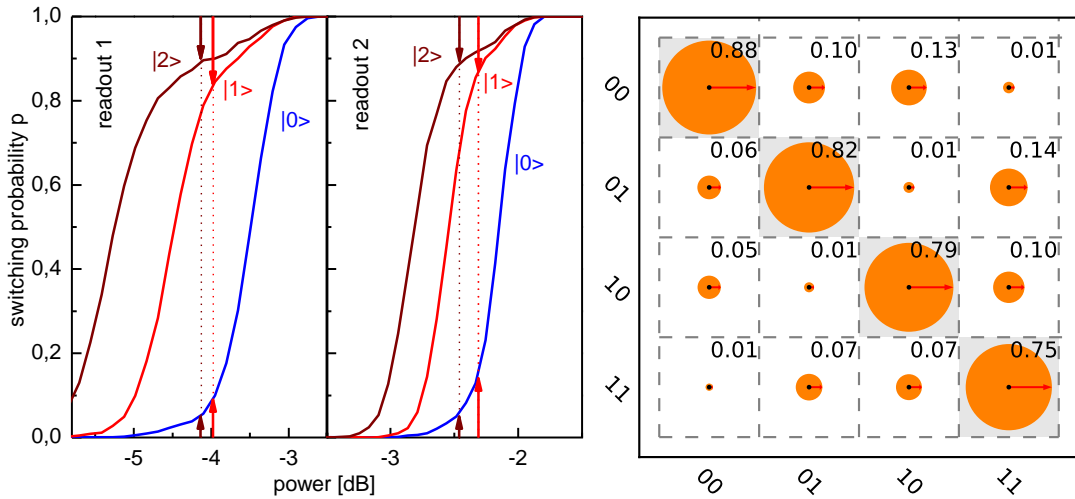


Figure 1.3: a) Switching probabilities of the two qubit readouts as a function of the readout drive power at a fixed driving frequency. The measurement is performed after preparing the qubits in the states $|0\rangle$, $|1\rangle$ and $|2\rangle$. The readout contrast is given as the difference in probability between the curves corresponding to the states $|0\rangle$ and $|1\rangle$ or $|2\rangle$, respectively. The highest contrasts of 88 and 89 % are achieved when the qubit is in state $|2\rangle$. b) Readout matrix of the two-qubit system. The matrix contains the probabilities of obtaining a given measurement result after having prepared the system in a given state. **Figure Comment 2:** Replace this figure since it is not very intuitive. It would be better to show something which allows the reader to directly quantify the visibility and readout crosstalk present in the system.

For the read out the qubit state we use a so called *cavity bifurcation amplifier* (CBA). This approach consists in capacitively coupling the qubit to a coplanar waveguide resonator that is rendered nonlinear by placing a Josephson junction in its center conductor. The capacitive coupling between the qubit and the resonator creates a dispersive interaction between them that induces a change of the resonance frequency of the resonator dependent on the state of the qubit, and vice versa. Furthermore, the resonator can exhibit bistability at certain drive parameters due to its nonlinearity. Therefore, by driving it at a carefully chosen frequency and drive amplitude we can use the dispersive qubit-resonator interaction to map the state of the qubit to one of the bistable states of the resonator. We can then stabilize this resonator state by changing its operating point, effectively freezing it from the further evolution of the qubit state. This allows us to measure the state of the resonator with high precision without being limited by qubit relaxation, thereby providing a high-fidelity, single-shot qubit readout. Contrary to other CQED approaches, in our setup each individual qubit is fitted with such a CBA readout, allowing hence a simultaneous readout of the full two-qubit register, following the canonical blueprint of a quantum computer as formulated by DiVincenzo. For single-qubit CBA

readouts, readout fidelities up to 93 % have been reported (Mallet et al., 2009). However, due to the higher complexity and design constraints of our system, only 83-89 % fidelity have been achieved for the processor presented here. The full characterization of the readout of our processor is shown in fig. 1.3. Fig. 1.3a shows the switching probabilities of each individual qubit readout as a function of the drive amplitude, measured at a fixed drive frequency. Individual curves correspond to the qubit being prepared in different states $|0\rangle$, $|1\rangle$ or $|2\rangle$, the difference between either two curves giving the readout contrast between those qubit states. Preparing the qubit in state $|2\rangle$ before readout can increase the readout fidelity by more than 10 % and is therefore often used in the experiments presented in this thesis. Fig. 1.3b shows the full readout matrix of the two-qubit register that relates measured readout switching probabilities with real qubit state occupation probabilities and allows us to correct readout errors when performing quantum state tomography. In the main text of this thesis we discuss all relevant readout fidelities and errors in details and analyze different error sources limiting the readout performance in our experiments.

1.4 Generating and Characterizing Entanglement

The capacitive coupling between the two qubits provides a σ_{xx} -type interaction that can be used to generate entangled two-qubit states. Conveniently, this coupling is only effective when the qubit frequencies are near-resonant and can therefore be effectively switched on and off by tuning the qubit frequencies in and out of resonance. For the processor realized in this work, the effective coupling constant g of the two qubits has been measured as $2g = 8.2$ MHz. When the two qubits are in resonance, the effective Hamiltonian of the two-qubit system can be written as

$$U(t) = \begin{pmatrix} 1 & 0 & 0 & 0 \\ 0 & \cos 2\pi t g & i \sin 2\pi t g & 0 \\ 0 & i \sin 2\pi t g & \cos 2\pi t g & 0 \\ 0 & 0 & 0 & 1 \end{pmatrix} \quad (1.1)$$

, where $U(t)$ is written in the basis $\{|00\rangle, |01\rangle, |10\rangle, |11\rangle\}$. By using fast flux pulses to non-adiabatically tune the qubits in and out of resonance we can switch on this interaction for a well-defined time. We first characterize the effect of the coupling on the qubit register by preparing the state $|10\rangle$, tuning the qubits in resonance for a given time and measuring the qubit state afterwards. The resulting curve is shown in fig. 1.4 and clearly shows energy oscillations between the two qubits. Analyzing this curve allows us to extract the effective coupling strength between the qubits. Leaving the interaction between the qubits on for a well-defined time allows us to generate entangled Bell states that we

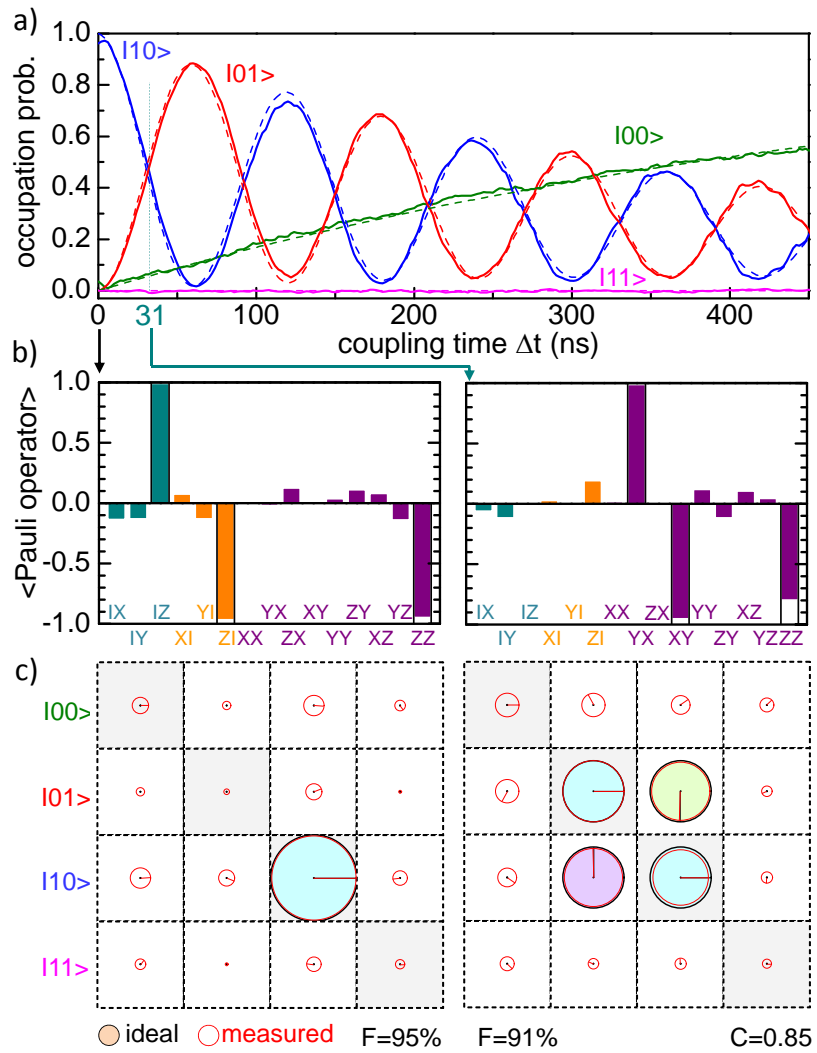


Figure 1.4: Energy oscillations between the two qubits induced by a resonant swapping interaction between them. a) The qubit state after switching on the swapping interaction for a given time Δt . The frequency of the oscillations corresponds to $2g = 8.7$ MHz. b) The Pauli set of the two-qubit state measured at 0 ns and 31 ns. c) The reconstructed density matrices corresponding to the two measured Pauli sets. In c), the area of each circle corresponds to the absolute value of each matrix element and the color and direction of the arrow give the phase of each element. The black circles correspond to the density matrices of the ideal states $|10\rangle$ and $1/\sqrt{2}(|10\rangle + i|01\rangle)$, respectively. **Figure Comment 4: verify sign!**

characterize by performing quantum state tomography. The experimental reconstruction of the density matrix of such a Bell-state of the type $|\psi\rangle = 1/\sqrt{2}(|01\rangle + i|10\rangle)$ is shown in fig. 1.4b. The measured fidelity of the prepared state of 91 % and the concurrence of 85 % confirm that entanglement is present in the system. We also characterize the entanglement between the two qubits by measuring the so-called *Clauser-Horne-Shimony-Holt* operator (Clauser et al., 1969), which combines measurements of the state of the two qubits along different axes on the Bloch sphere and provides a test that can distinguish between classical correlation and quantum entanglement in a two-qubit system.

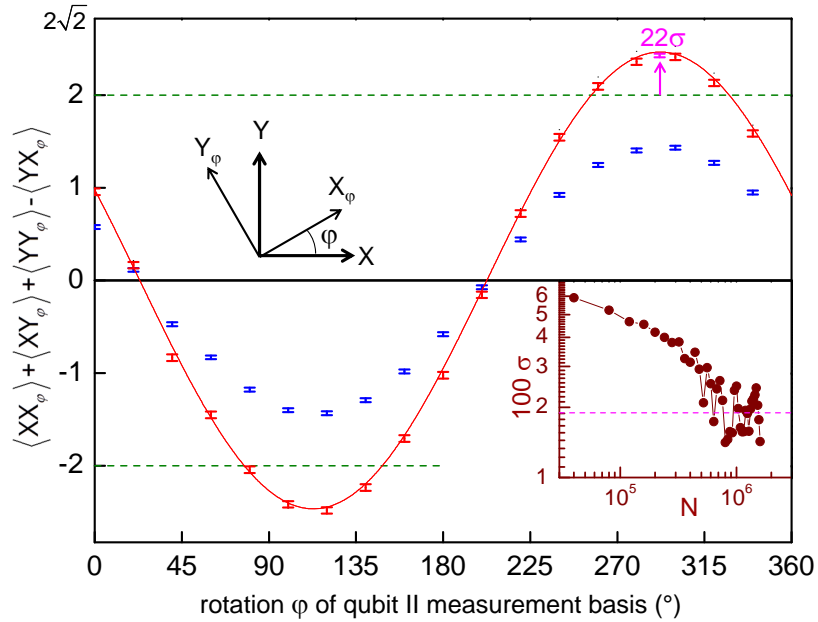


Figure 1.5: Measurement of the CHSH operator for an entangled two-qubit state. The renormalized CHSH expectation value (red points) exceeds the classical boundary of 2 by a large amount. The raw measurement data (blue points) lies below this critical threshold. The inset shows the standard deviation σ at the highest point of the curve as a function of the measurement sample size. For the highest sample count, the classical boundary is exceeded by 22 standard deviations. [Figure Comment 6: p. 140 in cavities 6 labbook](#)

For classical states, the maximum value of the CHSH operator is bound by 2 but for entangled states it can reach a maximum of $2\sqrt{2}$. Fig. 1.5 shows the result of such a CHSH-type measurement performed on a state created by the method described above, showing the value of $\langle \text{CHSH} \rangle$ as a function of the angle ϕ of the measurement basis (more details about the measurement and the preparation of the entangled state can be found in the main text). We observe a violation of the classical boundary 2 of the operator by 22 standard deviations when correcting the readout errors that are present in our system. The raw, uncorrected data fails to exceed the non-classical bound due to readout errors mainly caused by qubit relaxation during the readout. Nevertheless, the observed violation of the equation in the renormalized measurement data is a strong

indication of entanglement in the system.

1.5 Realizing a Universal Two-Qubit Quantum Gate

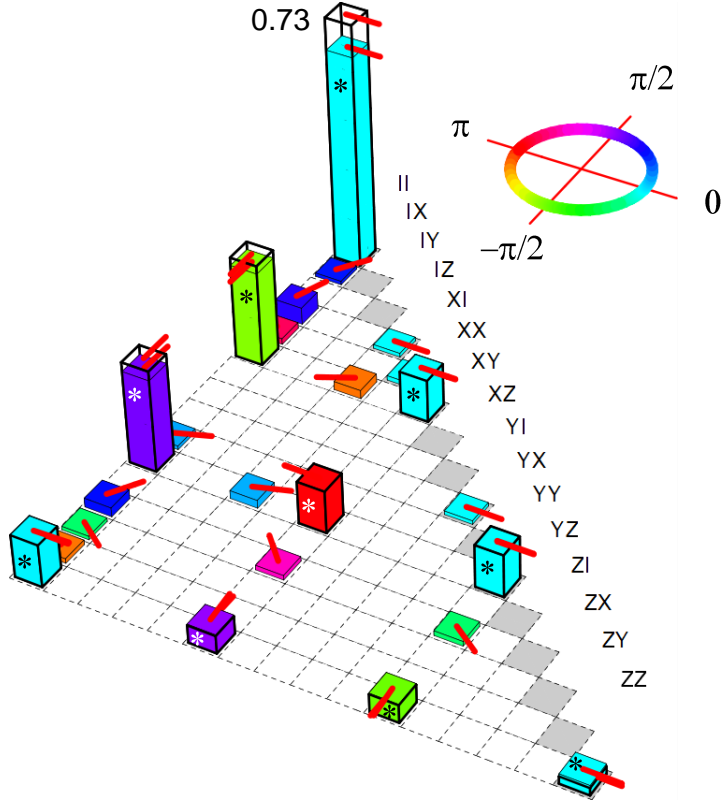


Figure 1.6: The measured χ -matrix of the implemented $\sqrt{i\text{SWAP}}$ gate. The row labels correspond to the indices of the E_i operators, the height of each bar to the absolute value of the corresponding matrix element and the color and direction of the red arrow to the complex phase of each element. The ideal χ -matrix of the $i\sqrt{\text{SWAP}}$ gate is given by the outlined bars. The upper half of the positive-hermitian matrix is not shown.

The swapping evolution given by eq. (1.1) allows not only the preparation of entangled two-qubit states but also the implementation of a two-qubit gate. When switching on the interaction for a time $t_{\pi/2} = 1/8g$ we can realize the so-called $\sqrt{i\text{SWAP}}$ gate, which has the representation

$$U(t) = \begin{pmatrix} 1 & 0 & 0 & 0 \\ 0 & 1/\sqrt{2} & i\sqrt{2} & 0 \\ 0 & i\sqrt{2} & 1/\sqrt{2} & 0 \\ 0 & 0 & 0 & 1 \end{pmatrix} \quad (1.2)$$

and is a universal two-qubit quantum gate. We characterize the operation and errors of our implementation of this gate by performing quantum process tomography, obtaining a gate fidelity of 90 %. The 10 % error in gate fidelity is caused mainly by qubit relaxation and dephasing during the gate operation and only marginally by deterministic preparation errors, as will be discussed in the main text of the thesis. Fig. 1.6 show the measured χ matrix of the gate, which contains the full information on the unitary and

non-unitary action of the gate. The achieved fidelity of the gate operation is sufficient to allow the implementation of a simple quantum algorithm with our processor, as will be discussed in the following section.

1.6 Running a Quantum Search Algorithm

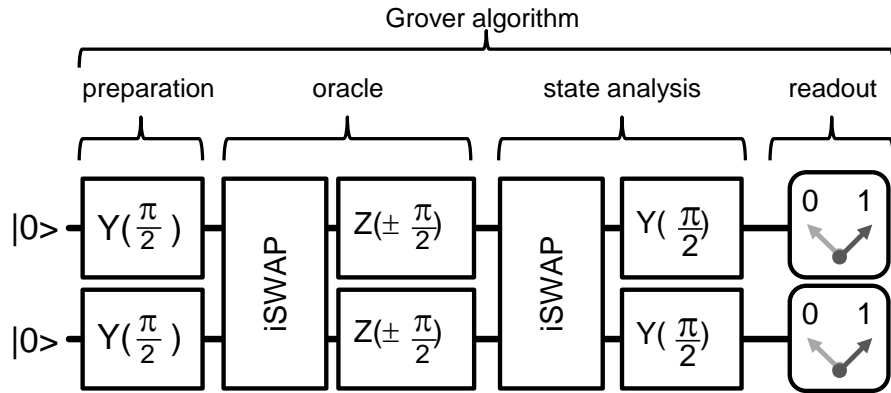


Figure 1.7: Schematic of the implementation of the Grover search algorithm on our two-qubit quantum processor. The algorithm consists in preparing a fully superposed state, applying the quantum Oracle operator to this state and analyzing the resulting output to determine the operator that has been applied with only a single call to the Oracle function.

We can use a two-qubit quantum gate derived from the one described above to run a simple quantum algorithm on our processor, the so called *Grover search algorithm* (Grover, 1997). The version of this algorithm that we implemented operates on a two-qubit basis $x_i \in \{ |00\rangle, |01\rangle, |10\rangle, |11\rangle \}$ and can distinguish between four different *Oracle functions* $f(x)$ with $x \in x_i$ that each tag one given basis state x_j . In the two-qubit case, this algorithm requires only one evaluation of the Oracle function $f(x)$ to determine which state has been marked by the Oracle operator and is therefore faster than any classical algorithm, which would need at most three evaluations of the Oracle function to determine it with certainty. Therefore, it demonstrates the concept of quantum speed-up in a straightforward and intuitive way. The schematic of our version of the Grover algorithm is shown in fig. 1.7 and involves two *iSWAP* gate operations and six single-qubit operations along with a single-shot qubit readout at the end of the algorithm. We implemented this algorithm with our two-qubit processor and performed quantum state tomography after each step to reconstruct the quantum state at different points in the algorithm.

Fig. 1.8 shows the experimentally measured density matrices when running this algorithm with an Oracle operator that marks the state $|00\rangle$. State tomographies are shown after applying a generalized Hadamard transform to the initial state $|00\rangle$, after

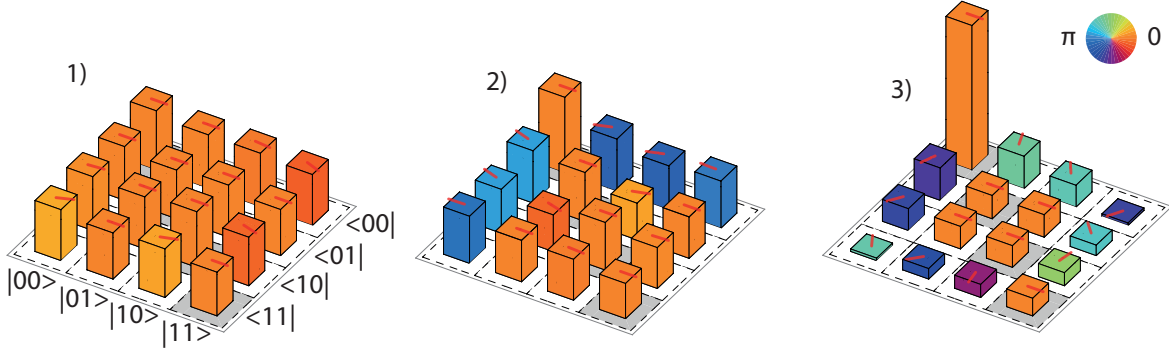


Figure 1.8: Measured density matrices when running the Grover search algorithm with a search oracle marking the state $|00\rangle$. 1) shows the state after the generalized Hadamard transform, 2) after applying the quantum oracle and 3) after the final step of the algorithm.

evaluating the quantum Oracle function and after the final step of the algorithm. The measured state tomographies after the final state of the algorithm yield state fidelities of 68%, 61%, 64% and 65% for the four different Oracle functions, respectively. These fidelities have been corrected for readout errors and therefore do not quantify the quantum speed-up that can be achieved when running this algorithm with our processor. For this it is necessary to analyze the uncorrected single-shot readout outcomes, which we will do in the next section, showing that it is possible to demonstrate a form of probabilistic quantum speed-up with our processor.

1.7 Demonstrating Quantum Speed-Up

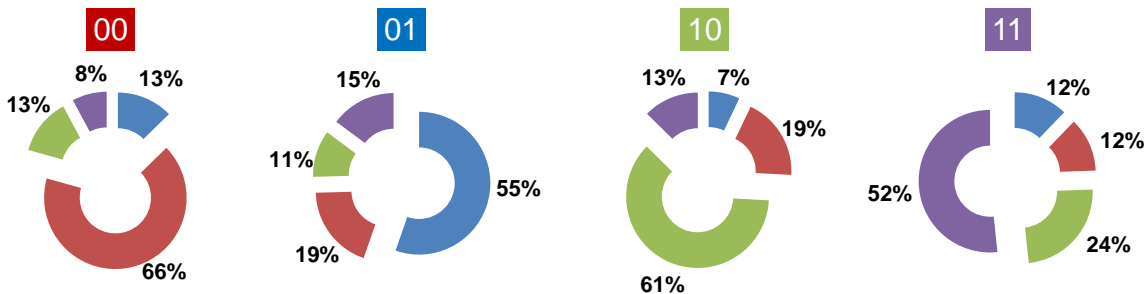


Figure 1.9: Single-run results when running the Grover search algorithm on our two-qubit quantum processor. Shown are the probabilities of obtaining the results 00, 01, 10, 11 as a function of the Oracle function provided to the algorithm, indicated by the number on top of each graph. In all four cases, the success probability of the algorithm is $> 50\%$, thus outperforming any classical query-and-guess algorithm in the required number of calls to the Oracle function.

The main interest of running a quantum algorithm is to obtain an advantage in the run-time in comparison to a classical algorithm, the so-called *quantum speed-up*. To

characterize this quantum speed-up as obtained with our processor, we run the Grover algorithm for all four possible Oracle functions and directly read out the state of the qubit register after the last step of the algorithm instead of performing quantum state tomography, thus not correcting any readout errors. By averaging the outcomes of many such individual runs of the algorithm with different Oracle functions we obtain the so-called *single-run fidelities*, which –for the four different Oracle functions– have been measured as 66%, 55%, 61% and 52%. The full probability distributions for the four possible cases and are shown in fig. 1.9. The measured success probabilities that are $> 50\%$ demonstrate the probabilistic quantum speed-up achieved with our processor compared to a classical query-and-guess algorithm that would be able to give the correct answer with only 50% single-run fidelity (a detailed explanation of this value can be found in the section on the Grover search algorithm in the main part of this thesis). The achieved success probabilities still are considerably lower than the theoretically possible values of 100 % , where the errors are mainly due to relaxation and decoherence of the qubit state during the runtime of the algorithm and to a small degree also due to errors in the pulse sequence.

Chapter 2

Theoretical Foundations

The goal of this chapter is to provide the theoretical foundations needed to interpret and analyze the experiments discussed in the following chapters. We will therefore briefly introduce some basic concepts of quantum mechanics and quantum computing, discuss Transmon qubits and circuit quantum electrodynamics (CQED) and introduce the reader to the Josephson bifurcation amplifier that we use to read out the qubit state in our experiments. Further details on all the elements discussed here will be provided in the relevant sections of the “Experiments” chapter.

2.1 Clasical & Quantum Information Processing

By definition, computing designates the activity of using computer hardware and software to process information, or *data*. Classical information processing can be divided in so-called *analog and digital information processing*, the former being based on continuously changeable physical quantities whereas the latter is based on incrementally changeable quantities. The fundamental unit of digital information processing is the so-called *bit*, which represents a boolean (true/false) information. The discipline of theoretical computer science has been created to investigate the fundamental limits and properties of classical information processing. One of the main foundational theorems of theoretical computer science is the so-called *Church-Turing thesis* which provides a universal computing model by saying (basically) that everything which is computable can be efficiently computed using a *Turing machine*. Such a Turing machine, in turn, is a simple theoretical devices which is able to run programs that operates on a discrete set of data using a well-specified set of operations. The Turing machine is universal in the sense that any other classical computing device can be efficiently simulated using a Turing machine with the appropriate program and data.

Surprisingly, Richard Feynman discovered in the early 1980 that a classical Turing machine as described above would be unable to efficiently simulate a quantum-

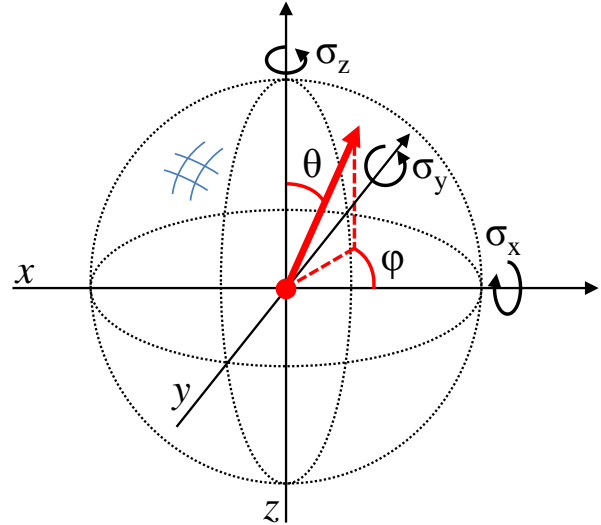


Figure 2.1: The Bloch sphere representation of a qubit state $|\psi\rangle = \cos \frac{\theta}{2} |0\rangle + e^{i\phi} \sin \frac{\theta}{2} |1\rangle$. The state $|\psi\rangle$ is fully characterized by specifying its “altitude” and “azimuth” angles θ and ϕ . Pure quantum states will always lie on the surface of the Bloch sphere, whereas mixed quantum states can also lie anywhere inside the sphere.

mechanical system (Feynman, 1982). A few years later, David Deutsch took up Feynman’s idea and developed an information processing framework based on quantum mechanics. He showed that by using this so-called *quantum computing* or *quantum information processing* framework one could solve certain problems faster than would be possible with any classical Turing machine (Deutsch, 1985). The work by Feynman and Deutsch created a large interest in the physics community and led to a huge experimental and theoretical effort aimed at realizing a working quantum computer.

2.2 Principles of Quantum Computing

2.2.1 Quantum Bits

Similar to classical computing, in quantum computing one can define a fundamental unit of information, the so called *quantum bit* or *qubit*. Such a qubit is a quantum-mechanical two-level system described by the wavefunction

$$|\psi\rangle = \cos \frac{\theta}{2} |0\rangle + e^{i\phi} \sin \frac{\theta}{2} |1\rangle \quad (2.1)$$

As can be seen, the state of such a qubit can be described by a pair of real numbers θ and ϕ that characterize the occupation probability of each of the two basis states $|0\rangle$ and $|1\rangle$ and the phase between them. A useful and intuitive representation of such a single-qubit state is the so-called *Bloch sphere representation* of a quantum state, which is shown in fig. 2.1. In this representation, the state $|\psi\rangle$ is located on a unit sphere. The north and south poles of this sphere correspond to the qubit states $|0\rangle$ and $|1\rangle$. All states lying between those two correspond to superposition states, which are characterized by their “altitude” and “azimuth” angles θ and ϕ .

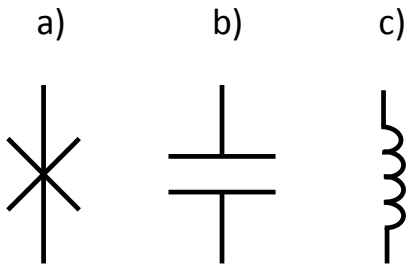


Figure 2.2: The three main circuit elements that are used to construct superconducting quantum circuits. Shown are a) a Josephson junction, b) an inductor and c) a capacitor.

2.2.2 Quantum Gates

Analogously to classical information processing it is necessary to define *quantum gates* which act on individual or multiple qubits and allow us to process information with them. In the most general sense, a quantum gate is a unitary quantum operator that acts on one or several qubits. Theoretically there is an infinite number of possible quantum gates, however in order to describe all possible quantum operations that can be performed on a register of qubits it is sufficient to define an *universal set of quantum gates*. Such a universal gate set that will be especially relevant to this work consists of the three single-qubit rotation matrices

$$R_x(\theta) = \begin{pmatrix} \cos \theta/2 & -i \sin \theta/2 \\ -i \sin \theta/2 & \cos \theta/2 \end{pmatrix} \quad (2.2)$$

$$R_y(\theta) = \begin{pmatrix} \cos \theta/2 & -\sin \theta/2 \\ +\sin \theta/2 & \cos \theta/2 \end{pmatrix} \quad (2.3)$$

$$R_z(\theta) = \begin{pmatrix} e^{-i\theta/2} & 0 \\ 0 & e^{+i\theta/2} \end{pmatrix} \quad (2.4)$$

together with the so-called *iSWAP* two-qubit operator, which has the representation

$$i\text{SWAP} = \begin{pmatrix} 1 & 0 & 0 & 0 \\ 0 & 0 & -i & 0 \\ 0 & -i & 0 & 0 \\ 0 & 0 & 0 & 1 \end{pmatrix} \quad (2.5)$$

in the basis $(|00\rangle, |01\rangle, |10\rangle, |11\rangle)$. Often we will represent these gates schematically as shown in fig. ??.

2.3 Superconducting Quantum Circuits

In this section we will discuss several types of superconducting circuits that are most relevant to this work. We will start our discussion by introducing a general framework for treating classical circuit components such as inductances and capacitors quantum-mechanically and introduce the Josephson junction, the key element used to realize superconducting qubits.

2.3.1 The Josephson junction

The core element used to construct quantum circuits is the so-called *Josephson junction*, being equivalent to the transistor in classical circuits in significance. A Josephson junction is based on a discovery of Brian Josephson, which published a now-classical paper on quantum tunneling between weakly coupled superconductors (Josephson, 1962). He found, that such a *weak link* between two superconductors could support a supercurrent I described by the simple formula

$$I = I_c \sin \phi \quad (2.6)$$

where $\phi = \phi_2 - \phi_1$ and ϕ_1 and ϕ_2 are the superconducting phases at each side of the link. This simple equation, together with the current-phase relation of a Josephson junction,

$$U = \frac{\hbar}{2e} \frac{\partial \phi}{\partial t} \quad (2.7)$$

yields a system exhibiting a wealth of interesting physical phenomena that are used today in various applications in physics. The energy associated with the Josephson junction is given as

$$E = E_J(1 - \cos \phi) \quad (2.8)$$

where $E_J = I_c \Phi_0 / 2\pi$ is the so-called *Josephson energy*. In addition to this Josephson energy, the junction usually has an energy associated to the capacitance formed by the two separated electrodes of the junction and given as $E_c = Q^2 / 2C$.

For currents $I \ll I_c$, a Josephson junction behaves approximatively like a nonlinear inductor with inductance

$$L_J = \frac{\Phi_0}{2\pi I_c \cos \phi} \quad (2.9)$$

where $\Phi_0 = h/2e \approx 2.05 \times 10^{-15}$ Wb is the so-called *magnetic flux quantum*. Later we will show how to make use of the properties of the Josephson junction to construct a qubit with it.

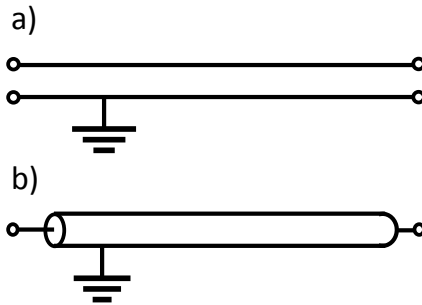


Figure 2.3: a) The circuit diagram of a grounded transmission line. b) The circuit diagram of a grounded coaxial transmission line.

2.3.2 Transmission Lines

Another circuit element that we will encounter many times in this work is the so-called *transmission line*. In the most general way, a transmission line is a structure with a large extension in one direction which is capable of transmitting electromagnetic waves along itself. Two possible symbols by which one usually designates transmission lines in a circuit schematic are shown in fig. ???. A detailed treatment of the physics of transmission lines can be found e.g. Pozar (2011). For this introduction we will skip these basics and start directly with the equation that describes the propagation of an electromagnetic wave along the extended dimension z of the transmission line and which is given as

$$V(z, t) = \exp(i\omega t) \cdot (V^+ \exp(-i\gamma z) + V^- \exp(i\gamma z)) \quad (2.10)$$

$$I(z, t) = \frac{1}{Z_0} \exp(i\omega t) \cdot (V^+ \exp(-i\gamma z) - V^- \exp(i\gamma z)) \quad (2.11)$$

Here, $\gamma = \alpha + i\beta = \sqrt{(R + i\omega L)(G + i\omega C)}$ is the so-called *propagation constant* which describes the dispersion and damping of electromagnetic waves along the transmission line and ω the circular frequency of the electromagnetic wave. The voltages V^+ and V^- correspond to waves traveling in different directions along the waveguide.

If we regard a CPW of fixed length l , we can model the voltages and currents at its end by using the formula(Pozar, 2011)

$$\begin{pmatrix} V_1 \\ I_1 \end{pmatrix} = \begin{pmatrix} \cos \gamma l & iZ_r \cos \gamma l \\ iY_r \sin \gamma l & \cos \gamma l \end{pmatrix} \cdot \begin{pmatrix} V_2 \\ I_2 \end{pmatrix} \quad (2.12)$$

2.3.3 Transmission Line Resonators

One can easily create a resonator using a coplanar waveguide as described in the last section. As an example, we will discuss an open-ended $\lambda/2$ CPW resonator that is used in our experiments as well and thus highly relevant to this work. To create a resonator out of a CPW line, we terminate the line by an open and connect it to a drive line through an input capacitance C , as shown in fig. ???. To calculate the voltages and

currents going into the CPW resonator, we can use eq. (2.12). Since the far end of the resonator is open we demand that $I_2 = 0$ and thus obtain for the voltage V_1 and current I_1 the relation

$$V_1 = \cos \gamma l V_2 \quad (2.13)$$

$$I_1 = iY_r \sin \gamma l V_2 \quad (2.14)$$

Hence, the impedance of the resonator is given as $Z_{res} = V_1/I_1 = iZ_r \cot \gamma l$, where Z_r is the impedance of the transmission line of which the resonator is made of. We couple this resonator to an input line through a gate capacitance C_g , thus the impedance seen from the input of the circuit is given as

$$Z_{in} = iZ_r \cot \gamma l - \frac{i}{\omega C_g} \quad (2.15)$$

It is straightforward to calculate the S_{11} reflection coefficient of the resonator when coupling it to an input line with impedance Z_0 as

$$S_{11} = \frac{Z_{in} - Z_0}{Z_{in} + Z_0} = \frac{Z_r \cot \gamma l - / \omega C_g - Z_0}{Z_r \cot \gamma l - / \omega C_g + Z_0} \quad (2.16)$$

Now, when measuring the reflection of an incoming signal with voltage V^+ at frequency $f = 2\pi\omega$ and phase ϕ_0 , the phase of the reflected signal ϕ_{ref} will be simply given as $\phi_{ref} = \text{Arg}[V^-/V^+] - \phi_0 = \text{Arg}[S_{11}] - \phi_0$. Fig ?? shows this phase for an exemplary resonator, plotted for $f = 2\pi\omega$ in reduced units of $[l/v]$, with impedances $Z_r, Z_0 = 50 \Omega$, $\alpha = 0$ and with the resonator coupled to the input line through a normalized capacitance $C_g = 10^{-3}/\omega$ [Hz · F].

We can calculate the quality factor of such an open-ended CPW resonator by modeling it as a series-LC circuit. Indeed, if we regard the input impedance of the resonator in the vicinity of ω_0 such that $\Delta\omega = \omega - \omega_0$ with $\Delta\omega \ll \omega_0$ and $\beta l = \pi + \pi\Delta\omega/\omega_0$, we obtain an effective impedance

$$Z_{in} = \frac{Z_r}{\alpha l + i(\Delta\omega\pi/\omega_0)} \quad (2.17)$$

We can identify the quantities in this equation with the input impedance of a parallel LCR-resonator, which at $\omega \approx \omega_0$ is approximatively given as

$$Z_{in} = \frac{R}{1 + 2iQ\Delta\omega/\omega_0} \quad (2.18)$$

with $W = \omega_0 RC$. This yields an effective resistance, inductance and capacitance for the

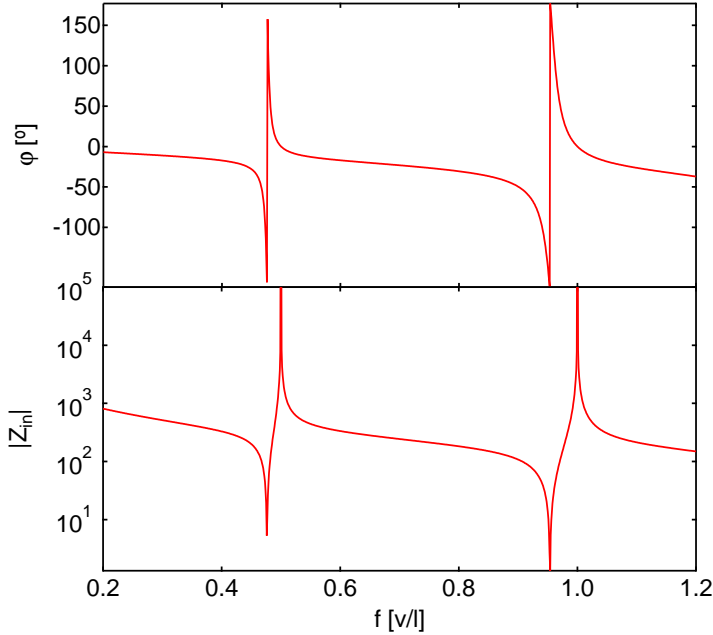


Figure 2.4: This is the side caption which is maybe already to small to support such long text..

transmission line resonator of

$$R_r = \frac{Z_r}{\alpha l} \quad (2.19)$$

$$L_r = \frac{1}{\omega_0^2 C} \quad (2.20)$$

$$C_r = \frac{\pi}{2\omega_0 Z_r} \quad (2.21)$$

When coupling this resonator to an input transmission line of impedance Z_0 through a gate capacitance C_g as before, the quality factor of the coupled (or *loaded*) resonator will be given as (Göppl et al., 2008)

$$Q_L = \omega_0^* \frac{C + C^*}{1/R_r + 1/R^*} \quad (2.22)$$

where we have introduced an effective resistance, capacitance and resonance frequency given as

$$R^* = \frac{1 + \omega_0^2 C_g^2 Z_0^2}{\omega_0^2 C_g^2 Z_0} \quad (2.23)$$

$$C^* = \frac{C_g}{1 + \omega_0^2 C_g^2 Z_0^2} \quad (2.24)$$

$$\omega_0^* = \frac{1}{\sqrt{L_r(C_r + C_g)}} \quad (2.25)$$

Thus, we can effectively tune the quality factor of the resonator by changing the gate

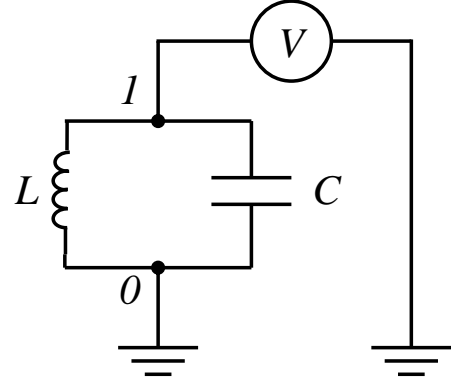


Figure 2.5: An exemplary superconducting circuit made of a Josephson junction, a capacitor and a voltage source. The circuit topology can be described by one node (plus ground) and one branch.

capacitance by which we couple it to the input transmission line.

2.3.4 Quantization of Electrical Circuits

In this section we will outline a general method to treat arbitrary electrical circuits as the ones discussed before within the framework of quantum-mechanics, hence *quantizing* them. This introduction on circuit quantization presented in this chapter is based on an article by Devoret (1995).

Fig. 2.6 shows an exemplary circuit made of a Josephson junction, a capacitor and a voltage source. A circuit as this one is fully characterized by the parameters of its elements and its topology. The latter can be described – following the laws of Kirchhoff – as a set of nodes connected by a number of branches. In classical circuit theory, each branch i is described by a voltage V_i and a current I_i flowing through it. The Kirchhoff laws demand that the sum of the branch voltages V_i along any closed path must be zero, i.e. $\sum_i V_i = 0$. Equivalently one may demand that the sum of currents flowing in and out of each node must be zero. For the quantization of electrical circuits it is usually more convenient to replace voltages and currents with branch charges and fluxes that are defined as

$$\Phi_i(t) = \int_{-\infty}^t V_i(t') dt' \quad (2.26)$$

$$Q_i(t) = \int_{-\infty}^t I_i(t') dt' \quad (2.27)$$

In analogy with the Kirchhoff laws for the sums of currents and voltages along a closed branch, we can formulate a Kirchhoff law for the charges Q_i at each node of the circuit,

given as

$$\sum_i Q_i = Q_0 \quad (2.28)$$

where Q_0 is constant . To quantize such a circuit made up of non-dissipative elements we can follow the method given in Yurke and Denker (1984), writing the Lagrangian of the circuit as

$$\mathcal{L} = \sum_i V_i - \sum_i T_i \quad (2.29)$$

where V_i and T_i are the potential and kinetic energies associated to each circuit element.

!6! . For a circuit composed entirely of capacitors and inductor, the Lagrangian is given as

$$\mathcal{L} = \frac{1}{2} \sum_i \frac{Q_i^2}{C_i} - \frac{1}{2} \sum_i L \left(\frac{dQ_i}{dt} \right)^2 \quad (2.30)$$

To Do 6: Clarify why kinetic energy is mapped to capacitive energy and potential energy to inductive energy

If needed, resistors can be described within the Lagrangian formalism by modeling them as transmission lines with a characteristic impedance matching their resistance (Yurke and Denker, 1984). From the Lagrangian as given in eq. (2.30) we obtain then the equations of motion of the system by variation of the action

$$\frac{\partial}{\partial t} \left(\frac{\partial \mathcal{L}}{\partial (\partial_t Q_i)} \right) - \frac{\partial \mathcal{L}}{\partial Q_i} = 0 \quad (2.31)$$

By imposing the charge-conservation equations as given by eq. (2.28) we obtain then a complete description of the underlying circuit. From the variable Q_i we obtain the canonically conjugate momentum Φ_i by solving the equation

$$\Phi_i = \frac{\partial \mathcal{L}}{\partial (\partial_t Q_i)} \quad (2.32)$$

First Quantization of the circuit variables can then be done by imposing commutation relations between the set of canonical variables Q_i and Φ_i such that

$$[Q_i(t), Q_j(t')] = 0 \quad (2.33)$$

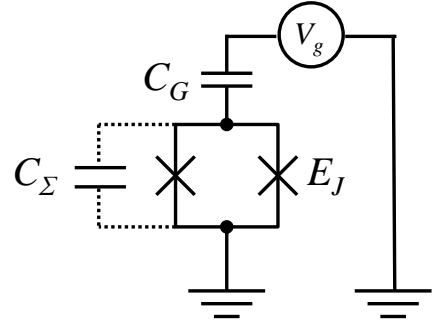
$$[\Phi_i(t), \Phi_j(t')] = 0 \quad (2.34)$$

$$[Q_i(t), \Phi_j(t')] = i\hbar\delta_{ij}\delta(t - t') \quad (2.35)$$

Having obtained Φ_i and Q_i , it is also trivial to obtain the Hamiltonian \mathcal{H} of the system by applying the transformation

$$\mathcal{H} = \sum_j \Phi_i \dot{Q}_i - \mathcal{L} \quad (2.36)$$

Figure 2.6: The circuit schematic of a Split Cooper Pair Box. The device consists of two Josephson junctions arranged in a loop, where the capacitance of the junctions is modeled as the extra capacitor indicated on the left. By putting the two junctions in series with a gate capacitance one creates an island one which charges can accumulate. The gate voltage can be controlled by an external voltage source.



2.3.5 The Cooper Pair Box

A Transmon qubit is essentially a Cooper pair box (CPB) operated in the phase regime, where $E_J \gg E_C$. The Hamiltonian of the CPB can be written as (Cottet, 2002)

$$\hat{H} = 4E_C (\hat{n} - n_g)^2 - E_J \cos \hat{\phi} \quad (2.37)$$

where $E_C = e^2/C_\Sigma$ is the charging energy with $C_\Sigma = C_J + C_B + C_g$ the total gate capacitance of the system, \hat{n} is the number of Cooper pairs transferred between the islands, n_g the gate charge, E_J the Josephson energy of the junction and $\hat{\phi}$ the quantum phase across the junction.

The corresponding wavefunction $\Psi_k(\theta) = \langle \theta, k \rangle$ will then satisfy the Schrödinger equation

$$E_k \Psi_k(\theta) = E_C \left(\frac{1}{i} \frac{\partial}{\partial \theta} - n_g \right)^2 \Psi_k(\theta) - E_J \cos(\theta) \Psi_k(\theta) \quad (2.38)$$

Since the potential $E_J \cos(\theta) \Psi_k(\theta)$ is periodic, we may demand that the solution will also exhibit a periodicity of the form

$$\Psi_k(\theta) = \Psi_k(\theta + 2\pi) \quad (2.39)$$

As it turns out, eq. (2.38) can be mapped easily to the so-called *Mathieu differential equation*, which is given as

$$\frac{d^2y}{dx^2} + [a - 2q \cos(2x)] y = 0 \quad (2.40)$$

Applying *Floquet's theorem* to this equation it can be shown that there exist solutions of the form

$$F(a, q, x) = \exp(i\mu x) P(a, q, x) \quad (2.41)$$

The most general solutions to eq. (2.38) are given as (Cottet, 2002)

$$\Psi_k(r, q, \theta) = C_1 \exp(in_g\theta) \mathcal{M}_C \left(\frac{4E_k}{E_C}, -\frac{2E_J}{E_C}, \frac{\theta}{2} \right) + C_2 \exp(in_g\theta) \mathcal{M}_S \left(\frac{4E_k}{E_C}, -\frac{2E_J}{E_C}, \frac{\theta}{2} \right) \quad (2.42)$$

with

$$E_k = \frac{E_C}{4} \mathcal{M}_A \left(r, -\frac{2E_J}{E_C} \right) \quad (2.43)$$

Here, \mathcal{M}_C , \mathcal{M}_S are the *Mathieu functions* and \mathcal{M}_A corresponds to the eigenvalue. This Hamiltonian can be solved exactly in the phase basis with the solutions being given as (Koch et al., 2007; Cottet, 2002)

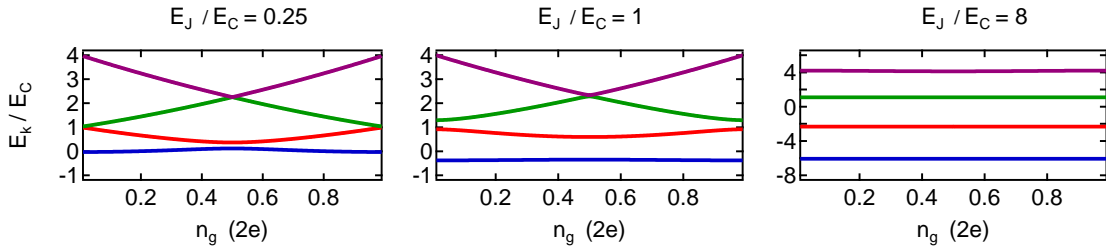


Figure 2.7: Energies of the first four energy level of the Cooper pair box for different ratios E_J/E_C , plotted as a function of the gate charge n_g . As can be seen, for $E_J \ll E_C$, the charge-dispersion curve becomes almost completely flat.

$$E_m(n_g) = E_C a_{2[n_g+k(m,n_g)]}(-E_J/E_C) \quad (2.44)$$

Here, $a_\nu(q)$ denotes Mathieu's characteristic value and $k(m, n_g)$ is a function that sorts the eigenvalues. We denote the energy differences between individual energy level by $E_{ij} = E_j - E_i$. We also define the absolute and relative anharmonicities of the first two energy levels as $\alpha_{12} \equiv E_{12} - E_{01}$ and $\alpha_r \equiv \alpha/E_{01}$. In the limit $E_J \gg E_C$ these anharmonicities are well approximated by $\alpha \simeq -E_C$ and $\alpha_r \simeq -(8E_J/E_C)^{-1/2}$.

2.4 The Transmon Qubit

The Transmon qubit is a Cooper pair box operated in the regime where $E_J \gg E_C$. As shown above, in this regime the charge dispersion of the energy levels of the Cooper pair box becomes flat, thus rendering the transition frequency E_{01} almost insensitive to the value of the gate charge n_g . This reduced sensitivity to charge noise is highly advantageous in experiments. However, when increasing the ratio E_J/E_C , we also reduce the anharmonicity α_r of the qubit, therefore limiting the speed of gate operations that can be realized with this system (driving errors related to weak anharmonicity will be discussed more thoroughly in the Experiments section of this thesis). Remarkably

though, α_r decreases only geometrically with E_J/E_C , whereas the sensitivity of the qubit to charge noise decreases exponentially with the ratio of Josephson and charging energy. Fig ?? shows the relaxation rate and relative anharmonicity of a Cooper Pair box for different values of E_J/E_C . As can be seen,

2.5 Circuit Quantum Electrodynamics

For readout and noise protection, the Transmon qubit is usually coupled to a harmonic oscillator which is usually realized as a lumped-elements resonator or a coplanar waveguide resonator. In the limit where the resonator capacity $C_r \gg C_\Sigma$ we can write the effective Hamiltonian of the system as

$$\hat{H} = \hbar \sum_j \omega_j |j\rangle \langle j| + \hbar \omega_r \hat{a}^\dagger \hat{a} + \hbar \sum_{i,j} g_{ij} |i\rangle \langle j| (\hat{a} + \hat{a}^\dagger) \quad (2.45)$$

Here, $\omega_r = 1/\sqrt{L_r C_r}$ gives the resonator frequency and \hat{a} (\hat{a}^\dagger) are annihilation (creation) operators acting on oscillator states. The voltage of the oscillator is given by $V_{rms}^0 = \sqrt{\hbar \omega_r / 2C_r}$ and the parameter β gives the ratio between the gate capacitance and total capacitance, $\beta = C_g/C_\Sigma$. The coupling energies g_{ij} are given as

$$\hbar g_{ij} = 2\beta e V_{rms}^0 \langle i | \hat{n} | j \rangle = \hbar g_{ji}^* \quad (2.46)$$

When the coupling between the resonator and the Transmon is weak $g_{ij} \ll \omega_r, E_{01}/\hbar$ we can ignore the terms in eq. (2.45) that describe simultaneous excitation or deexcitation of the Transmon and the resonator and obtain a simpler Hamiltonian in the so-called *rotating wave approximation* given as

$$\hat{H} = \hbar \sum_j \omega_j |j\rangle \langle j| + \hbar \omega_r \hat{a}^\dagger \hat{a} + \left(\hbar \sum_i g_{i,i+1} |i\rangle \langle i+1| \hat{a}^\dagger + H.c. \right) \quad (2.47)$$

2.5.1 Dispersive Limit & Qubit Readout

When the qubit frequency is far detuned from the resonator frequency direct qubit-resonator transition get exponentially suppressed and the only interaction left between the two system is a dispersive shift of the transition frequencies. In this limit, the effective Hamiltonian of the system can be written as (Blais et al., 2004; Koch et al., 2007)

$$\hat{H}_{eff} = \frac{\hbar \omega'_{01}}{2} \hat{\sigma}_z + \hbar(\omega'_r + \chi \hat{\sigma}_z) \hat{a}^\dagger \hat{a} \quad (2.48)$$

Here, the resonance frequencies of both the qubit and the resonator are shifted and given as $\omega'_r = \omega_r - \chi_{12}/2$ and $\omega'_{01} = \omega_{01} + \chi_{01}$. The dispersive shift χ itself is given as

$$\chi = \chi_{01} - \chi_{12}/2 \quad (2.49)$$

$$\chi_{ij} = \frac{g_{ij}^2}{\omega_{ij} - \omega_r} = \frac{(2\beta e V_{rms}^0)^2}{\hbar^2 \Delta_i} |\langle i | \hat{n} | i+1 \rangle|^2 \quad (2.50)$$

The fact that χ_{01} and χ_{12} contribute to the total dispersive shift can cause the overall dispersive shift to become negative and even diverge at some particular working points.

2.6 The Josephson Bifurcation Amplifier

(Palacios-Laloy, 2010)

$$[L_e + L_J(i)]\ddot{q} + R_e \dot{q} + \frac{q}{C_e} = V_e \cos(\omega_m t) \quad (2.51)$$

Expanding this to second order in L_J leads to the expression

$$\left(L_e + L_J \left[1 + \frac{\dot{q}^2}{2I_0^2} \right] \right) \ddot{q} + R_e \dot{q} + \frac{q}{C_e} = V_e \cos(\omega_m t) \quad (2.52)$$

Defining the total inductance $L_t = L_e + L_J$, the participation ratio $p = L_J/L_t$, the resonance frequency $\omega_r = 1/\sqrt{L_t C_e}$ and the quality factor $Q = \omega_r L_t / R_e$ we can rewrite this as

$$\ddot{q} + \frac{\omega_r}{Q} \dot{q} + \omega_r^2 q + \frac{p \dot{q}^2 \ddot{q}}{2I_0} = \frac{V_e}{L_t} \cos(\omega_m t) \quad (2.53)$$

Chapter 3

Realizing a Two-Qubit Processor

This chapter discusses the main experimental results of this thesis. We start by discussing the implementation of a superconducting two-qubit processor, discussing the characteristics of the Transmon qubits used in the processor, the readout scheme, single-qubit manipulation, two-qubit gates as well as the experimental procedures used for quantum state and quantum process tomography. The last section of this chapter will discuss the implementation of a quantum algorithm – so called Grover search algorithm – using our two-qubit processor and the demonstration of quantum speed-up achieved with our system.

3.1 Introduction & Motivation

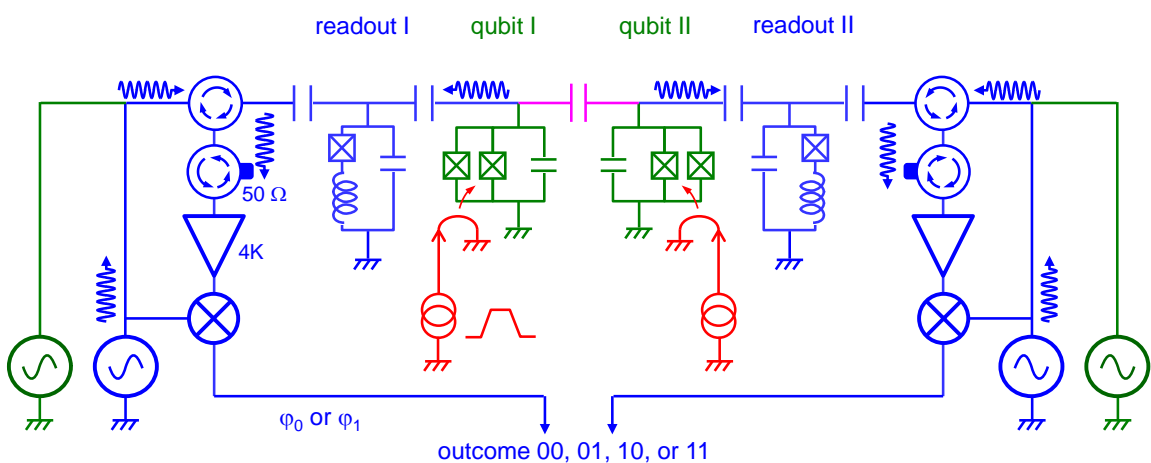


Figure 3.1: The circuit schematic of the two-qubit processor used in this work. Shown are the two Transmon qubits in green, the drive and readout circuit in blue, the fast flux lines in red and the coupling capacitance in magenta.

As discussed in the introduction, the most simple, usable quantum processor contains two qubits that are coupled by an universal two-qubit gate and which in addition

can be manipulated and read out individually. We realized such a two-qubit processor using two Transmon qubits, coupled through a fixed capacitance and readout out by individual single-shot readout of the JBA type. The circuit diagram of our processor is shown in fig. 3.1, showing the qubits, the drive and readout circuit and the coupling element between them. The following sections we'll discuss the parameters of individual parts of the processor.

3.2 Qubit Design

The parameters of the sample have been chosen in accordance to various design constraints of the qubit processor. For the qubits, the main design goals were high coherence time, good frequency tunability and fast drivability. As we will show later, the coherence time of the qubit is limited by relaxation to the ground state and coupling to external noise sources. The relaxation component of the Transmon qubit is ultimately limited by internal losses of the Josephson junction but usually is bound by coupling to the electromagnetic environment, as will be discussed later. The frequency tunability is important for the realization of fast two-qubit gates but can also limit the relaxation and coherence time of the qubit by coupling to external noise sources. The drivability speed on the other hand is limited by the anharmonicity of the qubit, which can however not be increased arbitrarily since it will make the qubit sensitive to charge noise when chosen too high. For the readout, the main design goals were readout speed and fidelity. The speed of the readout is limited by the quality factor of the readout resonator, which however also can induce qubit relaxation through the Purcell effect and may therefore not be chosen too small.

In the following paragraphs we'll therefore discuss the parameter design for our two-qubit processor and analyze the sample parameters that have been obtained.

3.3 Readout Design

3.4 Processor Fabrication

In this section we will discuss the fabrication of the two-qubit processor realized in this work.

Chapter 4

Measurement Setup

Fig. 4.1 show the measurement setup used for the two-qubit experiments. The different signal and measurement lines as well as the room-temperature and cryogenic microwave components used in our experiments will be described in the following paragraphs.

In this section we discuss the details of the measurement setup used to perform the two-qubit experiments presented in this thesis. All experiments have been performed in a custom-built dilution cryostat at $< 40 \text{ mK}$ using a cryogenic microwave signal generation and measurement chain. The individual components of this setup will be discussed in the following sections.

4.1 Sample Holder & PCB

The qubit chip is first glued to a high-frequency PCB !7!, then wirebonds are used to connect the groundplane and the center conductors of the on-chip transmission lines to their counterparts on the PCB. Finally, additional bond wires connect isolated ground planes on-chip. The realization of a good and uniform groundplane on the qubit chip and around is very important to suppress unwanted resonance modes that can be created when the connection between isolated ground planes is not good enough !8!. The mounted chip on the PCB is then placed in a Copper or Aluminium sample holder which fully encloses the PCB and serves to reduce unwanted couplings to the environment. The coplanar waveguides on the PCB are connected to Mini-SMP cables through a set of connectors that are soldered on the PCB.

To Do 7: add substrate material details

To Do 8: Add references e.g. to Schuster's thesis

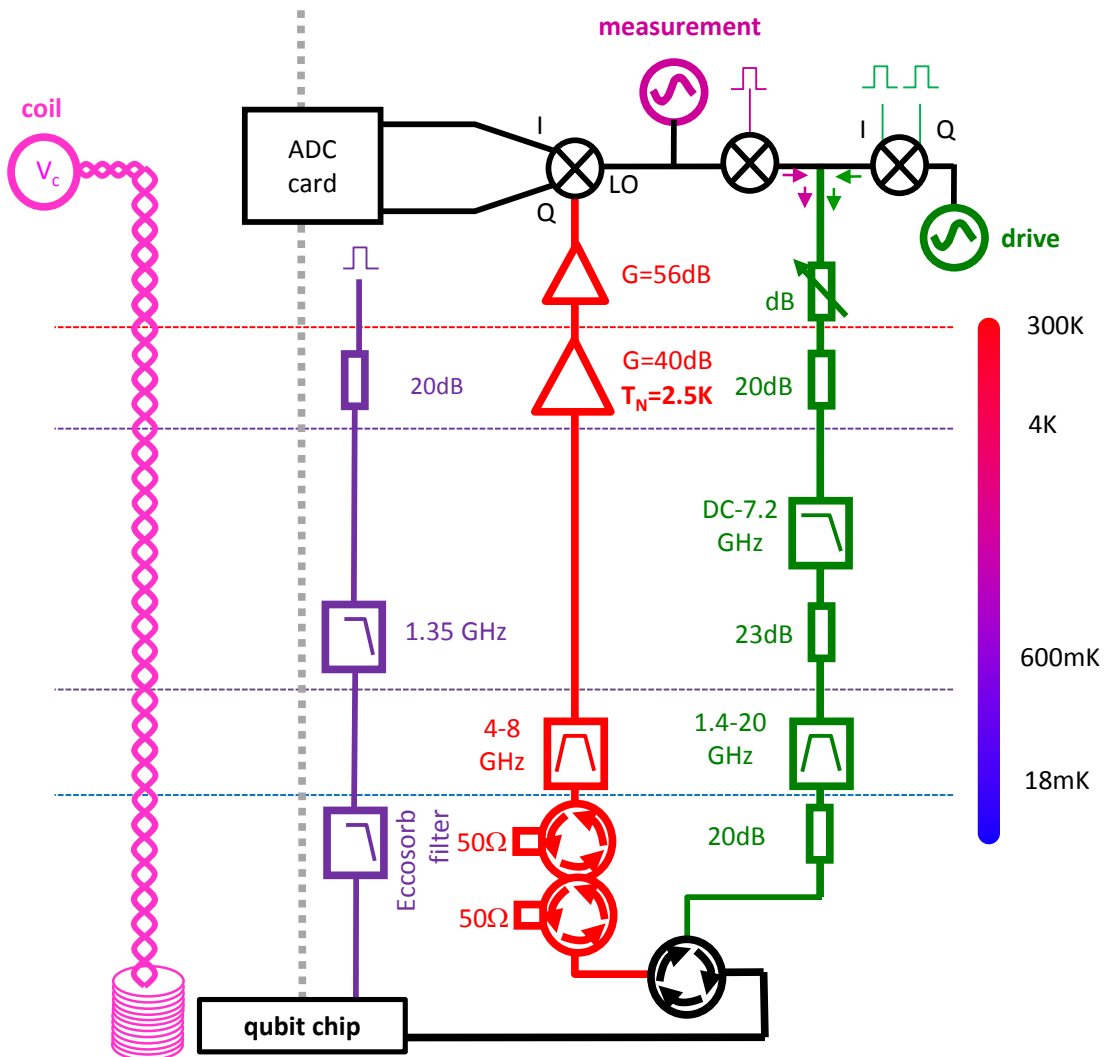


Figure 4.1: The measurement setup used for the two-qubit experiments. Exactly the same drive and readout scheme is used for both qubits with phase-locked microwave sources and arbitrary waveform generators.

4.2 Cryogenic Wiring

For the transmission of microwave signals to our sample we use various types of transmission lines suited for room-temperature and cryogenic application. The main goal of the input lines is to provide adequate signal transmission without introducing too much thermal conductance to the system. For the signal lines that carry the measurement signal from the sample we use superconducting cables [!9!](#) and low-resistance copper cables. In addition, we use superconducting bifilar cables for the DC bias of our magnetic coils. The qubit and fluxline input lines are attenuated and filtered at several stages of the cryostat to reduce signal noise.

To Do 9: add type

4.3 Signal Generation & Acquisition

Here we discuss the generation and acquisition of the different signals used to manipulate and read out our quantum processor. The experiments that have been performed require the generation, measurement and demodulation of microwave signals, the generation of fast flux control pulses and the application of DC currents to our magnetic coils.

4.3.1 Microwave Sideband Mixing

For qubit manipulation it is often advantageous to use single-sideband mixing for driving the qubit since it can provide higher ON/OFF ratios for microwave pulses and allow the driving of higher qubit-levels using a single, phase-coherent microwave source. To realize this, we use IQ mixers (Hittite !10!) that we drive with a continuous single-frequency microwave tone and two time-synchronized fast control signals generated by an arbitrary waveform generator (Tektronix AWG5014b). When feeding a signal $LO(t) = i_0 \cos(\omega_{rft}t)$ to the LO port of the mixer and two signals $I(t), Q(t)$ to the I and Q ports of the mixer one obtains a signal

$$RF(t) = I(t) \cos(\omega_{rft}t) + Q(t) \sin(\omega_{rft}t) \quad (4.1)$$

To Do 10: Add exact type number

at the LO port of the mixer. Since the IQ mixer that we use is a passive, reciprocal device one can as well feed two input signals to the LO and RF ports and obtain the demodulated signal quadratures at the I and Q ports, a technique that we'll make use of for our qubit readout scheme.

Commercially available IQ mixers often deviate from the ideal behavior as given by eq. (4.1). Typical imperfections include large insertion losses –i.e. loss of signal power between the different ports of the mixer–, RF signal leakage at zero IQ-input and frequency-dependent phase and amplitude errors of the mixed sideband signals. In order to achieve reliable single-qubit operations we need to correct the signal leakage and quadrature-specific amplitude and phase errors. The signal leakage causes a small part of the LO signal to leak through to the RF port even when the IQ inputs are zeroed. This leakage can be compensated by adding center-frequency ω_c dependent DC offset voltages to the IQ ports. The appropriate offset voltages can be determined by applying a continuous input signal at a frequency ω_c to the LO port of the mixer and minimizing the signal power at the RF port by varying the IQ offset voltages. To correct the sideband amplitude and phase errors we apply another correction procedure that we outline here. First, for the signals at the IQ inputs of the mixer we introduce the notation

$$A(t) = I(t) + iQ(t) = a(t) \exp(-i\phi(t)) \quad (4.2)$$

We consider an IQ signal at a single sideband frequency ω_{sb} and at fixed complex amplitude $a(t) = a = a_0 \exp(i\phi_0)$ such that $A(t) = a \exp(-i\omega_{sb}t)$. The effect of the gain and phase imperfections of the IQ mixers can then be modeled by assuming that the mixer adds another IQ signal $\epsilon(\omega_{sb}, \omega_c)A^*(t)$ at the mirrored sideband frequency $-\omega_{sb}$. We can correct this unwanted signal by adding a small correction $c(\omega_{sb}, \omega_c)A^*(t)$ to our IQ input signal. The correction coefficient $c(\omega_{sb}, \omega_c)$ usually depends both on the carrier frequency ω_c and the sideband frequency ω_{sb} . We determine the correction coefficients by generating a continuous waveform at a given center and sideband frequency, measuring the amplitude of the unwanted sideband signal with a fast spectrum analyzer and minimizing its amplitude by varying the correction coefficient $c(\omega_{sb}, \omega_c)$.

Both the offset and the sideband-amplitude and -phase corrections have been automatized using our data acquisition software, the resulting correction coefficients are summarized in fig. ??.

4.3.2 Fast Magnetic Flux Pulses

The fast flux lines are implemented by a pair of superconducting 50Ω transmission lines, which are attenuated by 20 dB and filtered at the 4K and 20 mK stages of the cryostat. The filtering at the 20 mK stage is realized through custom-made, highly absorptive Eccosorb filters. Fig. ?? shows an image of these filters and the attenuation characteristic obtained. The heavy filtering of the flux line greatly reduces noise seen by the qubit but also distorts all signals sent through the line. This distortion is unwanted especially at high frequencies and needs to be corrected. To do this we need to measure and compensate the frequency response of the flux line at experimental conditions. In order to do this, we feed back the flux signal sent to the sample through a transmission line which is exactly equivalent to the input line. This allows us to measure the returning signal at room temperature and – assuming symmetric distortion in the in-

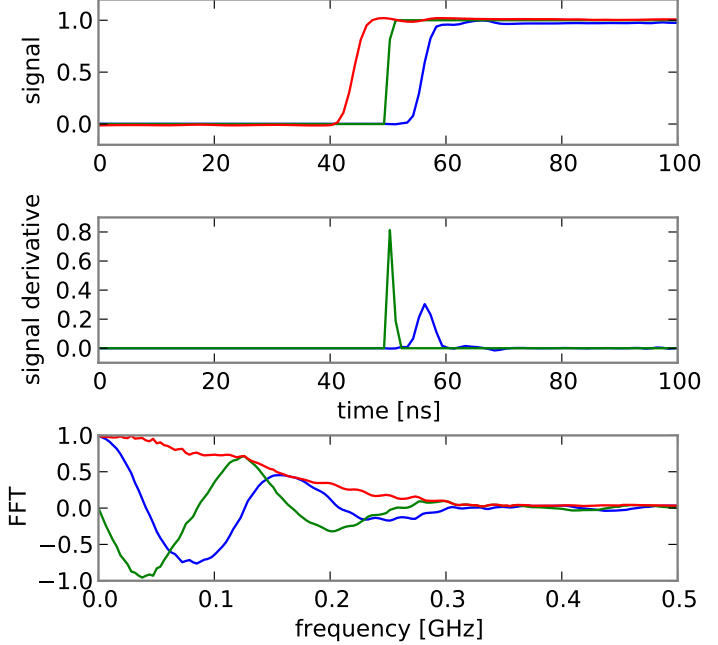


Figure 4.2: (response function filtered with a Gaussian filter with a cut-off at 0.4 GHz)

put and return line – to calculate the response function of the input line. Fig. 4.2 shows the different parts of the response function of the flux line as measured in our experiment. After eliminating the response of the analog-to-digital converter we can calculate the response function between the input port of the flux line and the sample by solving the equation

$$\dots \quad (4.3)$$

4.3.3 Pulse Synchronization

Chapter 5

Measurement Techniques

In this section we will discuss the techniques used to characterize and manipulate our two-qubit processor. All techniques employed are based on ...

5.1 Qubit Readout

5.2 Qubit Manipulation

5.3 Decoherence Time Measurement

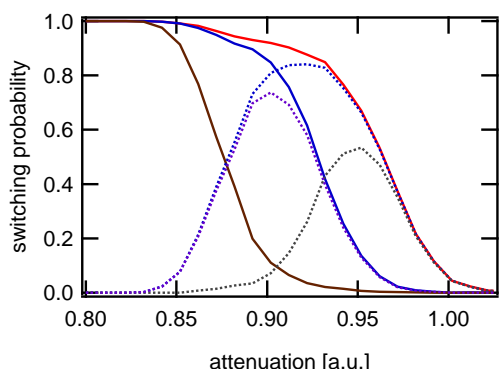


Figure 5.1: Example of a single-qubit s-curve measurement. Shown is the switching probability of the readout for a range of readout drive attenuations, for the different qubit states $|0\rangle$, $|1\rangle$ and $|2\rangle$. The difference in switching probability between individual curves defines the readout contrast between the corresponding qubit states at a given readout power attenuation.

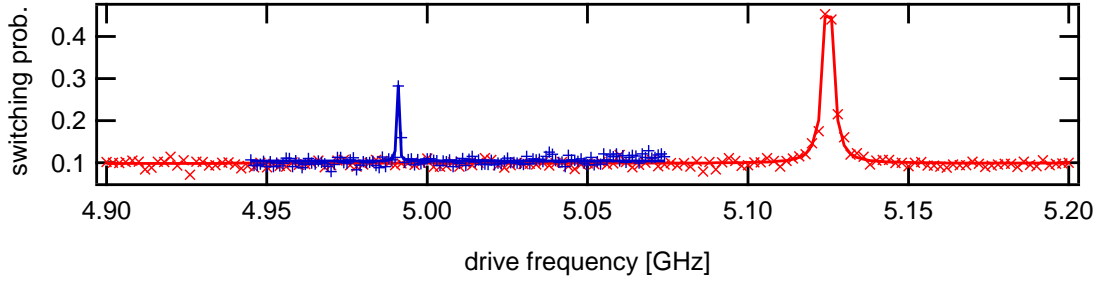


Figure 5.2: Example of a measured qubit spectroscopy. Shown is the switching probability of the qubit readout when driving the qubit with a very long drive pulse (typically $1 \mu\text{s}$) at a given drive frequency. The resonance to the right corresponds to the $|0\rangle \rightarrow |1\rangle$ (at frequency f_{01}) transition of the qubit, the resonance on the left to the 2-photon $|0\rangle \rightarrow |2\rangle$ (at frequency $f_{02}/2$) transition. We perform a Lorentzian fit of the two resonances to obtain the $|0\rangle \rightarrow |1\rangle$ and $|0\rangle \rightarrow |2\rangle/2$ resonance frequencies, from which we can calculate all other qubit transition frequencies.

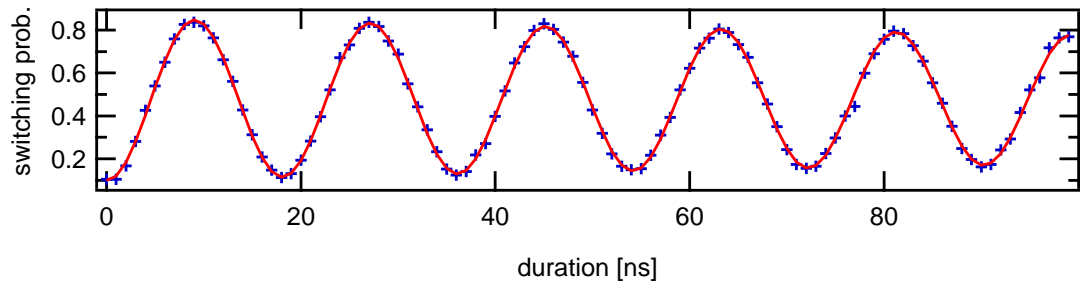


Figure 5.3: Example of a measured qubit Rabi experiment. Shown is the switching probability of the qubit readout when driving the qubit at f_{01} with a Gaussian drive pulse of varying duration. The measurement results are not corrected for readout errors.

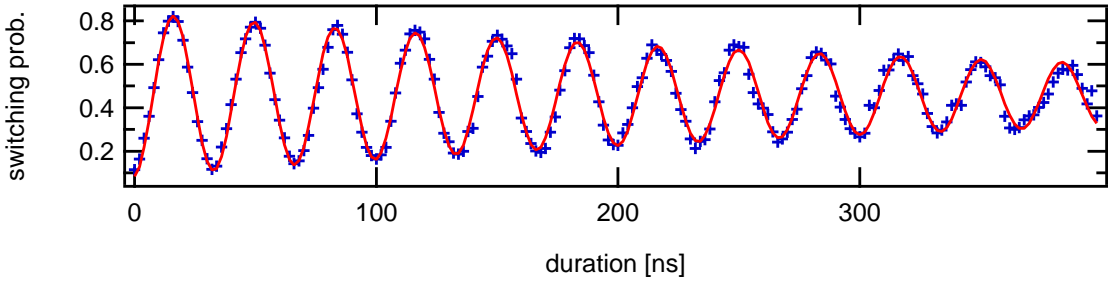


Figure 5.4: Example of a measured qubit Ramsey experiment. Shown is the switching probability of the qubit readout after performing a $X_{\pi/2}$ -wait- $X_{\pi/2}$ drive sequence at a frequency $f_{01} - \delta f$. Fitting the resulting curve with an attenuated sine-wave model allows us to determine the f_{01} frequency of the Qubit with high accuracy.

Chapter 6

Characterizing the Two-Qubit Processor

This section discusses the detailed characterization of individual circuit parts that will be used later to realize two-qubit gate and to run a quantum algorithm on the processor. The discussion will focus on the readout and microwave manipulation of the qubits as well as on the reconstruction of quantum states from measurement data, which will be used later for characterizing gate and processor operation.

6.1 Qubit & Readout Characterization

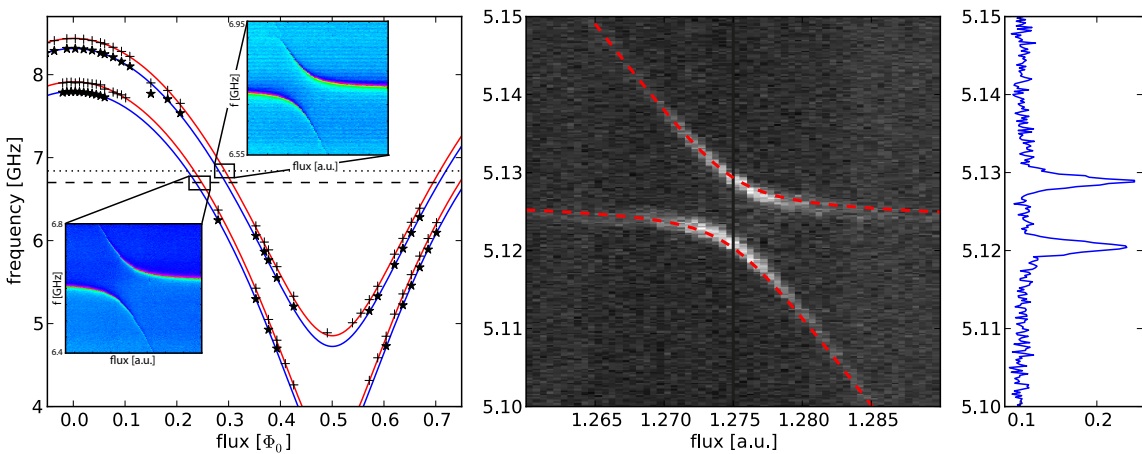


Figure 6.1: Spectroscopy of the realized two-qubit processor. a) $|0\rangle \rightarrow |1\rangle$ and $(|0\rangle \rightarrow |2\rangle)/2$ transition frequencies of the two qubits with fitted dependence and cavity frequencies. b) Avoided level crossing of the $|01\rangle$ and $|10\rangle$ levels of the qubits with fit, $g = 8.7$ MHz. c) Spectroscopy of qubit 1 at the point indicated in b).

The following section discusses the parameters of our two-qubit processor that have

been obtained by various measurements.

6.1.1 Qubit Parameters

To obtain all the relevant parameters of our two-qubit processor, we perform a set of measurements from which we obtain the qubit frequencies, anharmonicities, junction asymmetries, the inter-qubit coupling, the coupling to the microwave drive lines, the coupling of each qubit to its readout and the relaxation and dephasing times of the qubits. The drive and readout couplings as well as the relaxation and dephasing times are measured for a range of qubit frequencies, which will allow us later to pick an ideal working point for our two-qubit experiments. The qubit parameters obtained from spectroscopic measurements are as follows:

- *Qubits*: Spectroscopic measurement of the qubit transitions yielded parameter values of $E_J^I/h = 36.2$ GHz, $E_c^I/h = 0.98$ GHz and $E_J^{II}/h = 43.1$ GHz, $E_C^{II}/h = 0.87$ GHz for the Josephson and charging energies of the two qubits and values of $d^I = 0.2$, $d^{II} = 0.35$ for the qubit junction asymmetries.
- *Readout resonator*: The frequencies of the readout resonators have been measured as $\nu_R^I = 6.84$ GHz and $\nu_R^{II} = 6.70$ GHz with quality factors $Q^I \simeq Q^{II} = 730$, independent measurements of the Kerr nonlinearities yielded $K^I/\nu_R^I \simeq K^{II}/\nu_R^{II} = -2.3 \pm 0.5 \times 10^{-5}$!11! .
- *Qubit-Resonator coupling*: The coupling of the qubits to the readout resonators has been spectroscopically determined as $g_0^I \simeq g_0^{II} = 50$ MHz

To Do 11: add junction inferred parameters from the bare resonator frequencies

Readout Parameters

Qubit Readout, Driving, Relaxation and Dephasing Time

In order to obtain the relaxation time and the coupling of the qubit to the drive line, we perform an automated survey of qubit spectroscopies, qubit readout characterizations and T_1 measurements at different qubit frequencies. The results of such a parameter survey are summarized in fig 6.2, showing the relaxation time T_1 , the readout contrast c_{10} and the Rabi frequency f_{Rabi} for a fixed drive amplitude for the two qubits in a frequency range between 5.2 and 6.5 GHz. As can be seen, the relaxation time of the qubits tends to increase the farther detuned each qubit is from its readout resonator. Not surprisingly, the drive frequency of the qubit also decreases when the qubit-resonator detuning increases as expected from the Purcell effect, which filters incoming microwave signals that are far-detuned from the resonator frequency. The inverse is true for the readout contrast, which increases near-linearly when reducing the qubit-resonator detuning due

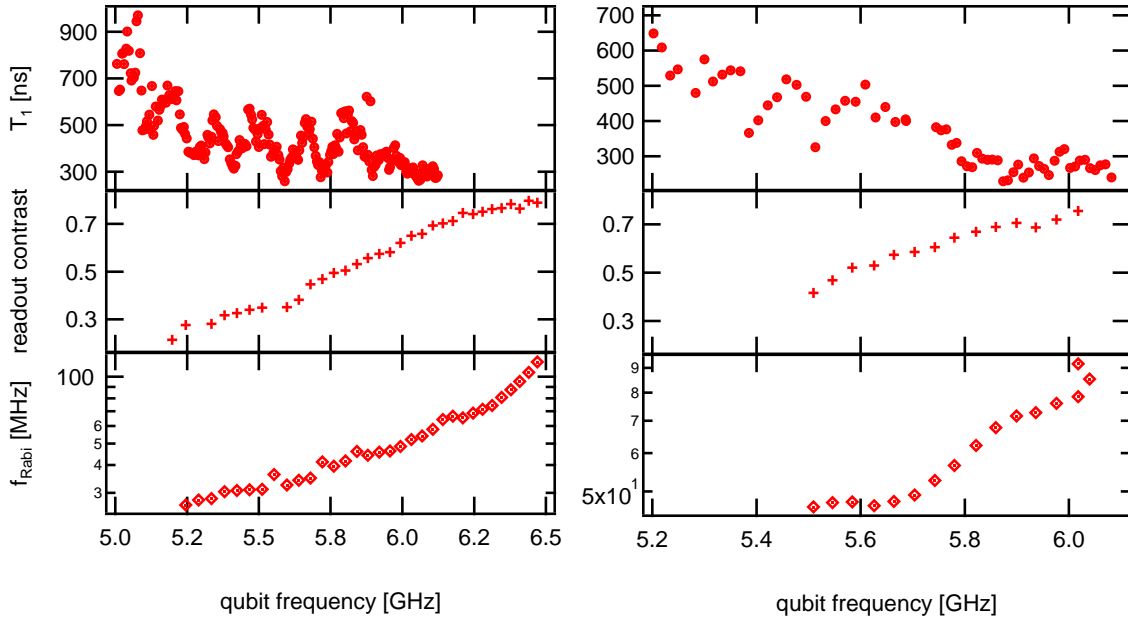


Figure 6.2: A qubit parameter survey showing the relaxation time T_1 , the readout contrast and the Rabi frequency at a fixed drive amplitude for the two qubits over a large range of qubit frequencies.

to the increase of the dispersive resonator frequency shift induced by the qubit that gets stronger the less the qubit is detuned from the readout resonator.

It is interesting to note the non-monotonous characteristic of the qubit relaxation time T_1 shown in fig. 6.2, which cannot be explained by Purcell-filtering through the readout resonator and hints at a different qubit relaxation process present in the system. A possible explanation would be the coupling of the qubit to a spurious low-Q resonance in the environment. Coupling to volumetric resonance modes of the sample holder or non-CPW resonance modes of the readout resonator can be possible explanations for the data. Also, the overall dependency of the relaxation time T_1 on the qubit-resonator detuning –ignoring the “fine-structure” present in the system– is not quadratic as would be expected from the Purcell theory but rather linear. Also, by comparing the qubit relaxation time to the Rabi drive frequency reveals that the increase in T_1 is clearly not proportional to the Purcell factor that determines the qubit relaxation rate through the readout resonator. However, the observed T_1 dependency can be partially explained by taking into account the qubit relaxation through the fast fluxline, which might be strongly-coupled to the qubit on our chip, hence inducing additional qubit relaxation beyond the Purcell and intrinsic qubit relaxation rates. This effect will therefore be studied in more detail in the following sections.

6.2 Single-Qubit Operations

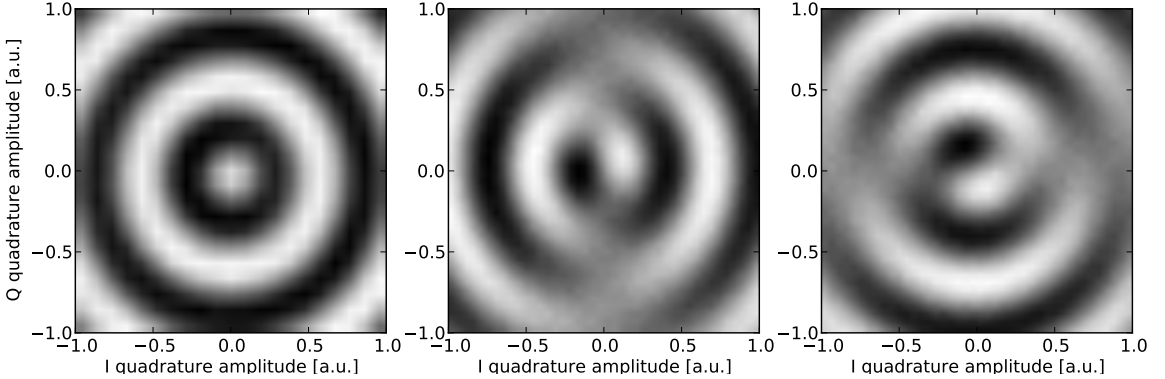


Figure 6.3: Demonstration of single-qubit IQ control. The figures show the state probability of a single qubit when preparing it in one of the states $|1\rangle$, $1/\sqrt{2}(|0\rangle+|1\rangle)$ or $1/\sqrt{2}(|0\rangle+i|1\rangle)$ and subjecting the qubit to a microwave drive pulse of the form $a(t) = V_I \cdot \cos \omega_{rf} t + V_Q \cdot \sin \omega_{rf} t$.

To perform arbitrary single-qubit operations – as needed e.g. for implementing a quantum algorithm or performing quantum state tomography – we need to implement a universal set of X , Y and Z qubit gates with our processor. Qubit rotations in the XY -plane are implemented through microwave drive pulses, where the phase of the drive pulse in reference to an arbitrary reference determines the rotation axis and the amplitude of the drive pulse the Rabi frequency of the gate. To characterize the drive pulses, we perform an experiment where we initialize a single-qubit in the states $|1\rangle$, $1/\sqrt{2}(|0\rangle+|1\rangle)$ and $1/\sqrt{2}(|0\rangle+i|1\rangle)$ and subject it afterwards to a single microwave pulse of the form $a(t) = V_I \cdot \cos \omega_{rf} t + V_Q \cdot \sin \omega_{rf} t$, which we tune by changing the input voltages V_I and V_Q to the IQ -mixer that generates the pulse from a continuous input microwave-tone at frequency ω_{rf} . We measure the qubit state at different values of V_I , V_Q , obtaining the graph shown in fig. 6.3. The qubit which was prepared in state $|1\rangle$ shows a perfectly cylinder-symmetric switching probability pattern when subjecting it to an IQ-pulse of a given phase, which is what one would expect for a qubit being prepared in either the $|0\rangle$ or $|1\rangle$ state. On the contrary, the switching probability distributions of the measured qubits prepared in the states $1/\sqrt{2}(|0\rangle+|1\rangle)$ and $1/\sqrt{2}(|0\rangle+i|1\rangle)$ are mirror-symmetric, where the switching probability does not vary at all along the drive axis which corresponds to the axis along which the qubit has been prepared. These measurements demonstrate therefore our ability to prepare and drive the qubit along arbitrary axes of the Bloch sphere. In the following sections we will analyze more in detail the drive errors inherent to our system and quantitatively analyze different error sources.

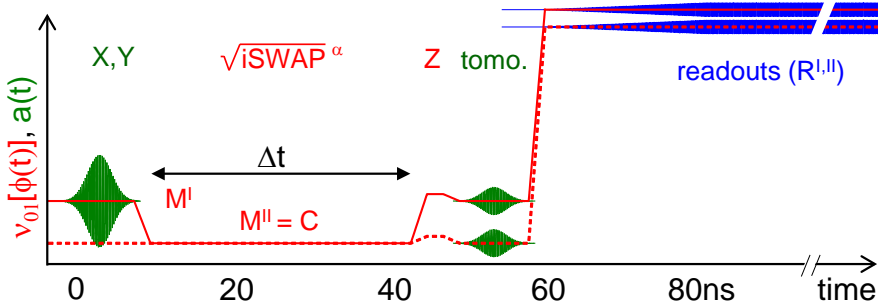


Figure 6.4

6.2.1 Estimation of drive errors

Since the Transmon is a weakly anharmonic multi-level system and thus no real qubit, driving the $|0\rangle \rightarrow |1\rangle$ transition with high power can induce transitions to higher Transmon levels. It is important to estimate and reduce these errors when performing fast qubit gates e.g. for state preparation or tomography. To model the driving of a Transmon, we use the simple drive model in the rotating-frame approximation and as used e.g. in Motzoi et al. (2009):

$$\hat{H} = \begin{pmatrix} 0 & \epsilon^*(t) & 0 \\ \epsilon(t) & \delta & \sqrt{2}\epsilon^*(t) \\ 0 & \sqrt{2}\epsilon(t) & 2\delta + \alpha \end{pmatrix} \quad (6.1)$$

Here, $\epsilon(t) = \epsilon_x(t) + i\epsilon_y(t)$ is the complex drive IQ amplitude in the rotating qubit frame, δ is the detuning of the microwave drive from the Transmon ω_{01} transition frequency and α is the Transmon anharmonicity. To estimate the leakage

6.3 Two Qubit Operations

6.3.1 Creation of Entanglement

6.3.2 Violation of the Bell Inequality

$$CHSH = QS + RS + RT - QT \quad (6.2)$$

with the operators Q, R, S, T being defined as

$$\begin{aligned} Q &= \sigma_z^1 & S &= \sigma_z^2 \cdot \cos \phi + \sigma_x^2 \cdot \sin \phi \\ R &= \sigma_x^1 & T &= -\sigma_z^2 \cdot \sin \phi + \sigma_x^2 \cdot \cos \phi \end{aligned} \quad (6.3)$$

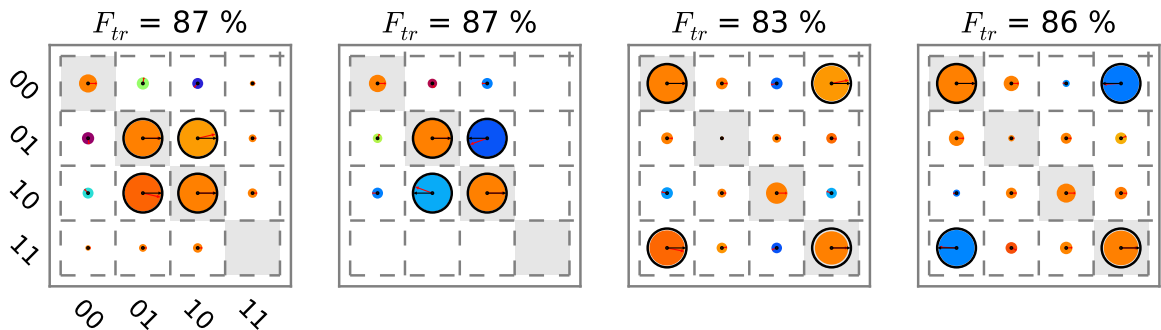


Figure 6.5: Experimentally created $|\psi_+\rangle$ ($F = 0.91$) and $|\psi_-\rangle$ ($F = 0.93$) states

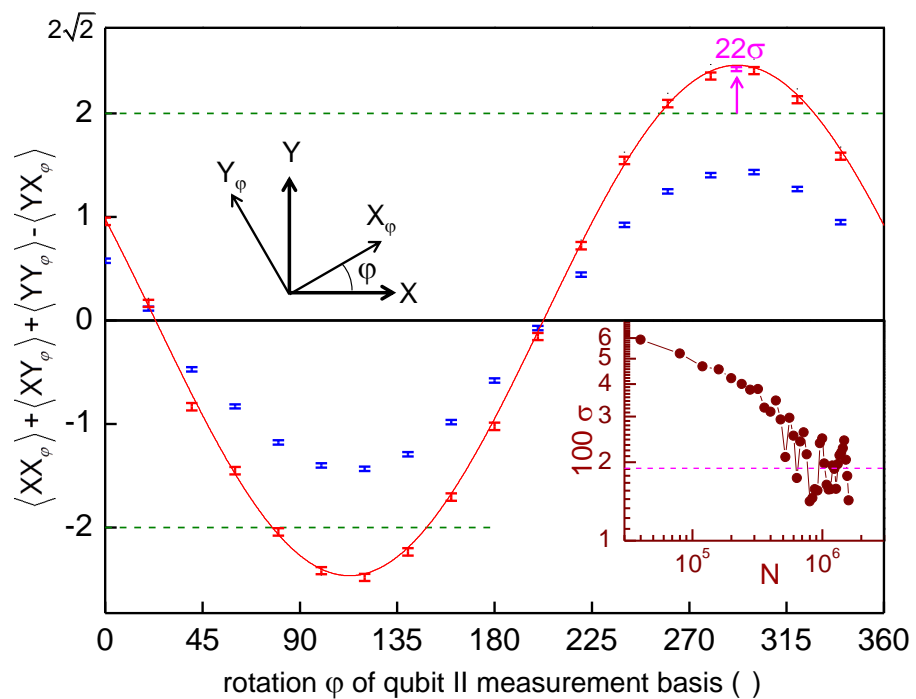


Figure 6.6

Here, the angle ϕ is a parameter that should be chosen in accordance to the phase of the Bell state on which it is applied.

6.3.3 Quantum State Tomography of Two-Qubit States

Quantum state tomography is the procedure of experimentally determining an unknown quantum state(Michael A. Nielsen and Isaac L. Chuang, 2000).

The density matrix of an n-qubit system can be written in general form as

$$\rho = \sum_{v_1, v_2, \dots, v_n} \frac{c_{v_1, v_2, \dots, v_n} \sigma_{v_1} \otimes \sigma_{v_2} \dots \otimes \sigma_{v_n}}{2^n} \quad (6.4)$$

$$c_{v_1, v_2, \dots, v_n} = \text{tr} (\sigma_{v_1} \otimes \sigma_{v_2} \dots \otimes \sigma_{v_n} \rho) \quad (6.5)$$

where $v_i \in \{X, Y, Z, I\}$ and n gives the number of qubits in the system and where the c_{v_1, v_2, \dots, v_n} are real-valued coefficients that fully describe the given density matrix. To reconstruct the density matrix of an experimental quantum system in a well-prepared state it is therefore sufficient to measure the expectation values of these $n^2 - 1$ coefficients on an ensemble of identically prepared systems. However, statistical and systematic measurement errors can yield a set of coefficients that corresponds to a *non-physical* density matrix which violates either the positivity or unity-trace requirement. In the following paragraph we will therefore discuss a technique with which one can estimate the density matrix of a system in a more correct way.

Maximum Likelihood Estimation of Quantum States

A method which is often used in quantum state tomography is the so-called *maximum-likelihood* technique. Rather than directly calculating the density matrix of the system from the obtained expectation values c_{v_1, v_2, \dots, v_n} , it calculates the joint probability of measuring a set $\{c_{X, X, \dots, X}, c_{Y, X, \dots, X}, \dots, c_{I, I, \dots, I}\}$ for a given estimate of the density matrix $\hat{\rho}$. By numerically or analytically maximizing this joint probability over the set of possible density matrices we obtain the density matrix which is most likely to have produced the set of measurement outcomes that we have observed.

The joint measurement operators $\Sigma_j = \sigma_{v_1} \otimes \sigma_{v_2} \dots \otimes \sigma_{v_n}$ have the eigenvalues ± 1 and can thus be written as

$$\sigma_{v_1} \otimes \sigma_{v_2} \dots \otimes \sigma_{v_n} = |+_j\rangle\langle +_j| - |-_j\rangle\langle -_j| \quad (6.6)$$

where $|+_j\rangle$ and $|-_j\rangle$ are the eigenstates corresponding to the eigenvalues ± 1 of Σ_j .

The expectation value $\langle \Sigma_j \rangle$ can be estimated by the quantity

$$\widehat{\langle \Sigma_j \rangle}_\rho = \frac{1}{l} \sum_{i=1}^l M_i(\Sigma_j, \rho) \quad (6.7)$$

where $M_i(M, \rho)$ denotes the outcome of the i -th measurement of the operator M on the state described by the density matrix ρ . This quantity is binomially distributed with the expectation value $E(\widehat{\langle \Sigma_j \rangle}_\rho) = \langle \Sigma_j \rangle_\rho$ and the variance $\sigma^2(\widehat{\langle \Sigma_j \rangle}_\rho) = 1/l \cdot (1 - \langle \Sigma_j \rangle_\rho^2)$. For large sample sizes l , the binomial distribution can be well approximated by a normal distribution with the same expectation value and variance. The joint probability of obtaining a set of measurement values $\{s_1, \dots, s_{n^2-1}\}$ for the set of operators $\{\widehat{\langle \Sigma_1 \rangle}_\rho, \dots, \widehat{\langle \Sigma_{n^2-1} \rangle}_\rho\}$ is then given as

$$P\left(\widehat{\langle \Sigma_1 \rangle}_\rho = s_1; \dots; \widehat{\langle \Sigma_{n^2-1} \rangle}_\rho = s_{n^2-1}\right) = \prod_{i=1}^{n^2-1} \exp\left(-\frac{l}{2} \frac{(s_i - \langle \Sigma_i \rangle_\rho)^2}{1 - \langle \Sigma_i \rangle_\rho^2}\right) \quad (6.8)$$

By maximizing this probability (or the logarithm of it) we obtain an estimate of the density matrix ρ of the quantum state. This technique also allows us to include further optimization parameters when calculating the joint probability. This is useful for modeling e.g. systematic errors of the measurement or preparation process, which can be described by modifying the operators contained in the probability sum. A common source of errors in our tomography measurements are errors in the microwave pulses used to drive the qubit. Since our measurement apparatus permits us only to measure the σ_z operator of each qubit we have to perform $\pi/2$ rotations about the Y or $-X$ axes of the Bloch sphere of each individual qubit in order to measure the values of the σ_x and σ_y operators, which we therefore replace with an effective measurement of each qubits σ_z operator preceded by a rotation R_{ν_i} given as

$$R_X = \exp(-i\sigma_y\pi/4) \quad (6.9)$$

$$R_Y = \exp(+i\sigma_x\pi/4) \quad (6.10)$$

Phase and amplitude errors can be modeled as

$$R_X = \exp(-i[+\sigma_y \cos \alpha + \sigma_x \sin \alpha] [\pi/4 + \gamma]) \quad (6.11)$$

$$R_Y = \exp(+i[-\sigma_y \sin \beta + \sigma_x \cos \beta] [\pi/4 + \delta]) \quad (6.12)$$

Here, α and β represent phase errors whereas γ and δ represent amplitude errors in the drive pulses.

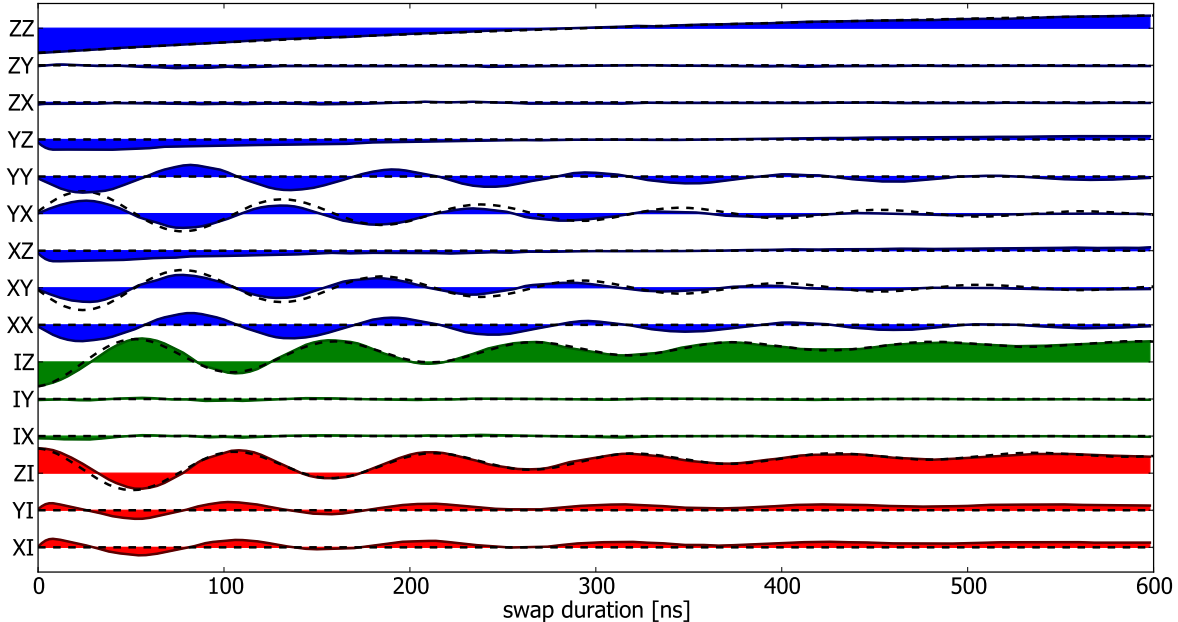


Figure 6.7: Measured Pauli operators $\sigma_i \otimes \sigma_j$ with $i, j \in \{X, Y, Z, I\}$ as a function of the interaction time. Shown are the 6 single-qubit operators as well as the 9 two-qubit correlation operators. The dashed line represents a master-equation simulation of the experiment.

6.4 Realizing a Two-Qubit Gate

6.4.1 Principle

6.4.2 Experimental Implementation

6.4.3 Quantum Process Tomography of the Gate

Introduction & Principle

Implementation

A quantum process can be described as a map $\mathcal{E} : \rho_{\mathcal{H}} \rightarrow \rho_{\mathcal{H}}$ that maps a density matrix ρ defined in a Hilbert space Q_1 to another density matrix $\mathcal{E}(\rho)$ defined in a target Hilbert space Q_2 and fulfilling three axiomatic properties Michael A. Nielsen and Isaac L. Chuang (2000); Haroche and Raimond (2006):

Axiom 6.0.1. $\text{tr} [\mathcal{E}(\rho)]$ is the probability that the process represented by \mathcal{E} occurs, when ρ is the initial state.

Axiom 6.0.2. \mathcal{E} is a *convex-linear map* on the set of density matrices, that is, for probabilities $\{p_i\}$,

$$\mathcal{E} \left(\sum_i p_i \rho_i \right) = \sum_i p_i \mathcal{E}(\rho_i) \quad (6.13)$$

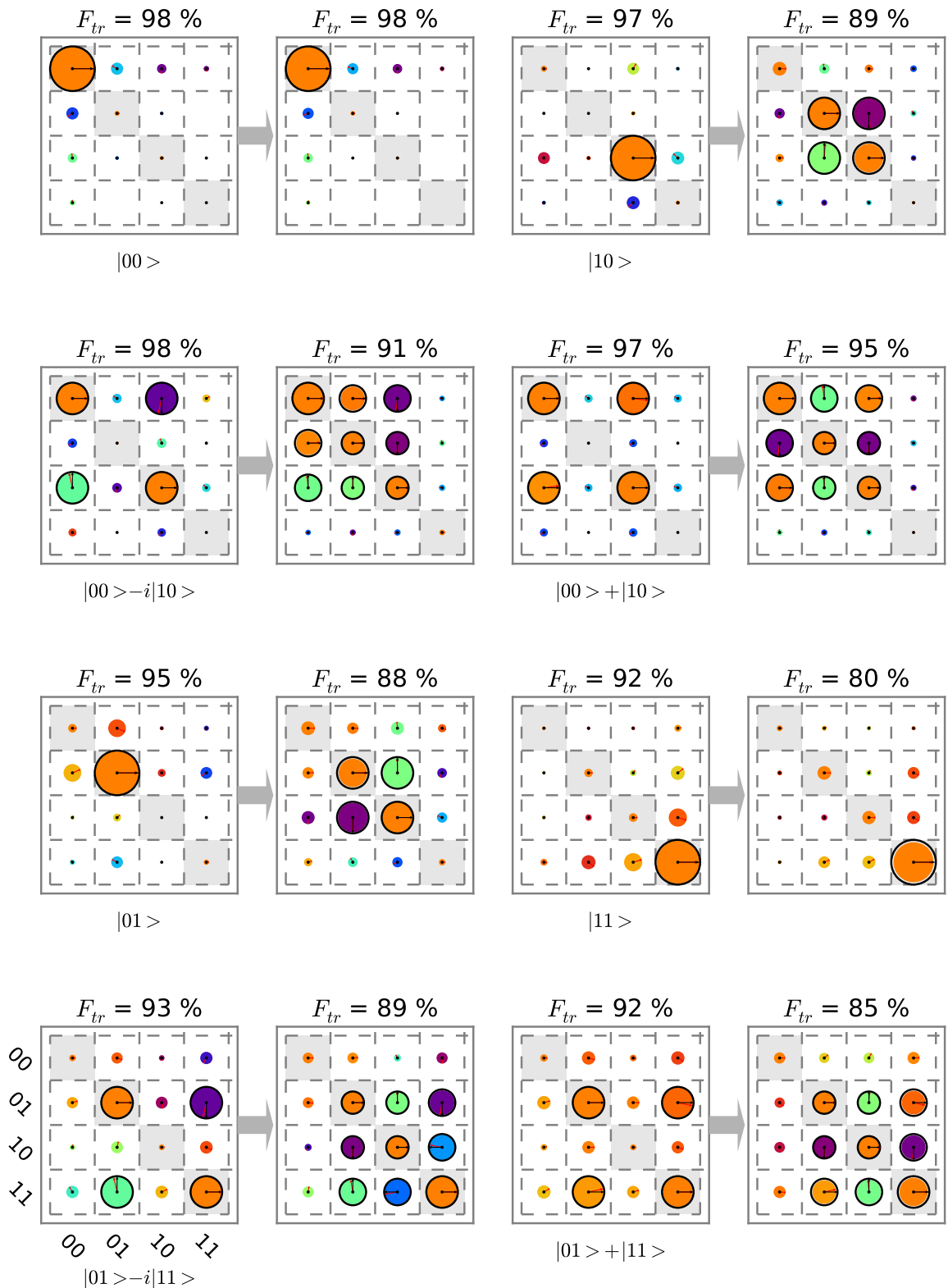


Figure 6.8: The input-output density matrix of the quantum process tomography of the $\sqrt{i\text{SWAP}}$ gate. Shown are the measured density matrices of 16 different input states and the corresponding output matrices with their state fidelities. The ideal matrices are overlaid in red.

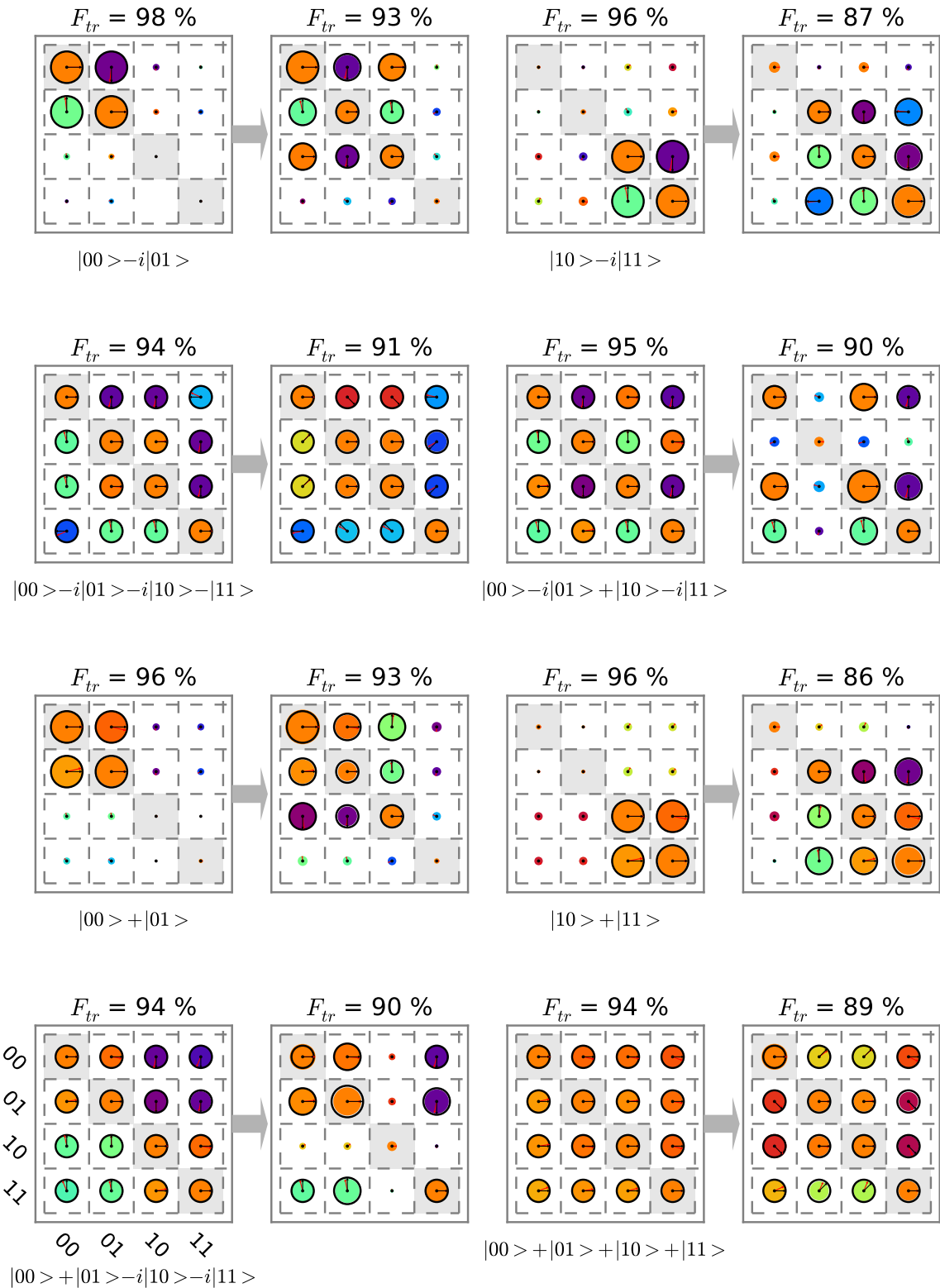


Figure 6.9: The input-output density matrix of the quantum process tomography of the $\sqrt{i\text{SWAP}}$ gate. Shown are the measured density matrices of 16 different input states and the corresponding output matrices with their state fidelities. The ideal matrices are overlaid in red.

Axiom 6.0.3. \mathcal{E} is a *completely-positive* map. That is, if \mathcal{E} maps density operators of system Q_1 to density operators of system Q_2 , then $\mathcal{E}(A)$ must be positive for any positive operator A . Furthermore, if we introduce an extra system R of arbitrary dimensionality, it must be true that $(\mathcal{I} \otimes \mathcal{E})(A)$ is positive for any positive operator A on the combined system RQ_1 , where \mathcal{I} denotes the identity map on system R .

As shown in Michael A. Nielsen and Isaac L. Chuang (2000), any quantum process fulfilling these criteria can be written in the form

$$\mathcal{E}(\rho) = \sum_i E_i \rho E_i^\dagger \quad (6.14)$$

for some set of operators $\{E_i\}$ which map the input Hilbert space to the output Hilbert space, and $\sum_i E_i^\dagger E_i \leq I$.

Now, if we express the operators E_i in a different operator basis \tilde{E}_j such that $E_i = \sum_j a_{ij} \tilde{E}_j$ and insert into eq. (6.14), we obtain

$$\mathcal{E}(\rho) = \sum_i \sum_j a_{ij} \tilde{E}_j \rho \sum_k a_{ik}^* \tilde{E}_k^\dagger \quad (6.15)$$

$$= \sum_{j,k} \tilde{E}_j \rho \tilde{E}_k^\dagger \sum_i a_{ij} a_{ik}^* \quad (6.16)$$

$$= \sum_{j,k} \tilde{E}_j \rho \tilde{E}_k^\dagger \chi_{jk} \quad (6.17)$$

where we defined $\chi_{jk} = \sum_i a_{ij} a_{ik}^*$. This is the so-called χ -matrix representation of the quantum process. Here, all the information on the process is contained in the χ matrix, which controls the action of the process-independent operators \tilde{E}_i on the initial density matrix ρ .

Now, the goal of *quantum process tomography* is to obtain the coefficients of the χ -matrix – or any other complete representation of the process – from a set of experimentally measured density matrices ρ and $\mathcal{E}(\rho)$.

To achieve this, several techniques have been developed. The technique used in this work is the so-called *standard quantum process tomography (SQPT)*. This technique proceeds as follows:

1. Choose a set of operators E_i that forms a full basis of $\mathcal{M} : Q_1 \rightarrow Q_2$. For n-qubit process tomography we usually choose $E_{i_1, i_2, \dots, i_n} = \sigma_{i_1} \otimes \sigma_{i_2} \dots \otimes \sigma_{i_n}$, where σ_i are the single-qubit Pauli operators and $i \in \{I, X, Y, Z\}$.
2. Choose a set of pure quantum states $|\phi_i\rangle$ such that $|\phi_i\rangle \langle \phi_i|$ span the whole space of input density matrices ρ . Usually, for a n-qubit system we choose $\phi =$

$\{|0\rangle, |1\rangle, (|0\rangle + |1\rangle)/\sqrt{2}, (|0\rangle + i|1\rangle)/\sqrt{2}\}^{\otimes n}$, where \otimes^n denotes the n-dimensional Kronecker product of all possible permutations.

3. For each of the $|\phi_i\rangle$, determine $\mathcal{E}(|\phi_i\rangle \langle \phi_i|)$ by quantum state tomography. Usually we also determine $|\phi_i\rangle \langle \phi_i|$ experimentally since the preparation of this state already entails small preparation errors that should be taken into account when performing quantum process tomography.

After having obtained the ρ_i and $\mathcal{E}(\rho_i)$ one obtains the χ -matrix by writing $\mathcal{E}(\rho_i) = \sum_j \lambda_{ij} \tilde{\rho}_j$, with some arbitrary basis $\tilde{\rho}_j$ and letting $\tilde{E}_m \tilde{\rho}_j \tilde{E}_n^\dagger = \sum_k \beta_{jk}^{mn} \tilde{\rho}_k$. We can then insert into eq. (6.17) and obtain

$$\sum_k \lambda_{ik} \tilde{\rho}_k = \sum_{m,n} \chi_{mn} \sum_k \beta_{ik}^{mn} \tilde{\rho}_k \quad (6.18)$$

This directly yields $\lambda_{ik} = \sum_{m,n} \beta_{ik}^{mn} \chi_{mn}$, which, by linear inversion, gives χ .

The Kraus Representation of the Quantum Process

Besides the χ -matrix representation, there is another useful way of expressing a quantum map, the so called *Kraus representation*, which is given as

$$\mathcal{E}(\rho) = \sum_i M_i \rho M_i^\dagger \quad (6.19)$$

It can be shown (Haroche and Raimond, 2006) that this sum contains at most N elements, where N is the dimension of the Hilbert space of the density matrix ρ . We can go from the χ representation to the Kraus representation by changing the basis \tilde{E}_i such that

$$\tilde{E}_i = \sum_l a_{il} \check{E}_l \quad (6.20)$$

which, for eq. (6.17), yields

$$\mathcal{E}(\rho) = \sum_{j,k} \sum_l a_{jl} \check{E}_l \rho \sum_m a_{km}^* \check{E}_m^\dagger \chi_{jk} \quad (6.21)$$

$$= \sum_{l,m} \check{E}_l \rho \check{E}_m^\dagger \sum_{j,k} a_{jl} a_{km}^* \chi_{jk} \quad (6.22)$$

The last sum on the right side of eq. (6.22) corresponds to a change of coordinates of the matrix χ . Now, we can pick the a such that χ is diagonal in the new basis \check{E} and obtain

$$\mathcal{E}(\rho) = \sum_l \lambda_l \check{E}_l \rho \check{E}_l^\dagger \quad (6.23)$$

$$= \sum_l M_l \rho M_l^\dagger \quad (6.24)$$

with λ_l being the l -th eigenvalue of the χ matrix with the eigen-operator \check{E}_l and $M_l = \sqrt{\lambda_l} \check{E}_l$.

6.4.4 Gate Fidelity

6.4.5 Gate Error Analysis

Tomographic errors are removed from the process map of our \sqrt{iSWAP} gate using the following method. The measured Pauli sets corresponding to the sixteen input states are first fitted by a model including errors both in the preparation of the state (index *prep*) and in the tomographic pulses (index *tomo*). The errors included are angular errors $\varepsilon_{I,II}^{\text{prep}}$ on the nominal π rotations around $X_{I,II}$, $\eta_{I,II}^{\text{prep,tomo}}$ and $\delta_{I,II}^{\text{prep,tomo}}$ on the nominal $\pi/2$ rotations around $X_{I,II}$ and $Y_{I,II}$, a possible departure $\xi_{I,II}$ from orthogonality of (\vec{X}_I, \vec{Y}_I) and $(\vec{X}_{II}, \vec{Y}_{II})$, and a possible rotation $\mu_{I,II}$ of the tomographic XY frame with respect to the preparation one. The rotation operators used for preparing the states and doing their tomography are thus given by

$$\begin{aligned} X_{I,II}^{\text{prep}}(\pi) &= e^{-i(\pi+\varepsilon_{I,II}^{\text{prep}})\sigma_x^{I,II}/2}, \\ X_{I,II}^{\text{prep}}(-\pi/2) &= e^{+i(\pi/2+\eta_{I,II}^{\text{prep}})\sigma_x^{I,II}/2}, \\ Y_{I,II}^{\text{prep}}(\pi/2) &= e^{-i(\pi/2+\delta_{I,II}^{\text{prep}})[\cos(\xi_{I,II})\sigma_y^{I,II}-\sin(\xi_{I,II})\sigma_x^{I,II}]/2}, \\ X_{I,II}^{\text{tomo}}(\pi/2) &= e^{-i(\pi/2+\eta_{I,II}^{\text{tomo}})[\sin(\mu_{I,II})\sigma_x^{I,II}+\cos(\mu_{I,II})\sigma_y^{I,II}]/2}, \\ Y_{I,II}^{\text{tomo}}(-\pi/2) &= e^{+i(\pi/2+\delta_{I,II}^{\text{tomo}})[\cos(\mu_{I,II}+\xi_{I,II})\sigma_y^{I,II}-\sin(\mu_{I,II}+\xi_{I,II})\sigma_x^{I,II}]/2}. \end{aligned}$$

The sixteen input states are then $\{\rho_{\text{in}}^e = U |0\rangle\langle 0| U^\dagger\}$ with $\{U\} = \{I_I, X_I^{\text{prep}}(\pi), Y_I^{\text{prep}}(\pi/2), X_I^{\text{prep}}(-\pi/2), X_{II}^{\text{prep}}(\pi), Y_{II}^{\text{prep}}(\pi/2), X_{II}^{\text{prep}}(-\pi/2)\}$, and each input state yields a Pauli set $\{\langle P_k^e \rangle = \text{Tr}(\rho_{\text{in}}^e P_k^e)\}$ with $\{P_k^e\} = \{I_I, X_I^e, Y_I^e, Z_I\} \otimes \{I_{II}, X_{II}^e, Y_{II}^e, Z_{II}\}$, $X^e = Y^{\text{tomo}}(-\pi/2)^\dagger \sigma_z Y^{\text{tomo}}(-\pi/2)$, and $Y^e = X^{\text{tomo}}(\pi/2)^\dagger \sigma_z X^{\text{tomo}}(\pi/2)$. Figure S5.1 shows the best fit of the modelled $\{\langle P_k^e \rangle\}$ set to the measured input Pauli sets, yielding $\varepsilon_I^{\text{prep}} = -1^\circ$, $\varepsilon_{II}^{\text{prep}} = -3^\circ$, $\eta_I^{\text{prep}} = 3^\circ$, $\eta_{II}^{\text{prep}} = 4^\circ$, $\delta_I^{\text{prep}} = -6^\circ$, $\delta_{II}^{\text{prep}} = -3^\circ$, $\eta_I^{\text{tomo}} = -6^\circ$, $\eta_{II}^{\text{tomo}} = -4^\circ$, $\lambda_I^{\text{tomo}} = 12^\circ$, $\lambda_{II}^{\text{tomo}} = 5^\circ$, $\xi_I = 1^\circ$, $\xi_{II} = -2^\circ$, and $\mu_I = \mu_{II} = -11^\circ$.

Knowing the tomographic errors and thus $\{\langle P_k^e \rangle\}$, we then invert the linear relation $\{\langle P_k^e \rangle = \text{Tr}(\rho P_k^e)\}$ to find the 16×16 matrix B that links the vector $\overrightarrow{\langle P_k^e \rangle}$ to the columnized density matrix $\overrightarrow{\rho}$, i.e. $\overrightarrow{\rho} = B \cdot \overrightarrow{\langle P_k^e \rangle}$. The matrix B is finally applied to the measured

sixteen input and sixteen output Pauli sets to find the sixteen $(\rho_{in}, \rho_{out})_k$ couples to be used for calculating the gate map.

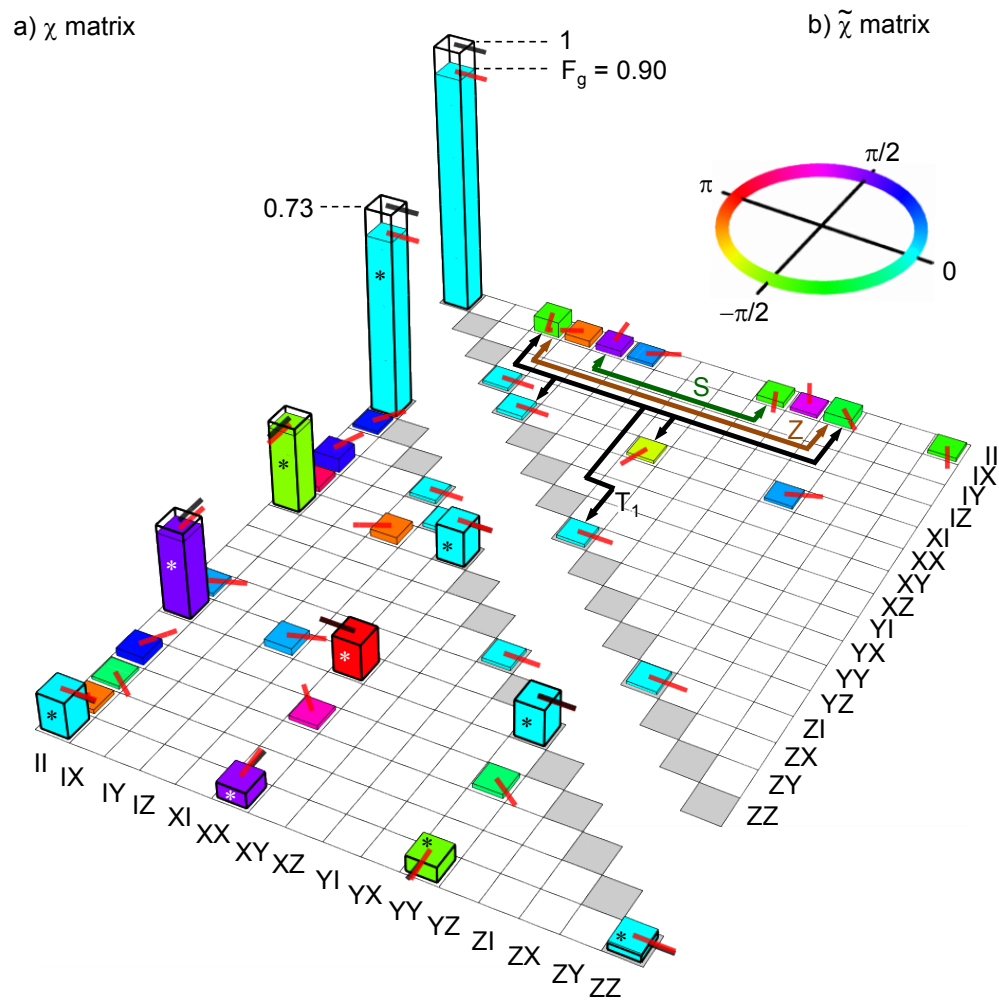


Figure 6.10

Chapter 7

Running the Grover Search Algorithm

This chapter will describe the experimental implementation of the so-called *Grover search algorithm* with our two-qubit quantum processor. The first section will provide a short introduction of the algorithm and motivate the interest in realizing it. The following sections will then discuss the details of the experimental realization of this algorithm. We will discuss the results that we obtained and compare the algorithm fidelity and runtime to that of an equivalent, classical algorithm. Finally, we will analyze all relevant errors made in our experiment.

7.1 Introduction & Motivation

Search algorithms are of great importance in many domains of mathematics and computer science. One such search problem that often arises and which will be discussed in the following sections can be formulated in simple terms as follows:

Theorem 7.1. Assume that we have a search space \mathcal{S} that consists of a finite number N of states $s \in \mathcal{S}$. The solution to our search problem corresponds to a subset of M states of the search space $\mathcal{T} \subset \mathcal{S}$. We can then define a search function $\mathcal{C}(s) : \mathcal{S} \rightarrow \{0, 1\}$ that discriminates between states that solve the search problem and states that don't, such that $\mathcal{C}(s) = 1$ for $s \in \mathcal{T}$ and $\mathcal{C}(s) = 0$ otherwise.

Using this definition of the search problem, the goal of a search algorithm is to find all states $t \in \mathcal{S}$ for which $\mathcal{C}(t) = 1$. In the following sections, for the sake of simplicity we will assume in the following sections that the solution set \mathcal{T} contains only one single state t . This special case can easily be generalized to cases where more than one solution exists to the search problem.

The first step in order to solve a search problem of the kind described above is to map the problem above to a form suitable for solution by a digital (quantum) computer. For this, we first number and encode the N input states $s_i \in \mathcal{S}$ in binary form such that

$s_i = \sum_{j=0}^l s_{ij} 2^j$, where l is the minimum required length of a binary register that can hold all N input states. With this definition, it is then also trivial to reformulate \mathcal{C} such that the function operates on a binary input register instead of the original input states.

Using these assumptions and definitions, it can then be shown that the most efficient classical search algorithm for solving the search problem above will use $\mathcal{O}(N)$ calls of the function \mathcal{C} to find the solution t of the search problem. Assuming that the time to evaluate the function \mathcal{C} is far superior to the time needed to perform any other operation during the search algorithm, the number of calls to \mathcal{C} also corresponds approximately to the runtime of the whole search algorithm.

Amazingly, in 1997, Lev Grover found a quantum algorithm that could solve exactly the same search problem with only $\mathcal{O}(\sqrt{N})$ calls to the function \mathcal{C} (Grover, 1997). His algorithm achieves this by repeatedly calling a quantum-mechanical implementation of the function \mathcal{C} with a highly superposed qubit state and applying a special operator to the output state afterwards. The individual steps of the algorithm are straightforward and are given as follows:

1. Initialize a qubit register to the state $|\psi\rangle = |0\rangle$ (corresponding to a binary input state $|0000\dots 0_B\rangle$)
2. Apply the generalized Hadamard operation to the qubit register, producing a fully superposed quantum state

$$|\psi\rangle = \frac{1}{\sqrt{N}} \sum_{i=0}^{N-1} |i\rangle$$

3. Repeat the following sequence $\mathcal{O}(\sqrt{N})$ times:
 - a) Apply the *Oracle operator* $|i\rangle \rightarrow (-1)^{\mathcal{C}(i)} |i\rangle$ to the state $|\psi\rangle$
 - b) Apply the *diffusion operator* $|i\rangle \rightarrow -|i\rangle + \frac{2}{N} \sum_{j=0}^{N-1} |j\rangle$ to the state $|\psi\rangle$
4. Measure the state of the quantum register

Here, we have enumerated the states of the qubit register from $|0\rangle$ to $|N-1\rangle$. Basically, the Grover algorithm makes use of quantum parallelism to solve the search problem $\mathcal{O}(\sqrt{N})$ times faster than the most efficient classical algorithm. To understand better its strategy used to solve the search problem, the different steps of the algorithm can be rephrased in the following, more intuitive way:

- First, it creates a fully superposed quantum state which contains all possible solutions to the search problem at once. The amplitudes and phases of each individual state are all equal in the beginning.

- Then, it applies the so-called Oracle operator to this superposed state. The effect of the Oracle is to turn the phase of the states t for which $\mathcal{C}(t) = 1$ by an angle π . As will be shown later, such an Oracle operator can be implemented in a straightforward way for any classical search function.
- In the next step, it applies a diffusion operator to the quantum state which transfers a fraction of the amplitude from states with zero phase to the turned states, increasing thus the amplitude of the latter. In this process, the phases of all states also get turned back to zero, allowing the algorithm to repeat the sequence above.
- Repeating these two operations increases the amplitude of the states that correspond to a solution of the search problem until the amplitudes of all the other states are zero. After that point, the process reverses and the amplitude is transferred back to the original states. It is therefore crucial to stop the repetition sequence given above after the right number of iterations.

By implementing the search function as a quantum operator, the Grover algorithm is able to evaluate it in one single call for all possible input states. This so-called *quantum parallelism* provides the basis for the speed-up of the search in comparison to a classical algorithm. However, being able to encode the result of the search function in the phase of a multi-qubit state does not directly translate to a speed advantage since it is usually very hard to extract this phase information from the quantum state. Indeed, to extract the values of all phases from an N -qubit state, it is necessary to perform $\mathcal{O}(2^N)$ measurements on an ensemble of identically prepared quantum states. However, extracting the state amplitudes from such a state takes only $\mathcal{O}(N)$ measurements, which in addition can usually be carried out in parallel. It is for this that the Grover algorithm uses an operator that transforms the information encoded in the phases of the qubits to an information encoded in their amplitude. However, since the conversion between phase to amplitude information through the application of an unitary operator is limited by certain physical constraints, the algorithm needs to repeat the encode-and-transfer sequence described above $\mathcal{O}(\sqrt{N})$ times.

To analyze further the constraints and principles of the algorithm, we will discuss a more detailed derivation of it starting from the Schrödinger equation and we will also explain what limits the efficiency of the phase-to-amplitude conversion in the algorithm.

7.1.1 Deriving the Grover Algorithm from Schrödinger's Equation

An interesting derivation of the Grover algorithm algorithm starting from Schrödinger's equation has been detailed by Grover himself in a seminal paper (Grover, 2001) and shall be briefly rediscussed here since it sheds light on the basic principles on which the

algorithm is based. The derivation begins by considering a quantum system governed by Schrödinger's equation, which can be written as (omitting all physical constants)

$$-i\frac{\delta}{\delta t}\psi(x, t) = \frac{\delta^2}{\delta x^2}\psi(x, t) - V(x)\psi(x, t) \quad (7.1)$$

Here $\psi(x, t)$ describes the wave-function and V is a time-independent potential. Let us assume that the potential $V(x)$ is shaped as in fig. 7.1, i.e. possessing a local minimum of energy. When one initializes the system to a state $\psi_0(x, t_0)$ and lets it evolve for a given time, $\psi(x, t)$ will be attracted by the minimum of potential energy and “fall into it” much like a classical particle in such a potential would¹. One might thus ask if one could encode the solution to a search problem as a point of minimum energy x_0 of a potential $V(x)$, take an initial state $\psi_0(x, t_0)$ and let it evolve into a state that has a high probability around x_0 , thereby solving the search problem. To answer this question it is first necessary to discretize the wavefunction $\psi(x, t)$ such that it can represent the search problem stated in the last chapter, which is defined over a finite number of states. In the most simple case, we can use a regular grid of points x_i with a spacing dx for this, as shown in fig. 7.1b. Discretizing the time evolution of eq. 7.1 in steps dt as well and defining $\epsilon = dt/dx^2$, we obtain a new equation of the form

$$-\frac{\psi_i^{t+dt} - \psi_i^t}{dt} = \frac{\psi_{i+1}^t + \psi_{i-1}^t - 2\psi_i^t}{dx^2} - V(x_i)\psi_i^t \quad (7.2)$$

where we have written $\psi(x_i, t) = \psi_i^t$. For a circular grid with N points we can write this equation in matrix form as

$$\vec{\psi}^{t+dt} = S^t \cdot \vec{\psi}^t \quad (7.3)$$

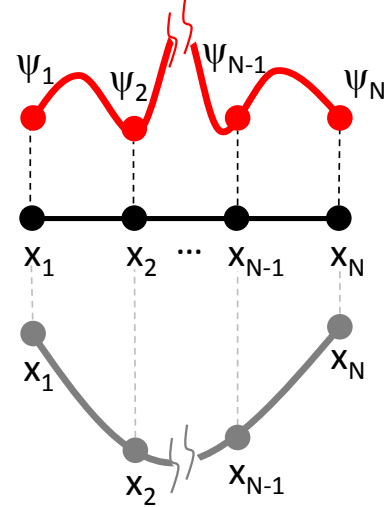


Figure 7.1: A wavefunction $\psi(x)$ and potential $V(x)$ defined on a grid of points x_1, \dots, x_N .

¹of course, since there is no dissipation, the state will not come to rest at the minimum point of energy but rather oscillate around it conserving its total potential and kinetic energy

with S being a state transition matrix of the form

$$S = \begin{pmatrix} 1 - 2i\epsilon - iV(x_1)dt & i\epsilon & 0 & \dots & i\epsilon \\ i\epsilon & 1 - 2i\epsilon - iV(x_2)dt & i\epsilon & \dots & 0 \\ 0 & i\epsilon & \ddots & & \vdots \\ \vdots & & \ddots & & \vdots \\ i\epsilon & 0 & \dots & i\epsilon & 1 - 2i\epsilon - iV(x_N)dt \end{pmatrix} \quad (7.4)$$

For infinitesimal times dt we can separate the effect of the potential $V(x)$ on the wavefunction from the spatial dispersion by writing $S \approx D \cdot R$ with

$$D = \begin{pmatrix} 1 - 2i\epsilon & i\epsilon & 0 & 0 & \dots & i\epsilon \\ i\epsilon & 1 - 2i\epsilon & i\epsilon & 0 & \dots & 0 \\ \dots & \ddots & & & & \vdots \\ i\epsilon & 0 & 0 & \dots & i\epsilon & 1 - 2i\epsilon \end{pmatrix} \quad (7.5)$$

and

$$R = \begin{pmatrix} e^{-iV(x_1)dt} & 0 & \dots & 0 \\ 0 & e^{-iV(x_2)dt} & \dots & 0 \\ 0 & \dots & 0 & e^{-iV(x_N)dt} \end{pmatrix} \quad (7.6)$$

This approximation is correct to $\mathcal{O}(\epsilon)$ up to an unimportant renormalization factor. We can now repeatedly apply the matrix product $D \cdot R$ to the wavefunction to obtain its state after a given finite time Δt by writing

$$\vec{\psi}^{t+\Delta t} = \left(\prod_{i=1}^{\Delta t/dt} D \cdot R \right) \cdot \vec{\psi}^t \quad (7.7)$$

This technique of splitting up the full evolution operator into a product of two or more non-commuting operators that are applied repeatedly to the wavefunction to obtain its state after a finite time is sometimes referred to as *Trotterification* – in reference to the so-called *Lie-Trotter formula* on which it is based – and is widely used in digital quantum simulation (Lloyd, 1996; Lanyon et al., 2011).

As can be seen in eq. (7.7), the evolution of the wavefunction at infinitesimal times is governed by two processes: The interaction with the potential V and a spatial dispersion process that mixes different spatial parts of the wavefunction with each other. The operator D resembles a Markov diffusion process since each row and column of the matrix sums up to unity, whereas R changes the phase of each element of the wavefunction in accordance with the local potential seen by it. If we apply R to a fully superposed

initial state of the form $\psi_i = 1$ (omitting the normalization factor for clarity) and assume that $V_i = 0$ for $i \neq j$ and $V_j dt = \pi/2$ (the potential thus encoding a search function with $C(j) = 1$ and $C(i) = 0$ for $i \neq j$), the element ψ_j will get turned according to $\psi_j \rightarrow i\psi_j$, whereas all other elements ψ_i will remain unchanged. Applying the operator D to the resulting state will transform ψ_j according to $\psi_j \rightarrow \psi_j(i + 2\epsilon(1 + i))$ with a corresponding amplitude $\sqrt{1 + 4\epsilon + \mathcal{O}(\epsilon^2)}$ and the adjacent states $\psi_{j\pm 1}$ according to $\psi_{j\pm 1} \rightarrow \psi_{j\pm 1}(1 - \epsilon(1 + i))$ with an amplitude $\sqrt{1 - 2\epsilon + \mathcal{O}(\epsilon^2)}$. Hence there is a transfer of amplitude between the state whose phase has been turned and its neighboring states. If we reset the phases of all the ψ_i to zero afterwards, we can iterate the application of $D \cdot R$ until all of the amplitude has been transferred to the element ψ_j that solves the search problem. This is, in essence, exactly what the Grover algorithm does, the only difference being that it replaces the matrix D with an unitary matrix that maximizes the amplitude transfer to the states solving the search problem, thereby speeding up the algorithm. As stated before, the efficiency with which the algorithm can transfer amplitude between different states is limited by physical constraints, in the next section we will therefore discuss exactly what limits this efficiency and which unitary matrix one should choose to maximize it.

Efficiency of Quantum ‘‘Crawling’’

It is interesting to ask which is the maximum amount of amplitude that can be transferred in a single step of the Grover search algorithm and which form the matrix D should have to maximize this transfer. To answer this question and derive the ideal diffusion matrix, we will assume first that the matrix R which encodes the value of the search function C in the quantum state of the qubit register can be written in the most general case as

$$R = \sum_{i=0}^{N-1} \exp[i\alpha C(i)] |i\rangle \langle i| \quad (7.8)$$

Here, α is a factor which we can choose arbitrarily. So, without loss of generality, we can choose $\alpha = \pi$, yielding an Oracle operator of the form

$$R = I - 2 \sum_{i=0}^{N-1} C(i) |i\rangle \langle i| \quad (7.9)$$

This operator will flip the sign of all states for which $C(i) = 1$. Now, the next step consists in finding a diffusion or state transfer matrix which will maximize the amplitude transfer to states marked by the Oracle operator above and which will also reset the phases of the quantum register to zero afterwards, such that we might apply the Oracle operator to the resulting state again. In the most general case, such a state transfer matrix will

have the form

$$D_c = \begin{pmatrix} b & a & a & \dots & a \\ a & b & a & \dots & a \\ \vdots & \ddots & & & \vdots \\ a & \dots & a & b \end{pmatrix} \quad (7.10)$$

Here, we assume that all non-diagonal elements of the matrix are equal, which is well justified since we have no knowledge of the structure of the search space of the problem and therefore want to treat all basis states equally during the phase-to-amplitude conversion. Furthermore, since both the initial quantum state and the Oracle operator as given by eq. (7.9) contain only real numbers and we demand that the quantum state after applying D_c may contain only positive real numbers it is easy to show that a, b must be real numbers. Finally, the unitarity of quantum operators demands that $D_c^\dagger D_c = I$, which for the matrix above is equivalent to the two conditions

$$1 = b^2 + (N - 1)a^2 \quad (7.11)$$

$$0 = 2ab + (N - 2)a^2 \quad (7.12)$$

Solving these two equations for a, b yields the trivial solution $b = \pm 1, a = 0$ and the more interesting one $b = \pm(1 - 2/N), a = \mp 2/N$. As can be checked easily, the solution $b = 1 - 2/N, a = 2/N$ results in a maximum amplitude transfer from states $|i\rangle$ for which $\mathcal{C}(i) = 0$ to states $|j\rangle$ for which $\mathcal{C}(j) = 1$. Thus the ideal diffusion matrix to be used in the Grover algorithm is given as

$$D = \begin{pmatrix} -1 + 2/N & 2/N & 2/N & \dots & 2/N \\ 2/N & -1 + 2/N & 2/N & \dots & 2/N \\ \vdots & & \ddots & & \vdots \\ 2/N & 2/N & 2/N & \dots & -1 + 2/N \end{pmatrix} \quad (7.13)$$

This matrix, together with an Oracle operator R as given by eq. (7.9) will yield the maximum amplitude transfer from states not solving the search problem to states that solve it. Repeating the application of $D \cdot R$ on an initially fully superposed quantum states for $\mathcal{O}(\sqrt{N})$ times will transform the input state to a state containing only the solutions of the search problem, thus solving the problem quadratically faster than would be possible with any classical algorithm.

To be able to compare the Grover algorithm as outlined here to a classical version solving the same search problem, we will now discuss another variant of the algorithm using an ancilla qubit to encode the result of the search function. This implementation will make it possible to devise a classical algorithm that can then be compared to the quantum algorithm discussed here. In the discussion in following sections we will focus

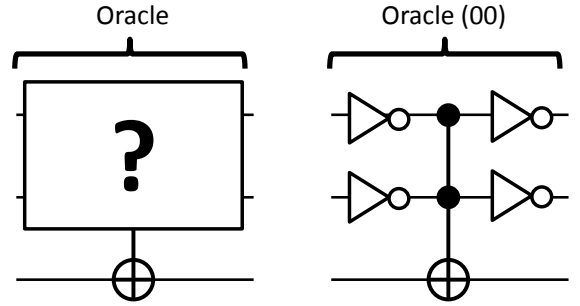


Figure 7.2: a) Ancilla-based implementation of the Oracle function \mathcal{C} . The state of the third bit get flipped if the search function $\mathcal{C}(i) = 1$ for the given input state i . b) An example of an ancilla-based search function that returns a true value for the input state 00.

entirely on the two-qubit case, which is the case most relevant to this work.

7.1.2 Ancilla-based Implementation of the Algorithm

The implementation of the Grover search algorithm outlined above encodes the value of the search function \mathcal{C} in the phase of the input state supplied to this function. This makes it hard to compare the algorithm to a classical search algorithm which operates on a binary input states and, in general, cannot encode the result of the search function directly in the input state. It is therefore useful to formulate a version of the Grover algorithm where the Oracle function does not directly encode the marked state in the input qubit register but rather uses an ancilla qubit to store the result of calling \mathcal{C} . Such a representation of the algorithm is very useful since it can be directly compared to a classical algorithm implemented with reversible logic gates, thus making it possible to benchmark our algorithm against a classical counterpart.

Exemplary implementations of ancilla-based search functions \mathcal{C} implemented using reversible (quantum) gates are shown in fig. 7.2 for the two-qubit case. There, a two-qubit Toffoli gate in combination with several single-qubit NOT gates (that can be easily implemented as single-qubit X_π rotations) is used to flip the state of an ancilla-qubit conditionally on the input state of the gate. Using this approach, any arbitrary classical search function \mathcal{C} that can be implemented with a set of universal reversible logic gates (e.g. the Toffoli gate and the NOT gate) can be directly mapped to a corresponding quantum operator that works on quantum-mechanical input states and implements the classical search function.

Now, to use the Grover algorithm with such an ancilla-based quantum Oracle, it is necessary to re-encode the result of the Oracle in the qubit input state. Fig. 7.3 shows a version of the two-qubit Grover algorithm that achieves exactly this by using a three-qubit control-not (CNOT) gate C of the form

$$C = I^{n \otimes n} - 2 \sum_{ij} |ij1\rangle \langle ij1| \quad (7.14)$$

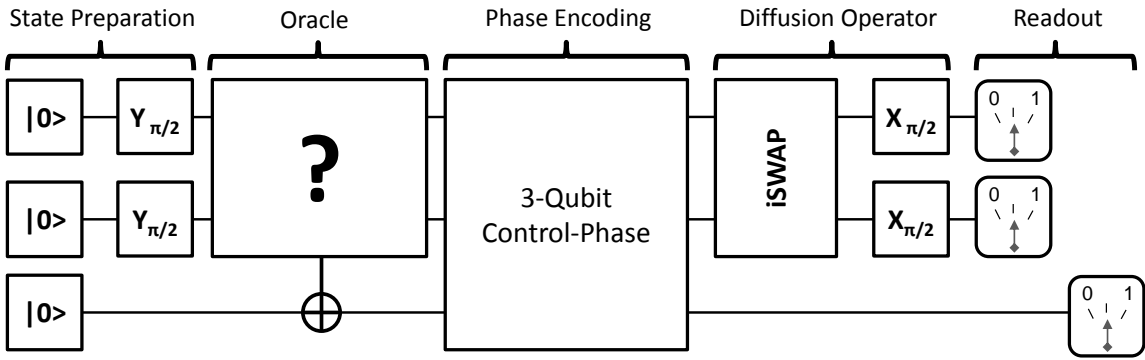


Figure 7.3: A full version of an ancilla-based implementation of the two-qubit Grover search algorithm. The algorithm works on a two-qubit input state and flips the state of a control qubit for one of the four possible input states in accordance to an unknown Oracle function. It then applies a 3-qubit control-phase operation of that maps $|xx1\rangle \rightarrow -|xx1\rangle$, $|xx0\rangle \rightarrow |xx0\rangle$ to encode the state of the control qubit directly in the two input qubits and then uses a diffusion operator to determine the state which has been marked by the Oracle function.

to phase-encoded the state of the ancillary qubit in the state of the input qubit register. After the re-encoding of the result, the ancilla qubit is not needed during the remainder of the algorithm and must not be read out before the algorithm terminates.

7.2 Comparision to a Classical Algorithm

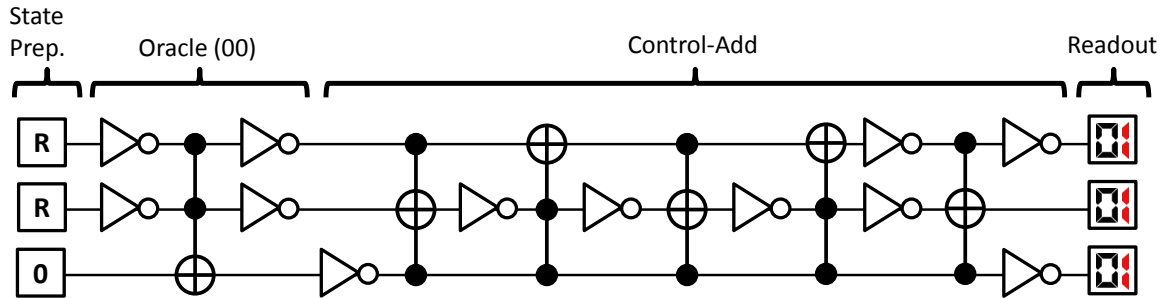


Figure 7.4: Classical reversible implementation of a search algorithm on a two-bit input register. The Oracle function can be implemented by two single-bit NOT operations and a Toffoli gate. R designates the generation of a random binary value at the beginning of the algorithm. If the Oracle does not yield the correct answer, the test state is incremented. The average success probability of the algorithm is 50 %.

In order to quantify the quantum speed-up achieved by a quantum algorithm it is necessary to map the problem it solves to an equivalent problem that can be solved by a classical algorithm. For the Grover algorithm, this is the search problem that we discussed in the first section of this chapter. Now, with the ancilla-based version of the Grover algorithm introduced in the last section it is possible to directly formulate a clas-

sical algorithm that solves the same problem and compare the efficiency of the two. We can use reversible logic gates such as the Toffoli gate and the single-(qu)bit NOT gate to implement the classical algorithm, thereby achieving a maximum comparability with the quantum version. Since the two-qubit Grover algorithm evaluates the search function \mathcal{C} only once it is interesting to ask what would be the performance of an equivalent classical algorithm which calls \mathcal{C} once and returns an estimate of the state solving the search problem. Such an algorithm is shown in fig. 7.4. It achieves a success probability of 50 % by evaluating the function \mathcal{C} for a randomly generated two-bit input value r and returning r if it found $\mathcal{C}(r) = 1$ or $r + 1 \pmod 4$ otherwise. The 50 % success rate of this algorithm provides a benchmark against which we will measure the speed-up of our implementation of the Grover algorithm.

7.3 Experimental Implementation

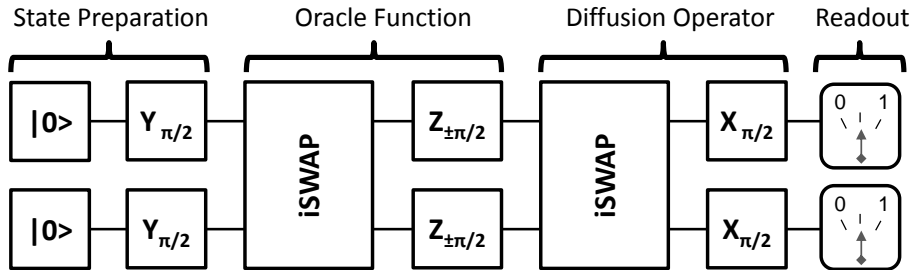


Figure 7.5: Schematic of our implementation of the Grover search algorithm. The algorithm consists in generating a fully superposed input state, applying the Oracle function to it and analyzing the resulting state by applying the Diffusion transform to it and reading out the value of the qubit register afterwards.

In this work we implement a compiled version of the two-qubit Grover algorithm. The gate sequence of the algorithm is shown in fig. 7.5 and consists in two $i\text{SWAP}$ gates and six single-qubit gates applied to an initial state $|00\rangle$. The first $i\text{SWAP}$ gate together with the two single-qubit $Z_{\pm\pi}$ rotations implements the Oracle function $f(x)$ as given in eq. (7.9), where the signs of the rotation operations determines the state which is marked and can be either $|00\rangle$ (corresponding to a $Z_{-\pi/2}^1 \cdot Z_{-\pi/2}^2$ rotation), $|01\rangle$ ($Z_{-\pi/2}^1 \cdot Z_{\pi/2}^2$), $|10\rangle$ ($Z_{\pi/2}^1 \cdot Z_{-\pi/2}^2$) or $|11\rangle$ ($Z_{\pi/2}^1 \cdot Z_{\pi/2}^2$). The second $i\text{SWAP}$ operation together with the following $X_{\pi/2}^1 \cdot X_{\pi/2}^2$ operation implements the diffusion operator as given by eq (7.13). The final step of the algorithm consists in reading out the two-qubit register.

7.3.1 Pulse Sequence

To implement the gate sequence described above we need to realize a sequence of microwave and flux pulses which realize the individual quantum gates of the sequence. To eliminate possible gate errors, we perform a series of calibration measurements before to tune-up the individual single- and two-qubit gates needed for the algorithm. In addition, we run individual parts of the algorithm successively and perform quantum state tomography to characterize the state of the quantum register after each step of the algorithm and correct the gate operations applied to the qubit in order to maximize the fidelity of the measured states in respect to the ideal ones. Fig. 7.6 shows an experimental pulse sequence for the Grover algorithm with an Oracle operator marking the state $|00\rangle$. Shown are the frequencies of the two qubits during the runtime of the algorithm and the microwave drive and readout pulses applied to them.

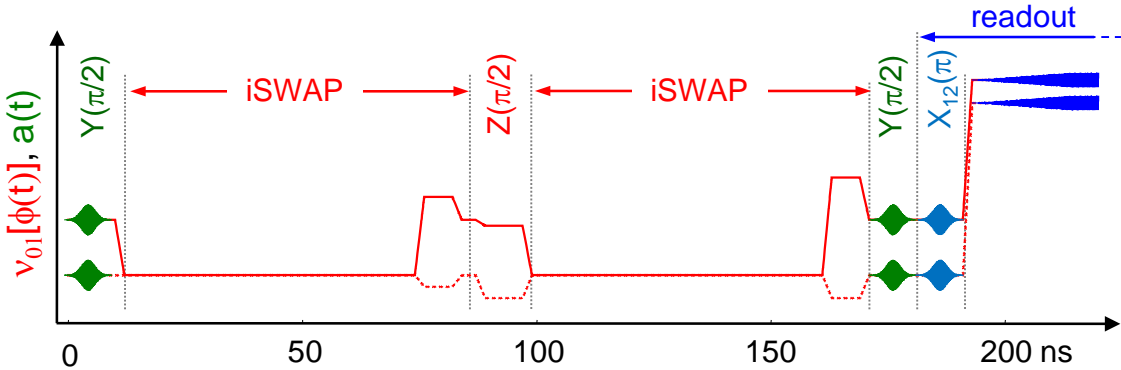


Figure 7.6: The pulse sequence used in realizing Grover's quantum search algorithm. First, a $Y_{\pi/2}$ pulse is applied to each qubit to produce the fully superposed state $1/2(|00\rangle + |01\rangle + |10\rangle + |11\rangle)$. Then, an $i\text{SWAP}$ gate is applied, followed by a $Z_{\pm\pi/2}$ gate on each qubit, which corresponds to the application of the oracle function. The resulting state is then analyzed using another $i\text{SWAP}$ gate and two $X_{\pi/2}$ gates to extract the state which has been marked by the oracle function. Optionally, a Y_{π}^{12} pulse is used on each qubit to increase the readout fidelity.

7.4 Results

Here we discuss the results obtained when running the Grover search algorithm with our two-qubit processor. In the first section we will analyze the quantum state of the qubit register during the algorithm by performing quantum state tomography. In the second section we will present and discuss the single-run results obtained in our experiment.

7.4.1 State Tomography of the Algorithm

Fig. 7.7 shows the results when running the Grover search algorithm for the four possible Oracle functions. Shown are quantum state tomographies after each step of the algorithm and the single-run results obtained when measuring the qubit register after the final step of the algorithm. In subfigures (a)-(d) The black outlined circles in the density matrices represent the ideal theoretical states, whereas the colored, solid circles represent the experimentally measured states. The trace fidelities of all states with the ideal ones are noted above each density matrix. As can be seen, the fidelity diminishes as a function of the runtime of the algorithm due to dephasing and relaxation of the qubit register. The experimental single-shot probabilities in subfigure (e) are shown along with the expected probabilities, which are calculated based on the readout matrix of our two-qubit system and the state tomographies after the final state of the algorithm.

7.4.2 Single Run Results

The experimental state tomographies discussed in the last section show that we are able to implement the Grover search algorithm with adequate fidelity using our two-qubit processor. However, the analysis of the two-qubit register by quantum state tomography at the end of the algorithm does not prove that we can achieve real quantum speed-up with our processor. For this, it is necessary to directly read out the state of the qubit register at the end of the algorithm *without* performing any kind of error correction afterwards. By looking at this “raw” outcome data and averaging it over many identical runs of the processor we can then quantify the success rate and the fidelity of the algorithm we implemented. The results of such measurements that we performed for the four possible Oracle functions is shown in fig. 7.8. Besides the single-run probabilities for all four Oracle functions, the diagram also shows for comparision the expected outcome probabilities that are calculated based on the quantum state tomographies discussed above and the readout matrix of the two-qubit system. As can be seen, the agreement between the measured and calculated probabilities is quite good. The dashed line in the diagrams corresponds to the success probability of a classical “query-and-guess” algorithm as described above, which is bound to 50 % and provides the benchmark against which we measure the quantum speed-up in this system. As can be seen, our implementation of the Grover search algorithm outperforms a classical search algorithm for all four Oracle functions, if only by a small margin.

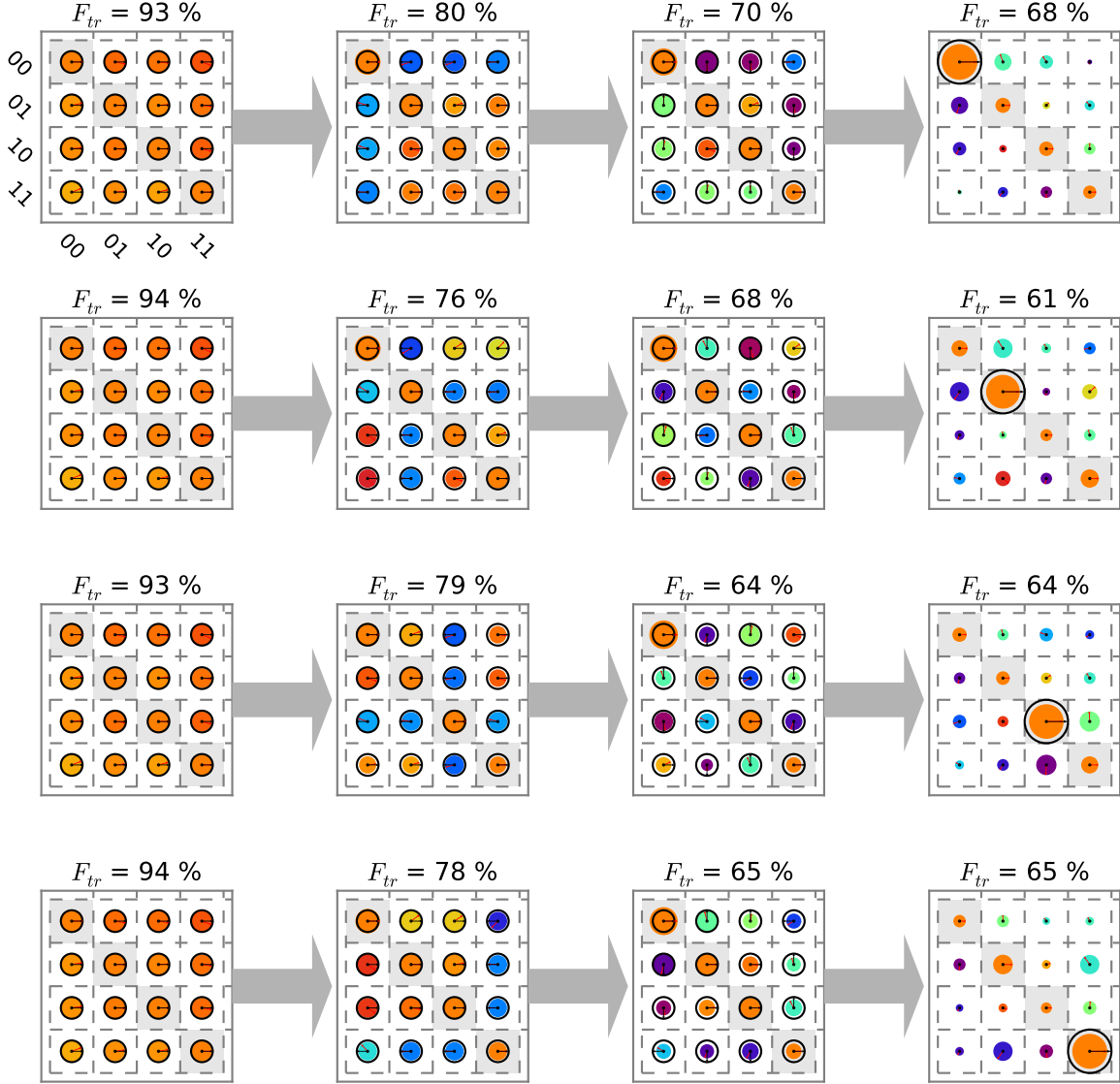


Figure 7.7: Quantum state tomographies at different steps of the Grover search algorithm. The density matrices show the experimentally measured states in color and the theoretical states in black. For each state, the trace fidelity $F_{tr}(\rho_A, \rho_B) = \text{Tr}\{\rho_A \cdot \rho_B\}$ is shown above the density matrix.

7.5 Algorithm Fidelity

We can define the average fidelity of the algorithm in a single run, which corresponds to the averaged success probabilities measured for all four Oracle functions and averaged over a large sample set. Table 7.1 shows these single-run probabilities along with the so-called *user fidelities*, which are given as

$$f_{ab} = p(|ab\rangle |ab\rangle) = \frac{p(ab|ab\rangle)}{\sum_{uv} p(uv|uv\rangle)} \quad (7.15)$$

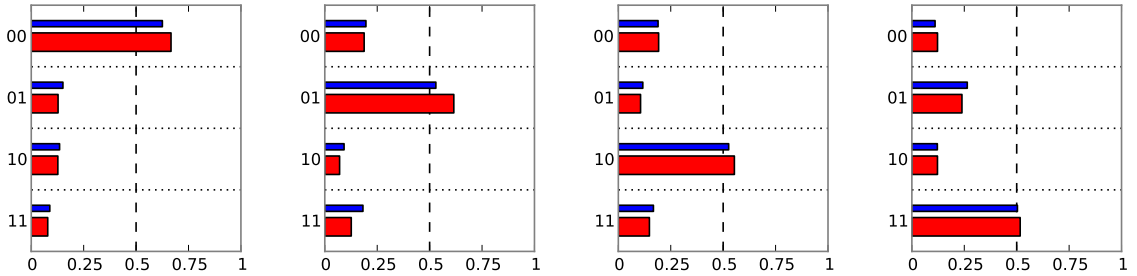


Figure 7.8: The single-run success probabilities of our implementation of the Grover search algorithm. Shown are the averaged probabilities for the four possible Oracle functions. The red bars correspond to measured values, the blue ones to expected probabilities calculated using the reconstructed density matrices after the final step of the algorithm and the measured two-qubit readout matrix. The dashed line indicates the average success probability of a classical query-and-guess algorithm for comparison.

and correspond to the probability of having obtained the correct answer given a certain outcome, averaged over all four possible Oracle functions. For all four, both the single-run and user fidelities are $> 50\%$, hence demonstrating quantum speed-up in comparison with a classical query-and-guess algorithm as discussed above.

$ab/ uv\rangle$	$ 00\rangle$	$ 01\rangle$	$ 10\rangle$	$ 11\rangle$	\sum	f_{ab}
00	0.666	0.192	0.188	0.122	1.168	57.0 %
01	0.127	0.554	0.071	0.122	0.874	63.4 %
10	0.128	0.106	0.615	0.239	1.088	56.5 %
11	0.079	0.148	0.126	0.517	0.870	59.4 %

Table 7.1: Conditional probabilities $p_{ab/|uv\rangle}$ and statistical fidelities f_{ab} for all possible outcomes ab , measured for our version of Grover's algorithm.

7.6 Error Analysis

There are three kind of errors arising in our implementation of the Grover search algorithm that we will analyze in the following section. These errors are:

1. Deterministic, unitary gate errors
2. Stochastic errors introduced due to qubit decoherence during the runtime of the algorithm
3. Readout errors due to qubit relaxation during the readout of the qubit state, insufficient coupling between the qubit and the readout or retrapping of the readout state during measurement

We will analyze the contributions of all these three error sources for the implementation of the algorithm below.

7.6.1 Gate Errors & Decoherence

Gate errors are unitary errors that arise due to misshaped or mistuned gate pulses. Usually the effect of these errors is combined with stochastic, non-unitary errors arising due to qubit decoherence during the runtime of the algorithm and therefore has to be analyzed together with the latter. Hence, in order to quantify these errors it is necessary to generate an error model of our algorithm that takes into account both unitary as well as non-unitary errors and whose parameters we obtain by fitting the model to our experimental results. Repeating this procedures for the experimental runs implementing the four different Oracle functions we obtain a full quantitative error model for all of them.

Modeling Decoherence

We could again model decoherence processes in our algorithm by formulating an effective master equation of the two-qubit system that includes relaxation and dephasing processes as we did when analyzing the universal quantum gate that we implemented. For our implementation of the Grover algorithm, however, we chose to rather use a set of discrete decoherence operators that model amplitude (i.e. T_1) and phase damping (i.e. T_ϕ) processes and which we can directly integrate in a more simple, operator-based model of the algorithm. We can then model the decoherence in our algorithm by applying these operators to the calculated quantum states after each individual step of the algorithm. Like this we can generate an error model incorporating the most relevant experimental decoherence processes without the need to numerically integrate an effective master equation, thereby greatly speeding up the process of fitting our experimental data to the formulated error model. In the following paragraphs we introduce the reader to the operators we use to model relaxation and dephasing processes in our error model.

To model qubit relaxation, we can use a pair of single-qubit operators describing amplitude-damping of the qubit state, which given as (Michael A. Nielsen and Isaac L. Chuang, 2000)

$$E_1^{T_1} = \begin{pmatrix} 1 & 0 \\ 0 & \sqrt{1 - \gamma_{T_1}} \end{pmatrix} \quad E_2^{T_1} = \begin{pmatrix} 0 & \sqrt{\gamma_{T_1}} \\ 0 & 0 \end{pmatrix} \quad (7.16)$$

On the other hand, phase-damping operators describing qubit dephasing can be written

analogously as

$$E_1^{T_{\phi 1}} = \begin{pmatrix} 1 & 0 \\ 0 & \sqrt{1 - \gamma_{\phi}} \end{pmatrix} \quad E_2^{T_{\phi 1}} = \begin{pmatrix} 0 & 0 \\ 0 & \sqrt{\gamma_{\phi}} \end{pmatrix} \quad (7.17)$$

Both operators are applied to a quantum state ρ according to

$$\rho \rightarrow E_1 \rho E_1^\dagger + E_2 \rho E_2^\dagger \quad (7.18)$$

and yield a trace-preserving, non-unitary evolution of the quantum state of ρ . The decoherence fraction γ that is used in the operators can be calculated from the corresponding relaxation and dephasing rates as $\gamma_{T_{1,2}}(t) = 1 - \exp(-t\Gamma_{1,2}^{T_1})$ and $\gamma_{\phi_{1,2}} = 1 - \exp(-t\Gamma_{1,2}^{T_{\phi}}/2)$, where t is the time during which the state is exposed to the given decoherence process.

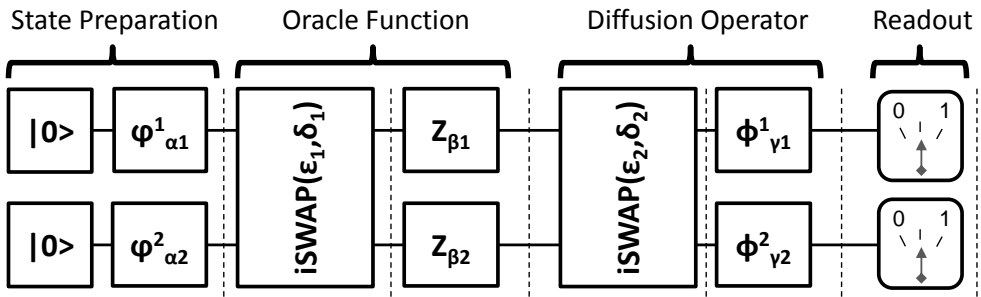


Figure 7.9: The error model we use to analyze the different gate and decoherence errors present when running the Grover search algorithm. The dotted lines indicate the points at which the quantum state has been measured by state tomography.

Using these two operators combined with a set of unitary operators describing the quantum operations performed during the algorithm we formulate a full error model that we use to model our experimental data, as shown in fig. 7.9. This model takes into account the following error sources:

- **Energy relaxation and phase decoherence:** Energy relaxation and dephasing of the qubit is modeled using the processes given in eqs. (7.16) and (7.17), applying these operators with an adapted γ after each unitary operation performed during the algorithm.
- **Single-qubit gate errors:** We model rotation angle and rotation phase errors of our single-qubit X_α and Y_α gates by replacing them with operators of the form $X_\alpha \rightarrow \phi_{\alpha'} = \cos \phi X_{\alpha'} + \sin \phi Y_{\alpha'}$ and $Y_\alpha \rightarrow \varphi_{\alpha'} = \sin \varphi X_{\alpha'} + \cos \varphi Y_{\alpha'}$. For Z -type single-qubit operators we model only rotation angle errors by replacing $Z_\alpha \rightarrow Z_{\alpha'}$.

- **Two-qubit gate errors:** We model both detuning and gate-length errors of our *iSWAP* 2-qubit gates.

For the two-qubit gates, we model the errors present in the *iSWAP* operation by using the model

$$i\text{SWAP}(t, \Delta) = \begin{pmatrix} 1 & 0 & 0 & 0 \\ 0 & \cos t g_e - i \frac{\Delta}{g_e} \sin t g_e & i \frac{g}{g_e} \sin t g_e & 0 \\ 0 & i \frac{g}{g_e} \sin t g_e & \cos t g_e + i \frac{\Delta}{g_e} \sin t g_e & 0 \\ 0 & 0 & 0 & 1 \end{pmatrix} \quad (7.19)$$

where $g_e = \sqrt{g^2 + \Delta^2}$ is the effective swap frequency at a qubit frequency detuning $f_{01}^1 - f_{01}^2 = 2\Delta$. Often it is practical to replace t and Δ with $\beta = t g_e$ and $\delta = \Delta/g$. Using this notation of the *iSWAP* gate and the definition of the single-qubit gates as discussed before, the full algorithm with gate errors can be written as (for right-multiplication)

$$\text{Grover} = \phi_{\gamma_1}^1 \otimes \phi_{\gamma_2}^2 \cdot i\text{SWAP}(\epsilon_2, \delta_2) \cdot Z_{\beta_1} \otimes Z_{\beta_2} \cdot i\text{SWAP}(\epsilon_1, \delta_1) \cdot \varphi_{\alpha_1}^1 \otimes \varphi_{\alpha_2}^2 \quad (7.20)$$

In addition, we add a dephasing and relaxation error after each step of the algorithm to model the decoherence during the runtime of the algorithm. Numerical optimization is then used to produce a fit of all the gate errors, which is shown in tab. 7.2. Here, the qubit relaxation and dephasing times were measured independently and are not part of the fit.

state	δ_1	δ_2	α_1	α_2	φ_1	φ_2	ϵ_1	β_1	β_2	ϵ_2	γ_1	γ_2	ϕ_1	ϕ_2
$ 00\rangle$	0.06	-0.06	-2.5	2.7	6.1	3.1	-7.3	-3.3	-4.1	7.5	29	9.3	0.66	-1.7
$ 01\rangle$	0.04	-0.3	-0.1	0.1	7.9	3.6	-11	-5.9	2.2	-6.9	28	-19	9	2
$ 10\rangle$	0.09	-0.2	-3.1	1.7	1	-2.5	-6.5	-15	-22	-7.5	-15	32	3.6	5.2
$ 11\rangle$	0.16	0.13	-6	3.9	2.2	0.9	-9.5	-20	-15	17	-12	-32	-7	-8.9

Table 7.2: Fitted error parameters for the measured density matrices, modeled according to the error model given in eq. (7.20). All angles are given in deg.

The resulting fitted error models obtained for our experimental data are shown in tab. 7.2. As can be seen, the phase and gate-time errors for the first gates are comparatively small and grow bigger during the following steps of the algorithm. Curiously, the phase errors are bigger for the states $|10\rangle$ and $|11\rangle$, as are the gate-length errors for the two *iSWAP* gates used in the algorithm. This fact might be explained by a drift of the operating point of our microwave setup during the time it took to take the data for the four possible Oracle operators, during which the parameters of individual qubit gates were not recalibrated.

Fig. 7.10 shows again the measured density matrices for our realization of the Grover search algorithm, this time overlaid with the numerically optimized error model according

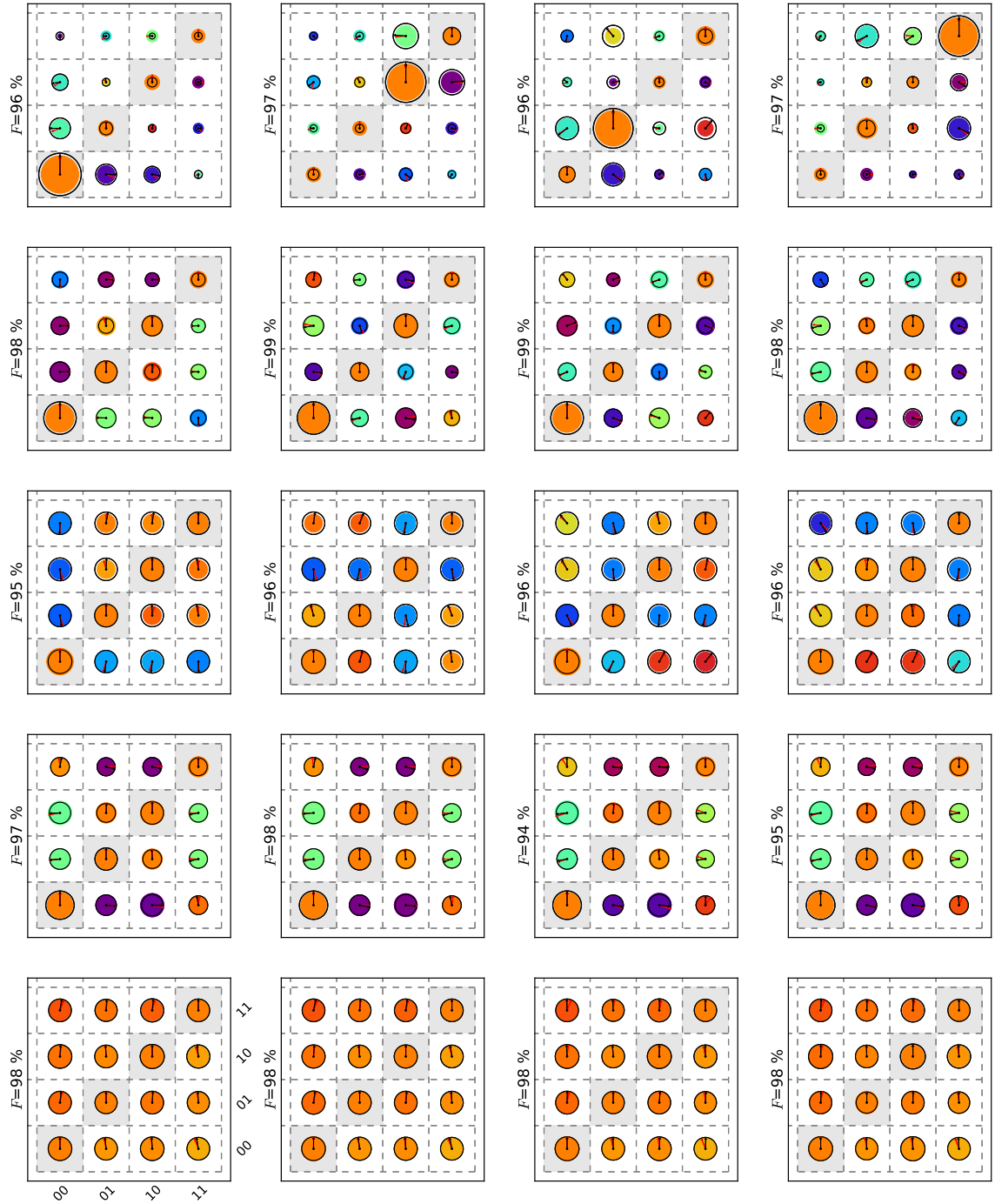


Figure 7.10: Comparison of the fitted error model as given by eq. (7.20) to our experimental data. Experimental data is shown in color, the fitted density matrices as black outlines. As before, we show the state fidelity according to eq. (??) between experimental and fitted states.

to eq. (7.20). As can be seen, our error model is able to capture most of the observed experimental errors and can reproduce to very good accuracy the observed density matrices. The state fidelities according to eq. ?? between the measured density matrices and those of the fitted error model are shown above each density matrix.

Fidelity of the Oracle and diffusion operators

It is interesting to analyze the individual experimental fidelities of the Oracle and diffusion operators that make up the Grover algorithm achieved in our experiment. For this, we compare the action of the ideal operators D' and R' with that of the experimentally implemented versions D'_e and R'_e , taking the measured quantum states before applying each of the operators as input. We take then as the fidelity of each operator the average state fidelity of the measured output states as compared to the calculated ones, i.e.

$$F(D'_e) = F(D'\rho_{in}D'^\dagger, D'_e\rho_{in}D'^\dagger) \quad (7.21)$$

$$F(R'_e) = F(R'\rho_{in}R'^\dagger, R'_e\rho_{in}R'^\dagger) \quad (7.22)$$

where we also make use of the state fidelity according to eq. ???. By this method, we obtain the following experimental fidelities for the two gate operations:

Operator / State	$ 00\rangle$	$ 01\rangle$	$ 10\rangle$	$ 11\rangle$	Average
D'	92.3	93.4	94.3	91.7	92.9
R'	94.5	93.6	88.5	87.7	91.1

Table 7.3: Measured fidelities of the quantum Oracle and diffusion operators used in the Grover search algorithm according to eqs. (7.21) and (7.22). All fidelities are given in percent.

As can be seen, on average we are able to implement both the diffusion operator and the quantum Oracle with a fidelity $> 90\%$.

7.6.2 Readout Errors

Another source of errors affecting the single-run fidelities of the algorithm arises due to the imperfection of our qubit readout. Here, mostly qubit relaxation during the readout process reduces the visibility of individual qubit states and introduces errors when reading out the qubit register in the final step of the algorithm. We can easily quantify those readout errors by using the readout matrix that was introduced in the last chapter. When running the Grover algorithm we use the $|1\rangle \rightarrow |2\rangle$ shelving method described in the last chapter to increase the readout contrast and thereby the algorithm fidelity. This technique reduces single-qubit readout errors but increases inter-qubit readout crosstalk. To

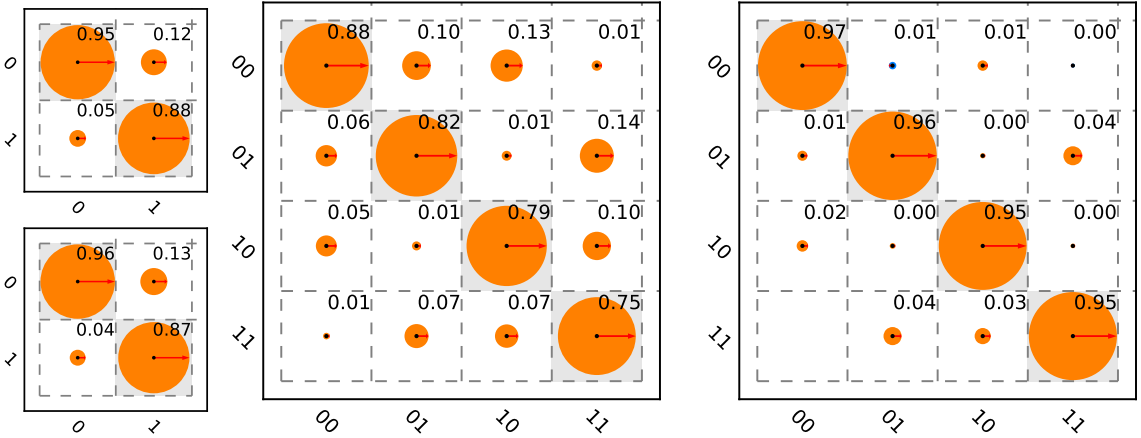


Figure 7.11: a.)The measured single-qubit readout matrices, showing the readout outcome probabilities as a function of the prepared state for both qubits. b.)The measured two-qubit readout matrix, showing again the detector outcome probabilities versus the prepared qubit states. c.) The crosstalk matrix, corresponding to the product of the inverse two-qubit readout matrix and the Kronecker product of the single-qubit readout matrices. Note that the $|1\rangle \rightarrow |2\rangle$ shelving method is used for reading out the qubit state, which increases readout fidelity but also inter-qubit readout crosstalk.

quantify all single-qubit and inter-qubit readout errors, we first model the readout matrix R of the two-qubit system as a product $R = R_v \cdot R_{ct}$, where R_v is the so-called *visibility matrix* and R_{ct} a matrix describing the readout crosstalk. The visibility matrix can be written as the Kronecker product $R_v = R_v^1 \otimes R_v^2$ of the two single-qubit readout matrices, which have the form

$$R_v^{1,2} = \begin{pmatrix} p_{00}^{1,2} & 1 - p_{11}^{1,2} \\ 1 - p_{00}^{1,2} & p_{11}^{1,2} \end{pmatrix} \quad (7.23)$$

Here, $p_{00}^{1,2}$ ($p_{11}^{1,2}$) corresponds to the probability to measure the value 0 (1) at the readout after having prepared the qubit in state $|0\rangle$ ($|1\rangle$). Usually, the full two-qubit readout matrix R and the single-qubit readout matrices $R_v^{1,2}$ are measured experimentally which allows us then to calculate the crosstalk matrix as $R_{ct} = R_v^{-1} \cdot R$. The three matrices measured in our experiment are shown in fig. 7.11. As can be seen, the single-qubit readout fidelities range between 87 - 96 % and the combined two-qubit readout fidelities between 75 - 85 %. Depending on the qubit state we also observe between 3-5 % inter-qubit readout crosstalk in our system.

Fig. 7.7e shows the single-run probabilities when running the Grover algorithm for the four different Oracle functions. In blue, the expected readout outcome probabilities, as calculated using the state tomography of the final states given in fig. 7.7d and the measured readout matrix of our system are shown along the measured readout outcome probabilities. The readout error model shows good quantitative agreement with the measured data, with deviations most probably due to parameter drifts occurred be-

tween the measurement of the quantum state tomography and the single-run experiment.

7.7 Conclusions

To summarize, we have shown that we can implement the Grover search algorithm with our quantum processor and achieve a single-run fidelity that is sufficient to demonstrate simple probabilistic quantum speed-up as compared to a classical, reversible search algorithm. The error model formulated in this chapter is able to account for most of the observed imperfections and can explain the data we observed. Unfortunately, the coherence times of our qubits does not permit the realization of more complex algorithm with this system, but nevertheless it provides a proof-of-principle of our approach to build a superconducting quantum computer with individual-qubit single shot readout.

In the following chapter, we will discuss the extension of this approach to a system of four qubits and explain different strategies for scaling up such system to an even larger number of qubits.

Chapter 8

Conclusions & Perspective

8.1 Future Directions in Superconducting QC

8.1.1 3D Circuit Quantum Electrodynamics

8.1.2 Hybrid Quantum Systems

8.1.3 Quantum Error Correction & Feedback

Appendix A

Modeling of Multi-Qubit Systems

A.1 Analytical Approach

A.1.1 Multi-Qubit Hamiltonian

A.1.2 Energies and Eigenstates

A.2 Master Equation Approach

$$\frac{d\rho}{dt} = -\frac{i}{\hbar}[H, \rho] + \sum_j [2L_j \rho L_j^\dagger - \{L_j^\dagger L_j, \rho\}] \quad (\text{A.1})$$

A.2.1 Direct Integration

A.2.2 Monte Carlo Simulation

A.2.3 Speeding Up Simulations

Appendix B

Data Acquisition & Management

B.1 Data Acquisition Infrastructure

B.2 Data Management Requirements

B.3 PyView

B.3.1 Overview

B.3.2 Instrument Management

B.3.3 Data Acquisition

B.3.4 Data Management

B.3.5 Data Analysis

Appendix C

Design & Fabrication

C.1 Mask Design

C.2 Optical Lithography

C.3 Electron Beam Lithography

Bibliography

- Baur, M., Philipp, S., Bianchetti, R., Fink, J. M., Göppl, M., Steffen, L., Leek, P. J., Blais, A., and Wallraff, A. (2009). Measurement of Autler-Townes and mollow transitions in a strongly driven superconducting qubit. *Physical Review Letters*, 102(24):243602.
- Blais, A., Huang, R., Wallraff, A., Girvin, S. M., and Schoelkopf, R. J. (2004). Cavity quantum electrodynamics for superconducting electrical circuits: An architecture for quantum computation. *Physical Review A*, 69(6):062320.
- Chiorescu, I., Nakamura, Y., Harmans, C. J. P. M., and Mooij, J. E. (2003). Coherent quantum dynamics of a superconducting flux qubit. *Science*, 299(5614):1869–1871.
- Clarke, J., Cleland, A. N., Devoret, M. H., Esteve, D., and Martinis, J. M. (1988). Quantum mechanics of a macroscopic variable: The phase difference of a josephson junction. *Science*, 239(4843):992–997.
- Clauser, J. F., Horne, M. A., Shimony, A., and Holt, R. A. (1969). Proposed experiment to test local Hidden-Variable theories. *Physical Review Letters*, 23(15):880–884.
- Collin, E., Ithier, G., Aassime, A., Joyez, P., Vion, D., and Esteve, D. (2004). NMR-like control of a quantum bit superconducting circuit. *Physical Review Letters*, 93(15):157005.
- Cottet, A. (2002). *Implementation of a quantum bit in a superconducting circuit*. PhD thesis, Université Paris VI, Paris.
- Deutsch, D. (1985). Quantum theory, the Church-Turing principle and the universal quantum computer. *Proceedings of the Royal Society of London. A. Mathematical and Physical Sciences*, 400(1818):97–117.
- Devoret, M. (1995). Quantum fluctuations in electrical circuits. In *Les Houches Session on Quantum Fluctuations*, volume LXIII, pages 351–386.
- Devoret, M. H., Martinis, J. M., and Clarke, J. (1985). Measurements of macroscopic quantum tunneling out of the Zero-Voltage state of a Current-Biased josephson junction. *Physical Review Letters*, 55(18):1908–1911.

- DiCarlo, L., Chow, J. M., Gambetta, J. M., Bishop, L. S., Johnson, B. R., Schuster, D. I., Majer, J., Blais, A., Frunzio, L., Girvin, S. M., and Schoelkopf, R. J. (2009). Demonstration of two-qubit algorithms with a superconducting quantum processor. *Nature*, 460(7252):240–244.
- DiCarlo, L., Reed, M. D., Sun, L., Johnson, B. R., Chow, J. M., Gambetta, J. M., Frunzio, L., Girvin, S. M., Devoret, M. H., and Schoelkopf, R. J. (2010). Preparation and measurement of three-qubit entanglement in a superconducting circuit. *Nature*, 467(7315):574–578.
- DiVincenzo, D. P. (2000). The physical implementation of quantum computation. *Fortschritte der Physik*, 48(9-11):771–783.
- Fedorov, A., Steffen, L., Baur, M., and Wallraff, A. (2011). Implementation of a toffoli gate with superconducting circuits. *arXiv:1108.3966*.
- Feynman, R. (1982). Simulating physics with computers. *International Journal of Theoretical Physics*, 21(6):467–488.
- Göppl, M., Fragner, A., Baur, M., Bianchetti, R., Filipp, S., Fink, J. M., Leek, P. J., Puebla, G., Steffen, L., and Wallraff, A. (2008). Coplanar waveguide resonators for circuit quantum electrodynamics. *Journal of Applied Physics*, 104(11):113904–113904–8.
- Grover, L. K. (1997). Quantum mechanics helps in searching for a needle in a haystack. *Physical Review Letters*, 79(2):325–328.
- Grover, L. K. (2001). From schrödinger’s equation to the quantum search algorithm. *American Journal of Physics*, 69(7):769–777.
- Haroche, S. and Raimond, J. (2006). *Exploring the Quantum: Atoms, Cavities and Photons*. Oxford University Press.
- Johnson, B. R., Reed, M. D., Houck, A. A., Schuster, D. I., Bishop, L. S., Ginossar, E., Gambetta, J. M., DiCarlo, L., Frunzio, L., Girvin, S. M., and Schoelkopf, R. J. (2010). Quantum non-demolition detection of single microwave photons in a circuit. *Nature Physics*, 6(9):663–667.
- Josephson, B. (1962). Possible new effects in superconductive tunnelling. *Physics Letters*, 1(7):251–253.
- Koch, J., Yu, T. M., Gambetta, J., Houck, A. A., Schuster, D. I., Majer, J., Blais, A., Devoret, M. H., Girvin, S. M., and Schoelkopf, R. J. (2007). Charge-insensitive qubit design derived from the cooper pair box. *Physical Review A*, 76(4):042319.

- Lanyon, B. P., Hempel, C., Nigg, D., Müller, M., Gerritsma, R., Zähringer, F., Schindler, P., Barreiro, J. T., Rambach, M., Kirchmair, G., Hennrich, M., Zoller, P., Blatt, R., and Roos, C. F. (2011). Universal digital quantum simulation with trapped ions. *Science*, 334(6052):57–61.
- Lloyd, S. (1996). Universal quantum simulators. *Science*, 273(5278):1073–1078.
- Mallet, F., Ong, F. R., Palacios-Laloy, A., Nguyen, F., Bertet, P., Vion, D., and Esteve, D. (2009). Single-shot qubit readout in circuit quantum electrodynamics. *Nat Phys*, 5(11):791–795.
- Martinis, J. M., Devoret, M. H., and Clarke, J. (1985). Energy-Level quantization in the Zero-Voltage state of a Current-Biased josephson junction. *Physical Review Letters*, 55(15):1543–1546.
- Martinis, J. M., Nam, S., Aumentado, J., and Urbina, C. (2002). Rabi oscillations in a large Josephson-Junction qubit. *Physical Review Letters*, 89(11):117901.
- Michael A. Nielsen and Isaac L. Chuang (2000). *Quantum Computation and Quantum Information*. Cambridge University Press.
- Mooij, J. E., Orlando, T. P., Levitov, L., Tian, L., van der Wal, C. H., and Lloyd, S. (1999). Josephson Persistent-Current qubit. *Science*, 285(5430):1036 –1039.
- Motzoi, F., Gambetta, J. M., Rebentrost, P., and Wilhelm, F. K. (2009). Simple pulses for elimination of leakage in weakly nonlinear qubits. *Physical Review Letters*, 103(11):110501.
- Nakamura, Y., Pashkin, Y. A., and Tsai, J. S. (1999). Coherent control of macroscopic quantum states in a single-Cooper-pair box. *Nature*, 398(6730):786–788.
- Paik, H., Schuster, D. I., Bishop, L. S., Kirchmair, G., Catelani, G., Sears, A. P., Johnson, B. R., Reagor, M. J., Frunzio, L., Glazman, L. I., Girvin, S. M., Devoret, M. H., and Schoelkopf, R. J. (2011). Observation of high coherence in josephson junction qubits measured in a Three-Dimensional circuit QED architecture. *Physical Review Letters*, 107(24):240501.
- Palacios-Laloy, A. (2010). *Superconducting qubit in a resonator: Test of the Leggett-Garg inequality and single-shot readout*. PhD thesis, Université Paris VI, Paris.
- Pozar, D. M. (2011). *Microwave Engineering*. Wiley, 4 edition.
- Reed, M. D., DiCarlo, L., Nigg, S. E., Sun, L., Frunzio, L., Girvin, S. M., and Schoelkopf, R. J. (2011). Realization of Three-Qubit quantum error correction with superconducting circuits. *arXiv:1109.4948*.

- Schuster, D. I., Houck, A. A., Schreier, J. A., Wallraff, A., Gambetta, J. M., Blais, A., Frunzio, L., Majer, J., Johnson, B., Devoret, M. H., Girvin, S. M., and Schoelkopf, R. J. (2007). Resolving photon number states in a superconducting circuit. *Nature*, 445(7127):515–518.
- Siddiqi, I., Vijay, R., Metcalfe, M., Boaknin, E., Frunzio, L., Schoelkopf, R. J., and Devoret, M. H. (2006). Dispersive measurements of superconducting qubit coherence with a fast latching readout. *Physical Review B*, 73(5):054510.
- Siddiqi, I., Vijay, R., Pierre, F., Wilson, C. M., Metcalfe, M., Rigetti, C., Frunzio, L., and Devoret, M. H. (2004). RF-Driven josephson bifurcation amplifier for quantum measurement. *Physical Review Letters*, 93(20):207002.
- Vijay, R., Devoret, M. H., and Siddiqi, I. (2009). Invited review article: The josephson bifurcation amplifier. *Review of Scientific Instruments*, 80(11):111101–111101–17.
- Vijay, R., Slichter, D. H., and Siddiqi, I. (2011). Observation of quantum jumps in a superconducting artificial atom. *Physical Review Letters*, 106(11):110502.
- Vion, D., Aassime, A., Cottet, A., Joyez, P., Pothier, H., Urbina, C., Esteve, D., and Devoret, M. H. (2002). Manipulating the quantum state of an electrical circuit. *Science*, 296(5569):886 –889.
- Wallraff, A., Schuster, D. I., Blais, A., Frunzio, L., Huang, R.-S., Majer, J., Kumar, S., Girvin, S. M., and Schoelkopf, R. J. (2004). Strong coupling of a single photon to a superconducting qubit using circuit quantum electrodynamics. *Nature*, 431(7005):162–167.
- Yurke, B. and Denker, J. S. (1984). Quantum network theory. *Physical Review A*, 29(3):1419–1437.